THE HONG KONG POLYTECHNIC UNIVERSITY
香港理工大學
Pao Yue-kong Library
包玉剛圖書館

Copyright Undertaking

This thesis is protected by copyright, with all rights reserved.

By reading and using the thesis, the reader understands and agrees to the following terms:

1. The reader will abide by the rules and legal ordinances governing copyright regarding the use of the thesis.
2. The reader will use the thesis for the purpose of research or private study only and not for distribution or further reproduction or any other purpose.
3. The reader agrees to indemnify and hold the University harmless from and against any loss, damage, cost, liability or expenses arising from copyright infringement or unauthorized usage.

IMPORTANT

If you have reasons to believe that any materials in this thesis are deemed not suitable to be distributed in this form, or a copyright owner having difficulty with the material being included in our database, please contact lbsys@polyu.edu.hk providing details. The Library will look into your claim and consider taking remedial action upon receipt of the written requests.

Pao Yue-kong Library, The Hong Kong Polytechnic University, Hung Hom, Kowloon, Hong Kong

http://www.lib.polyu.edu.hk

AN INVESTIGATION ON THE METALLURGICAL PROCESS AND DEFORMATION MECHANISM OF A NOVEL RESOURCE-SAVING DUPLEX STAINLESS STEEL (DSS)

WAN JIANQUAN

Ph.D

The Hong Kong Polytechnic University

2018

The Hong Kong Polytechnic University

Department of Mechanical Engineering

An Investigation On The Metallurgical Process And Deformation Mechanism Of A Novel Resource-saving Duplex Stainless Steel (DSS)

WAN Jianquan

A Thesis Submitted in Partial Fulfillment of the Requirements for the
Degree of Doctor of Philosophy

May 2017

Certificate of Originality

I hereby declare that this thesis is my own work and that, to the best of my knowledge and belief, it reproduces no material previously published or written, nor material that has been accepted for the award of any other degree or diploma, except where due acknowledgment has been made in the text.

Abstract

Though most duplex stainless steels are generally water quenched from high temperature, at which the equilibrium phase constitution is close to the desired magnitude. The non-equilibrium phase transformation in duplex stainless steel is less explored. The temperature-time-transformation diagram of duplex stainless steel was established, which shows that duplex stainless steel of equilibrated primary phase content can be obtained through different thermomechanical process. Specifically, we studied the effect of annealing temperature, time, cooling method and plastic deformation on the phase transformation of 15Cr-2Ni-2Al-11Mn duplex stainless steel, in which the consumption of Cr and Ni is reduced by substituting Al and Mn, respectively.

The room-temperature duplex structure of duplex stainless steel is always metastable, which suggests that non-equilibrium phase transformation can be further exploited for producing duplex stainless steel having the same chemical compositions and phase constitution but different microstructures. It shows that the duplex stainless steel with about 50% austenite phase can be prepared using different non-equilibrium thermal process, of which the yield strength and elongation vary in the ranges of 307~499 MPa and 20~33%, respectively. The sample, which exhibits the best combination of yield strength (371 MPa) and elongation (33%), is attributed to the bimodal distribution of austenite grain size.

The non-equilibrium phase transformation in producing DSS should be more

thoroughly explored on the partition coefficient of alloying elements so that to improve the corrosion resistance of duplex stainless steel. The microstructure exhibits impact on the overall corrosion resistance of duplex stainless steel. The annealing temperature and cooling rate affect the partition coefficient of alloying elements associated with the change of the ferrite volume fraction. When the volume fraction of ferrite increases, the partition coefficient becomes more uniform and close to 1. The partition coefficients of Cr and Al increase while those of Ni and Mn decrease with the annealing time, and finally become steady after the sample reaching composition homogenization period. The contrast of corrosion resistance between ferrite and austenite phases varies on the change of the partition coefficient of alloying elements, which is markedly affected by annealing temperature and time. For 1000 °C annealing 15min and 30 min respectively, the first-etched phase for former is ferrite but for latter is austenite. For 1150 °C annealing 15min, the first-etched phase is austenite.

The growing kinetics of sigma phase and its precipitation hardening effect on duplex stainless steel were also investigated. Upon aging at 750~900 ºC, sigma phase precipitates in the DSS, and the size and amount of sigma phase increase continuously with aging time. TTT diagram of sigma phase precipitation is established, and the kinetics of sigma phase formation reaches peak at 850 ºC. Mo increases the formation rate and the mass amount of sigma phase. Aging at 850 °C for 180 minutes leads to about 1.5% volume fraction of sigma phase and a peak strength of duplex stainless steel.

In order to gain more understanding of phase evolution in duplex stainless steel, the mean-field theoretical model for austenite reformation is established, which is used to

rationalize the exponent of the Avrami equation for fitting the kinetics of phase transformation. The phase field model for the influence of diffusion properties on phase transformation of duplex stainless steel was further established.

Key words：Duplex stainless steel; Resource-saving; Microstructure; TTT diagram; Mechanical Property; Bimodal size; Corrosion resistance； Plastic deformation; Partition coefficient; Corrosion resistance; Precipitation hardening; Avrami analysis; Phase field Model

Research output arising from the thesis

Publications of journal papers

[1] **Jianquan Wan,** Haihui Ruan, Jianbiao Wang, Sanqiang Shi. Exploiting the non-equilibrium phase transformation in a 15Cr-2Ni-2Al-11Mn resource-saving duplex stainless steel. Materials and Design 114 (2017) 433–440

[2] **Jianquan Wan**, Haihui Ruan, Sanqiang Shi. Excellent combination of strength and ductility in 15Cr-2Ni duplex stainless steel based on ultrafine-grained austenite phase. Materials Science & Engineering A, 690 (2017) 96–103

[3] **Jianquan Wan**, Haihui Ruan, Sanqiang Shi. The partition coefficient of alloying elements and its influence on the corrosion resistance of 15Cr-2Ni duplex stainless steel. Corrosion science, 2017, Under review.

[4] **Jianquan Wan**, Haihui Ruan, Sanqiang Shi. The kinetics diagram of sigma phase and its precipitation hardening effect on 15Cr-2Ni duplex stainless steel. Materials Science & Engineering A, 2017, Under review.

Conference

[1] Low-chromium low-Nickel resource-saving duplex Stainless Steel-Achievement and challenge. Nano-mechanical interfaces 2015, The HongKong University of Science and Technology, HongKong.

[2] Non-equlibrium phase transformation in a 15Cr-2Ni resource-saving duplex stainless steel. ICMMP 2016, The HongKong Polytechnic University, HongKong.

Acknowledgements

I would like to address the most sincere gratitude to my supervisors Dr. Haihui Ruan and Prof. Sanqiang Shi, for their consistent support, encouragement and patience on my research work. Their academic guidance, strictness and knowledge will be the most precious fortune for my whole life. The thesis would not be completed without their invaluable supervision and encouragement.

Special thanks to all the people who have been actively helped me complete this thesis. Sincere thanks to all the technical staffs in Department of Mechanical Engineering and Materials Research Centre at The Hong Kong Polytechnic University, City University of Hong Kong and The Chinese University of Hong Kong for their technical support. Genuine thanks to all my colleagues at the Hong Kong Polytechnic University for helping me in every particular work in and out of the thesis.

Last but not least, I would like to express my thanks to my family for their continuous support for my Ph.D. study. Their encouragements and understanding give me power to complete all the studies and research work at the Hong Kong Polytechnic University.

Table of contents

List of figures

List of tables

Chapter 1 Introduction

1.1 Definition of stainless steel

Stainless steel refers to steel which exhibits high chemical stability in air, water, acid and other corrosive media and high oxidation resistance at high temperature. The corrosion resistance mainly depends on the alloying elements contained in stainless steel. The alloying elements of stainless steel include Cr, Ni, Al, Mn, Mo, Ti, Nb, Cu, N, etc., of which many combinations are available to meet the requirements of various applications. The corresponding microstructure can be predicted by Schaeffler diagram (Fig.1.1) using chromium and nickel equivalent as follows:

The chromium equivalent is represented by the abscissa:

$$Cr_{eq} = \text{wt.\%Cr} + \text{wt.\%Mo} + 0.5\text{wt.\%(Si + Ti)} + 3\text{wt.\%A1} + 5\text{wt.\%V} \tag{1.1}$$

These elements are ferrite (δ)-forming elements.

The nickel equivalent is represented by the ordinate:

$$Ni_{eq} = \text{wt.\%Ni} + 30\text{wt.\%(C + N)} + 0.5\text{wt.\%Mn} + 0.33\text{wt.\%Cu} \tag{1.2}$$

These elements are austenite (γ)-forming elements. The corrosion resistance of stainless steel decreases with carbon content, therefore, most of stainless steels have a low carbon content, with a maximum value of lower than 1.2 wt.% and some even lower than 0.03 wt.%. Also, steel exhibits corrosion resistance only when the content of Cr reaches at least 10.5 wt.%. Stainless steel exhibits high strength, weldability, corrosion resistance, easy machining and a low ratio of price-life, etc. Stainless steel has been widely used in chemical industry, environmental protection, construction, automotive, aerospace, household appliances and medical industry, etc.

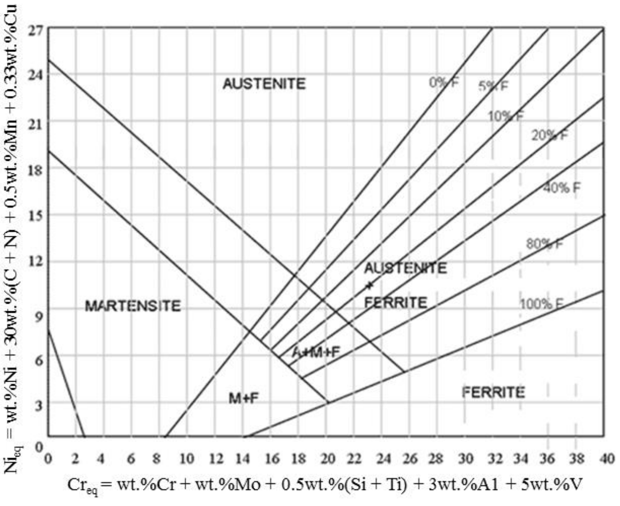

Fig.1.1 Schaeffler diagram

1.2 Classification of stainless steel

According to the microstructure of stainless steel used in the environment, stainless steel can be classified into the following five categories:

(1) Martensitic stainless steel

Martensite is a metastable phase transformed by γ phase via a non-diffusion phase transition. It exhibits ferromagnetic property, and its strength and hardness depend mainly on the super saturation content of C. With the increase of C, the boundary of γ phase area gradually extends in the direction of δ phase, which hinders the transformation of γ to martensite phase. Martensitic stainless steel exhibits high strength, hardness and wear resistance but relatively poor corrosion resistance. Therefore, martensitic stainless steel is applied in the components which require high performance of mechanical property and common corrosion resistance, such as springs, turbine blades, and hydraulic valves, etc. Martensitic stainless steel is used after quenching and tempering treatment which can improve its strength and ductility, and annealing softening is necessary followed by treatment of forging and stamping. Typical martensitic stainless steels include 1Cr13~4Cr13, 1Cr17Ni2, 2Cr13Ni2, etc.

(2) Ferritic stainless steel

The δ phase refers to the solid solution of body-centered cubic lattice structure formed by Fe and other elements. For common steel, it refers to the interstitial solid solution microstructure formed by C and other elements dissolved in δ-Fe. Then for ferritic stainless steel, it refers to the interstitial solid solution formed by 12%~30 wt.% amount of Cr dissolved in δ-Fe, including other δ-forming elements such as Al, Mo, etc. and an extremely low content of C. There is no transformation of δ-to-γ phase during the process of heating and cooling， and therefore ferritic stainless steel can't be strengthened by conventional heat treatment. Due to high content of Cr, ferritic stainless steel shows a strong resistance to corrosion and oxidation, and exhibits a good plasticity. However, it also shows undesirable brittleness such as high temperature brittleness, σ phase precipitation brittleness, and 475 °C brittleness, etc. It is mainly used to produce the components which require high corrosion resistance and relatively low strength, such as the nitric acid and nitrogen fertilizer equipment, etc. Typical ferritic stainless steels include Crl7, Cr25, and Cr28, etc. Advanced steels, which include low carbon and nitrogen, ultra low carbon and nitrogen, and high purity and super ferritic stainless steel, have largely overcome certain deficiencies exhibited by traditional ferritic stainless steel.

(3) Austenitic stainless steel

Austenitic stainless steel is the solid solution microstructure that Cr, Ni and small amounts of Mo, Ti, N, etc. dissolved in γ-Fe. It exhibits good comprehensive property and corrosion resistance against a variety of media. Large amounts of Ni and Cr are contained in austenitic stainless steel to maintain its austenitic state at room temperature. The main characteristics of austenitic stainless steel include non-magnetic austenitic organization at room temperature, low ratio of yield strength to tensile strength, good plasticity, good welding performance and easy hot forming, etc. It can't be strengthened by conventional heat treatment, but rather by cold working. It can be used to produce acid-resistant system such as corrosion resistant containers, pipelines, and nitric acid resistant equipment, etc. The typical brands of austenitic stainless steels include 1Cr18Ni9(Ti), 0Cr18Ni9Cu3, 0Cr17Ni12Mo2, and 0Cr25Ni20, etc.

(4) Austenitic-ferritic duplex stainless steel

Austenitic-ferritic duplex stainless steel has a microstructure of δ and γ phases, with approximately 50 vol.% of each. It exhibits the property of both austenitic and ferritic stainless steels. The details will be introduced in Sections 1.3.

(5) Precipitation hardening stainless steel

Carbide is precipitated by means of heat treatment so as to increase the strength of steel, and it is called precipitation hardening stainless steel. The matrix is γ or martensite phase, and it can be strengthened by heat treatment and precipitation hardening. Typical precipitation hardening stainless steels include 0Cr17Ni7A1(17-7PH) and 0Cr17Ni4Cu4Nb(17-4PH), etc.

In addition to the above categories, stainless steel can also be divided into the following four categories according to the alloying elements contained:

(1) Cr series stainless steel

Under general applications, the corrosion resistance of stainless steel increases with the content of Cr. A compact passive film forms on the surface of the steel when the content of Cr exceeds 12 wt.%. It performs normally in harsh environment, with an additional advantage of low cost, so this series of steel has been widely used. It is in the equivalent of AISI 400 stainless steel.

(2) Cr-Ni series stainless steel

Simply relying on the alloying element of Cr can’t meet the requirement of corrosion resistance in extremely harsh environment such as the acidic. The stability of the steel can be significantly improved when Cr is combined with Ni, such as the AISI 300 series.

(3) Cr-Ni-Mn-N series stainless steel

Due to the high cost of Ni, it can be replaced in certain conditions by Mn and N which perform similarly to Ni but are available at a lower price. This series of steel has been developing rapidly, such as AISI 200.

(4) Cr-Ni Precipitation hardening stainless steel

If a hardening secondary phase is formed in the matrix by precipitation, the mechanical property of stainless steel increases significantly. It is in the equivalent of AISI 600.

1.3 Definition of duplex stainless steel

Duplex stainless steel (DSS) is a dual-phase structure with δ and γ phases each half, generally minimum individual phase content of at least 30%, as shown in Fig.1.2. The δ phase is a body-centered cubic crystal structure, while γ phase is a face-centered cubic crystal structure as shown in Fig.1.3. In the condition of low content of C, DSS usually contains 18%~28% of Cr, 3%~10% of Ni and some other alloying elements such as Mo, Cu, Si, Nb, Ti, N, etc. DSS exhibits the advantage of both ferritic stainless steel and austenitic stainless steel. The existence of γ phase reduces the brittleness of high chromium contained ferritic stainless steel, prevents the grain growth tendency, and improves the toughness and weldability. The existence of δ phase improves the strength of austenitic stainless steel at room temperature, especially the yield strength and thermal conductivity, reduces the coefficient of expansion and welding hot cracking tendency, and improves the stress corrosion cracking resistance and pitting corrosion resistance. A typical steel 00Cr22Ni5Mo3N, exhibits the advantage of both austenitic and ferritic stainless steels. Compared to ferritic stainless steel, it shows higher plasticity and toughness, no brittleness at room temperature, better intergranular corrosion resistance and welding performance; Compared to austenitic stainless steel, it shows a higher yield strength and a stronger resistance of intergranular and stress corrosion. Fig.1.4 shows that DSS exhibits an attractive combination of mechanical property and corrosion resistance, e.g., twice yield strength, higher or similar corrosion resistance of austenitic stainless steel counterpart. DSS has been widely used in stringent environment such as nuclear power station, oil, and petrochemical service shown in Fig.1.5 [1-5].

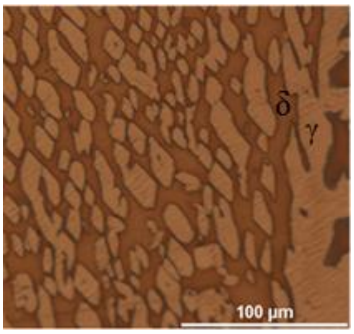

Fig.1.2 δ and γ phases in DSS

Fig.1.3 The cubic crystal structures of δ and γ phases

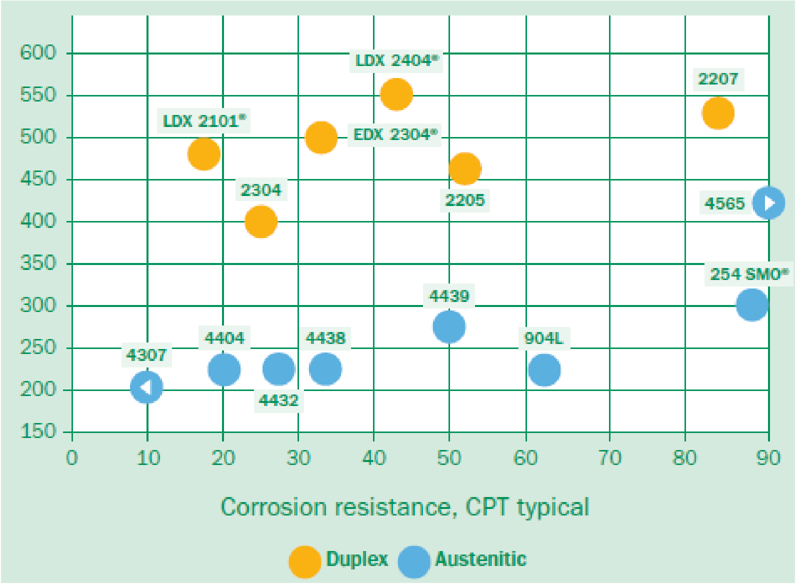

Fig.1.4 Comparison on the property between DSS and austenitic stainless steel counterpart

Fig.1.5 Tubes in nuclear power plant, oil and petrochemical industry and Chemical tanker

1.4 The propose of resource-saving DSS

DSS is formed, on the basis of 18-8 austenitic stainless steel, in terms of increasing Cr content or adding other δ phase forming elements so as to make steel a dual phase microstructure of γ and δ phases. The development of stainless steel has caused a great pressure for the resource of Ni, so the application of DSS is developed quickly. DSS replaces austenitic stainless steel in some ways, according to the points of production, processing and manufacturing, and application. With superior comprehensive performance of mechanical and corrosion resistance, DSS wins the favor of users. DSS has become an excellent corrosion resistant engineering material with low weight and investment. Common DSS contains 18~28% Cr and 4~7% Ni, so DSS exhibits a higher price than that of austenitic stainless steel counterpart and accounts for only a few share among the world consumption of stainless steel. To increase the marketing share of DSS, the less Ni and higher N contents have led to the lean DSS (LDX series), in which a portion of Ni was replaced by Mn. The most prominent trend for reducing cost is to replace Cr and Ni with other equivalent elements as shown in Fig.1.6. In recent years, Sweden's development on low Mn and low Ni DSS is relatively mature, and it has a clear goal to replace 304 and even the conventional DSS 2304. China also pays a high attention to the development of resource saving low Chromium and low Nickel DSS.

Nickel resource is very limited in China (Fig.1.7), so resource-saving DSS is proposed and investigated.

Fe–Al–Mn alloys exhibit good corrosion resistance and mechanical property. Al can stabilize the δ phase and improve the anti-corrosion behavior by forming a protective Al_2O_3 layer on the surface, while Mn can stabilize γ phase and enhance mechanical property at high temperature [6, 7]. However, the corrosion resistance of Fe–Al–Mn alloy is inferior to that of conventional stainless steel [8]. A new type 15Cr-2Ni DSS has been developed in the author's master period [9] and exhibits good mechanical property and corrosion resistance. The mechanism of the phase transformation, mechanical performance and the heat treatment control of 15Cr-2Ni DSS should be further investigated. Mathematical model of the phase transformation was also established on aiming to predict the phase evolution of DSS during annealing.

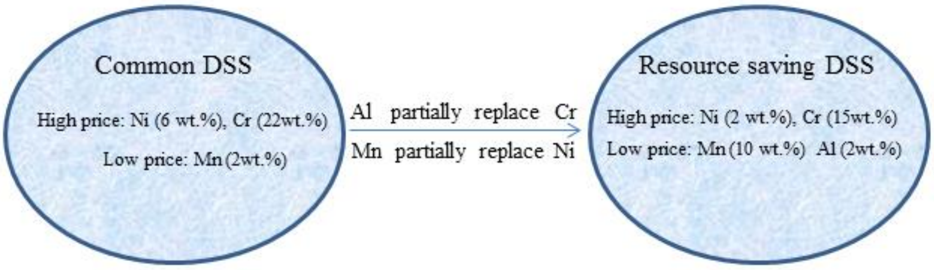

Fig. 1.6 The schematic diagram of resource saving DSS modified from common DSS

Fig.1.7 Nickel resource distribution in earth

1.5 The scope of the investigation

This work is based on the recently developed 15Cr-2Ni DSS [9], in which Al and Mn were alloyed, in terms of Cr-equivalent (Cr_{eq}) and Ni-equivalent (Ni_{eq}) elements, which can lead to a balanced content of both primary phases based on the Schaeffler-type diagram [10]. The 15Cr-2Ni series DSS introduced in [9] exhibits compelling properties that warrant more detailed investigation. In the conventional development of DSS, WRC1992 or Schaeffler diagram is widely used. However, Schaeffler diagram or WRC1992 is only obtained by air cooling, and thus can not provide adequate support. Meanwhile, the effect of thermal processing on the kinetics of phase transformation is not clear. Therefore, providing a theoretical model for alloy development is our focus. However, these diagrams merely represent the particular thermal history of welding, in which the arc-melted alloy was quenched in air and in contact with other metal parts under the cooling rate in the range of 10-10^3 °C/s. The actual thermal history of DSS production is different from welding, in which the cast ingot must be heated to a solution-treatment temperature to adjust the phase constitution and water-quenched for freezing the high-temperature microstructure. For such a process, the phase diagram is more useful, which describes the equilibrium phase constitutions at different temperatures and with different chemical compositions [11]. However, owing to the complicated chemical composition of resource-saving DSS, the phase diagram calculated using the state-of-the-art thermodynamics database may only be used qualitatively.

For a specific chemical composition, the volume fraction of δ phase can be managed by heat treatment. We perform the conventional heat treatment with 30 minutes annealing time at the beginning. Then we further perform the heat treatment with different annealing time (1, 3, 5, 7, 10, 15, 20, 40, 70 min……). Heat treatment is a thermal diffusion process running towards to an equilibrium state. As shown in Fig. 4.14, a high δ phase content contained in the preheated sample is beneficial to produce a standard DSS with 50% δ phase. The transformation process during annealing at a temperature higher than 1050 °C is too fast, and it is therefore not ideal to predict and produce a DSS product using a high annealing temperature. Controlling the content of δ phase is one of the main goals in optimizing the thermal process, and metallography image analysis software is used to measure it. Many variables affect the phase transformation in DSS alloys. Therefore, the development of resource-saving DSS must be done under the constraints of some variables. Conventionally, these constraints are generally specified for the heat treatment process, including solution-treatment temperature, the high-temperature holding time, the cooling method and chemical compositions. However, the major problems are that the knowledge collected over decades of research is still fragmented and that the cause, namely the chemical composition, and the effect, namely the microstructure and phase constitution, cannot be rationalized with a theoretical model. These difficulties motivate us to seek another route of developing resource-saving DSS: to fix the chemical composition and vary the heat treatment process. We will then establish the detailed temperature-time transformation (TTT) diagram of δ or γ phase and demonstrates that a particular of phase constitution can be achieved using different heat treatment processes. The material to be investigated in this dissertation research is the new series 15Cr-2Ni DSS, which was first developed by the author in his previous research [9].

After we obtain the standard DSS samples with approximately 50% δ phase produced by heat treatment with different annealing temperature, time, and cooling method, we can test the mechanical property of each sample. Therefore, we can develop an understanding on the effect of grain size, morphology on the mechanical property. We will show that several routes of heat treatment with different annealing temperature and cooling rate can be chosen to get a standard DSS with approximately 50% δ phase. However, they lead to different morphologies of phases and different grain size, which significantly influence the mechanical property. This result indicates the wide variety of possible heat-treatment processes to obtain DSS alloys with identical chemical and phase compositions.

The non-equilibrium phase transformation in producing DSS significantly involves the segregation of alloying elements. The partition coefficient of alloying elements could be explored so that the mechanism of corrosion resistance of DSS could be known and improved.

The growing kinetics of σ phase and its precipitation hardening effect on DSS alloy were investigated, and then the quantitative relation between σ phase and the mechanical property of DSS is sought. It proposes a solution to predict and well use the precipitation hardening effect to develop DSS alloy with proper strength and elongation.

Finally, a process model for γ phase reformation in DSS is established.

Chapter 2 Literature review

2.1 The development of stainless steel and duplex stainless steel

In 1797, people found that stainless steel is different from ordinary steel. The period from that time until 1878 can be seen as an early exploration stage of stainless steel. It was noted that Cr can improve the corrosion resistance of steel products. The significant progress in stainless steel research was made between 1895 and 1910, as signified by the publication of many valuable research papers. H. Brearley (U.K.) developed a stainless steel which is comparable to the current AISI420. Dantsizen, *et al.* developed a stainless steel which is comparable to the current SUS430. E. Maurer and B. Strauss (Krupp, Germany) developed a 18-8 stainless steel prototype, and carried out industrial production. Then, the furnace top open-type electric arc furnace was developed in 1922, followed by oxidation reduction smelting stainless steel. Because the arc furnace has the characteristic of less oxidation loss, which is especially suitable for the production of high alloy steel, so the melting of stainless steel was gradually came to be dominated by the electric arc furnace. In 1931, the ore oxidative decarburization method entered a practical stage, and the United States rustless steel took the lead in producing stainless steel. The preparation technique is called the rustless method, which uses high-carbon ferrochrome and chrome ore for the production of raw materials to replace the expensive low-carbon ferrochrome. In the 1940s, the oxygen blowing smelting method of producing stainless steel became popular. In 1954, the United States Union Carbide Corporation Niagara metal laboratory discovered the argon oxygen decarburization principle. The Witten special steel mill (Germany) developed the world's first vacuum oxygen decarbonization furnace-VOD in 1965. The first industrial AOD (argon-oxygen decarburization) refining converter was put into operation in the United States in 1968. After the single-step production process was gradually withdrawn from the stage of history, arc furnace single-refining stainless steel accounted for only 0.5% of the total output of stainless steel by 1991. At present, the AOD method is still the main method of smelting stainless steel. Most of the stainless steel plants in the world use electric arc furnace (EAF) + AOD two-step smelting stainless steel, and its output has exceeded 10 million tons, accounting for 68.7% of the world's total stainless steel output [12]. After years of development, AOD has undergone a number of technical improvements. Nippon Steel increases the top gun blowing oxygen, thereby improving the blowing process. AOD was also derived new methods, such as the converter vacuum blowing oxygen decarburization method (VODC).

At present, stainless steel manufacturers in foreign countries such as Kawasaki Chiba (four plants), the new iron Hachiman plant and the Brazilian ACESITA plant use three-step smelting (electric furnace➔converter➔vacuum degassing furnace). In China, TISCO and Baosteel built and produced similar production lines. The advantage of this technology includes flexible raw materials, low cost and high efficiency. It is also highly suitable for multi-species stainless steel production especially for ultra-low carbon and high nitrogen stainless steel smelting.

Apart from the improving technology in the production of stainless steel, continuous efforts have been extended to investigate the effect of the main alloying elements on designing and improving stainless steel, as discussed below [6, 7, 13]:

1. Cr

Cr is the most significant δ phase forming element and brings about the corrosion resistance. It increases the solubility of N which explains why the super DSS can contain higher N content than that of low Cr DSS. Cr also brings oxidation resistance to stainless steel.

2. Al

Al can stabilize the δ phase and improve the anti-corrosion behavior by forming a protective Al_2O_3 layer on the surface of stainless steel. Al improves the high temperature oxidation resistance and welding property of stainless steel.

3. Ni

In contrast to the δ phase stabilizing effect of Cr, Ni is a strong γ phase forming element. Ni improves both the stability and formability of γ phase. The γ phase volume fraction increases with Ni content, while Cr and Mo are enriched in the remaining δ phase, leading to the enhanced possibility that δ transformation to intermetallic phases during 750~950 °C.

4. Mn

Mn has been referred as an γ phase stabilizer. It can increase the temperature range and formation rate of detrimental sigma phase. It increases the abrasion, wear resistance and tensile property of DSS, without loss of ductility. Additionally, it increases the solid solubility of N and cold work hardening effect. It is sensitive to intergranular corrosion, and the inter-granular corrosion cannot be removed by the addition of Ti and Nb.

5. Mo

Mo is beneficial to the pitting and crevice corrosion resistance of DSS in chloride solutions, and it was found to suppress active sites via the formation of an oxyhydroxide or molybdate ion. Additionally, it has a similar effect on δ phase stability as Cr, and it can increase the strength of DSS.

6.Cu

Cu can increase the cold work hardening of stainless steel. It improves the machinability in low oxygen and sulphur materials. Generally, its addition to DSS is limited to 2%, because higher level reduces hot ductility and can lead to precipitation hardening.

In order to utilize the potential of stainless steel and find the best match with the elements such as Cr, Ni, etc., the researchers are constantly deepening the exploration. The future research can be conducted into the following aspects [14, 15]:

(1) Pure purification, fine grain and ultrafine crystal research. In the metallurgical industry, the research on the pure purification of materials has been advanced and the concept of clean steel and zero inclusion steel is proposed. As the material grain was refined, the micro-characteristics of materials and structure are improved. It will yield special material property that is not shown in the normal state.

(2) Nickel-free stainless steel. With the increase in stainless steel production, nickel demand is continually expanding. Reducing the proportion of nickel in stainless steel or replacing nickel with other elements without sacrificing its original performance is a viable and valued option.

(3) High-strength stainless steel. With the development of some large parts and lightweight components, the requirements of the material strength are increasing. A combination of alloying, especially micro-alloying and high purity, highly homogeneous refining, casting technology and ultrafine grain control technology is used to develop the new material with good toughness and corrosion resistance.

(4) Stainless steel with high corrosion resistance. It is imperative to develop stainless steel materials with good corrosion resistance as required for various special industries such as seawater purification plants, chemical plants and serious corrosion of coastal sodium chloride, etc.

(5) Stainless steel with high heat and oxidation resistance. With the deep exploration of the universe, it is necessary to develop materials with excellent resistance to high temperature and oxidation.

The discovery of a duplex microstructure was first described by Bain and Griffiths [16] in 1927 but it was not until the 1930s that DSS became commercially available. China began to study DSS in the mid-1970s, and the main research has been focused on nitrogen steel, which has been developed into five steel grades. Austenitic (300 series) stainless steel ratio has decreased from 90% in the 1980s to approximately 50%

nowadays, and the ferrite (400 series) stainless steel ratio has increased to 30% or more. The stainless steel industry, especially TISCO, Baosteel and other enterprises, are accelerating the research into new super ferritic stainless steel. In addition, we should provide not only middle and thick plates, but also hot and cold thin sheets to promote the development of DSS. The current focus is to promote conventional DSS 2101 and 2003, etc.

The production, processing and application of DSS in foreign countries have been matured after several decades of development. Owing to the difficulties in the refining of DSS during the steelmaking stage and the welding and thermoforming in the manufacturing process, the consumption of DSS is only 1% of the total amount of stainless steel to date. China is poor in nickel resources, and the development of stainless steel has imposed great pressure on the nickel resources. Therefore, the research and application of DSS is very wide and rapid. The most widely used DSS is S32205. In recent years, DSS has gradually opened up the potential market for industrial and civil use, including the construction industry and manufacturing containers, etc. The typical DSS can be classified into four types as follows:

1. Low alloy. The representative brand is UNS S32304 (23Cr-4Ni-0.1N), PRE 24~25, and it can replace AISI 304 OR 316 in terms of stress corrosion resistance.
2. Middle alloy. The representative brand is UNS S31803 (22Cr-5Ni-3Mo-0.15N), PRE 32~33. The corrosion resistance is between those of AISI 316L and 7%Mo+N austenite stainless steel.

3. High alloy, usually with 25% Cr, and Mo, N. The representative brand is UNS S32550(25Cr-6Ni-3Mo-2Cu-0.2N), PRE 38~39. Its corrosion resistance is higher than that of 22Cr DSS.

4. Super DSS with high content of Mo and N. The representative brand is UNS S32750 (25Cr-7Ni-3.7Mo-0.3N), PRE>40. It can be used in a hard environment with excellent corrosion resistance and mechanical property. It is comparable to super austenite stainless steel.

2.2 Phase transformation in DSS

DSS is constituted by δ and γ phases, and the important performance of DSS relies on the volume proportion of the two phases. The non-equilibrium phase transformation, which is ubiquitous in producing DSS, should be more thoroughly explored such that the microstructure can be better controlled. The influence of heat treatment parameters, such as annealing temperature, time, cooling rate as well as plastic deformation on the phase transformation was investigated much but scattered, so it is comprehensively investigated in this work.

In the open literature, many investigations have exhibited the important effect of processing parameters of post-cast thermomechanical treatment. For example, Sohn *et al.* [19] investigated the effect of annealing temperature on microstructural and mechanical property of Fe-0.35C-3.5Mn-5.8Al alloy. Li *et al.* [20] investigated the effect of annealing time on the content, distribution and shape of δ phase in DSS. Chen *et al.* [21] demonstrated that cooling rate is critical for the adjustment of the volume fraction of primary phases. They analyzed the phase content in the welding-induced heat affected zone of DSS 2304 and found that γ phase content increased gradually from 27.8 % to 35.7% as the cooling rate decreased from 100 to 10 °C/s. Several researchers [22-24] reported that plastic deformation exhibits a significant influence on the phase transformation, mechanical, corrosion and formability property of DSS. Although the non-equilibrium evolution of primary phase in DSS has been studied in welding process [25, 26], the TTT diagram of primary phase transformation in DSS is rarely found in the open literature. This can probably be ascribed to the fact that the solution treatment for adjusting phase content in DSS is quite unified. Most of the solution treatment of DSS is based on the notion of quenching equilibrium phase content of a high temperature. Therefore, TTT diagram of non-equilibrium phase transformation is seemingly not crucial. In this work, through establishing the TTT diagram of primary phase transformation in DSS, we would like to show that DSS of equilibrated phase content may be achieved under different heat treatment since the non-equilibrium phase transformation can be utilized.

Developing DSS based on the quinary Fe-Cr-Ni-Al-Mn system is intricate since the property and phase constitution are affected by not only the chemical composition but also the thermal and mechanical treatments. The phase prediction diagram based on the products of welding can only provide very limited guidance since the thermal process for producing DSS is significantly different from welding. The usual processing for DSS, after the alloy is cast, involves forging for remove internal voids, isothermal holding for adjusting the phase composition and final quenching to retain the high-temperature microstructure. In this process, the equilibrium phase diagram may help to choose an appropriate holding temperature [1]. But detailed effects of annealing temperature and time, cooling rate and plastic deformation cannot be found in a phase diagram, which therefore limits the choices of processing parameters. For this purpose, the complete picture of non-equilibrium phase transformation was also established.

A numerical model was developed to calculate the kinetic of δ-to-γ phase transformation in DSS. The modeling of the phase transformation behavior in DSS has been the topic of many researchers due to the increased emphasis on the microstructure control. Hertzman *et al.* calculate the kinetics of δ-to-γ phase transformation during cooling based on Cahn's theory of grain boundary nucleated reactions [27]. Hemmer *et al.* investigate the kinetics of the γ-to-δ phase transformation during heating and build an analytical model based on nitrogen diffusion [26]. These analytical models provide important understand on the kinetic of phase transformation, but the accuracy of the calculation is based on several simplifying assumptions. Then, in W. Zhang’s research [28], they remove these simplifying assumptions while address more realistic situations, and provide excellent insights into the mechanism and kinetics of γ-to-δ transformation during welding of DSS. They assume that the transformation rate of γ-to-δ phase during heating is controlled by nitrogen diffusion in both two phases, local equilibrium of nitrogen is maintained at δ/γ interface and the partition of substitutional elements is little. They address realistic situations that non-uniform starting microstructure exists grain boundaries (hard impingement) and overlapping diffusion fields (soft impingement) while conventional diffusion models assume a uniform starting microstructure.

The conventional theoretical investigations of the variation of primary phases were only conducted for DSS alloys with a substantial amount of nitrogen. In them, the diffusion of nitrogen was considered to be the main reason for the phase transformation. However, this is not the case for the resource-saving DSS investigated in this work. In order to understand the phase evolution in our material, the following assumptions are made: (i) the transformation between γ and δ phases is governed by the diffusion of substances and (ii) the diffusion is due to the exchange of position between vacancy and solute atom. The interphase boundary then serves as a vacancy reservoir to assist the flow of substances.

2.3 Mechanical property

Mechanical property of DSS was investigated based on the understanding of phase transformation. DSS is usually recommended to present the optimum δ/γ phase ratio close to 1:1 without secondary phase precipitation to exhibit best mechanic and corrosion resistance properties [29-32]. It is an interesting question on how to optimize the mechanical property of DSS in production. Many attempts are try to reveal the strengthening mechanisms and establish constitutive stress–strain relations of γ and δ phases in DSS. The conventional notion about DSS is still that the δ-phase is harder than γ-phase [33, 34], which is the cause of higher yield strength of DSS than that of ASS. For example, Guo et al. [35] utilized micro-pillar compression technique coupled with EBSD to quantify the deformation behavior of δ and γ-phases in a cast DSS and got the result that δ-phases exhibits higher strength than that of γ-phase. However, some investigations have shown that γ-phase could be harder[36, 37] than δ-

phase in DSS. Foct and Akdut [38] made a microprobe analysis on the fracture surface of DSS with SEM and EBSP, and found that nitrogen content can largely increase the yield stress of the austenitic phase, even change it from being the softer phase to become the harder phase compared to ferrite phase. It is possible to make the γ-phase harder than the δ-phase when nitrogen content in DSS exceeds 0.12 wt.%, which has been proved by many reports [39, 40]. The research on the mechanical properties of these individual phases is essential to the understanding and development of DSS. Studies have pointed out that the deformation behavior and the damage mechanisms for a particular dual phase stainless steel are related to their chemical compositions, inclusions, and morphology of the microstructure [9, 41, 42]. The deformation characteristics of the constituent phases and their effects on the overall deformation based on the sub-microstructure evolution during plastic deformation and chemical composition of the constituent phases is worth to be investigated. Fréchard et al. [43] combined AFM and EBSD to study the fracture surface, established a complete description on the plastic deformation of δ and γ-phases of DSS, and provided deep insights on slip systems of constitute phases in the tensile test of DSS.

It is well known that rolling leads to “pancake” grains, which is an effective approach to obtain small grains in the process involving phase transformation, since nucleation of new phase preferably starts at grain boundaries and the pancake-shaped grains limited the space of grain growth. The process combining plastic deformation and annealing is a widely adopted approach to produce ultrafine grains [44]. DSS heat-treated at low temperature can not only reduce growth rate of grains but also keep more deformed and dislocated microstructures, leading to finer γ-phase grains [45]. Therefore, the recently-developed 15Cr-2Ni DSS with approximately 50% δ/γ-phase was produced by cold rolling followed by different heat treatments to demonstrate disparate combinations of strength and ductility in this work. The bimodal grain size of austenite was obtained, which provides DSS excellent mechanical performance.

Developing DSS with high strength and high ductility attracts wide attention in recent years, and the possible solutions mainly include making use of transformation induced plasticity (TRIP) effect, precipitation hardening and grain refinement. When the TRIP effect occurs, the plate retained austenite induced martensite nucleation and formation on the condition of plastic deformation generates local hardening. Deformation does not concentrate in the local, and phase transformation evenly spread throughout the material to improve the strength and ductility, leading to a DSS with excellent mechanical property, good formability and energy absorption capacity. DSS with TRIP effect can get an ultra high strength up to 1GPa and 60% ductility by an optimal design on the concentration of alloying elements aimed to reduce austenite stability [46]. With the increase of isothermal aging time at 750 °C, the ultimate strength of Cr19 DSS is increased from 1100 to 1400 MPa due to the dislocation hindering effect by precipitate of $Cr_{23}C_6$ at δ-phase boundary [32]. Effect of thermal aging at 475 °C was reported [47] to increase significantly the hardness of δ-phase but reduce the toughness rapidly of lean duplex stainless steel 2101. Surface mechanical attrition treatment (SMAT) is a useful way of grain refinement. In principle, the treatments improve surface structures and properties of metals by impact of shots and or milling balls. The grain size is refined to the nanometer scale, the surface and subsurface possess compressive residual stress, and the surface morphology and roughness are modified. The recent studies shows that SMAT can increase effectively the tensile and bending strength, the thermal stability and the fatigue life of AISI 316L [48, 49].

2.4 Corrosion resistance

The non-equilibrium phase transformation, which is ubiquitous in producing DSS, should be more thoroughly explored so that the segregation behavior of alloying elements can be better controlled and used. Conventional research focused more on how to improve the mechanical property, but less on corrosion resistance. The influence of heat treatment on the corrosion resistance of DSS is rarely found. The addition of Al and Mn further complicates the empirical relation between corrosion resistance and the composition of chromium and nickel. The important question we may ask is: what is the role of the partition coefficient of alloying elements in affecting the corrosion resistance of DSS.

Bernhardsson [50] used thermodynamic data to calculate that the pitting corrosion resistance of the alloy can be optimized by selecting a proper diffusion annealing temperature in order to obtain an equilibrium concentration of alloy elements corresponding to equal pitting resistance in ferrite and austenite. Solomon and Devine [51] discussed how the proportion of δ and γ-phases influences the pitting corrosion resistance of DSS. Therefore, the modification of the microstructures within DSS would be very effective in improving their overall corrosion resistance. Solution treatment is important for DSS. It can promote dissolution of carbide and other phases after rolling process, and change the volume fraction of *δ* and *γ*-phase. Also, it varies the concentrations of alloying elements in the two phases and therefore changes the corrosion resistance of DSS [1, 33, 52, 53]. Solution treatment can promote dissolution of carbide and other precipitation phases after rolling process, change the volume fraction of *δ*-phase and *γ*-phase, and vary the content of alloying elements in the two phases by altering the solution temperature and time. Therefore, solution treatment is critical for using the corrosion resistance of DSS [1, 33, 52, 53]. For a particular DSS, heat treatment parameters, such as annealing temperature, time and cooling rate, may lead to significantly different corrosion resistance, which thus needs a detailed study. A more fundamental understanding of the alloying elements on the effect of the partition coefficient between *δ*-ferrite and γ-austenite and resultant corrosion resistance in the DSS were sought.

2.5 Precipitation of sigma and other secondary phases

Various brittleness tendencies of *δ* phase are retained as shown in Fig.2.1, especially in high Cr (such as 25% Cr) and Mo contained DSS which the matrix is *δ* phase. The formation of secondary phases usually occurs in the temperature range 700-1000 °C and decomposition of *δ* phase occurs in the range 350-500 °C (475 °C embrittlement). Therefore, exposures at these temperatures should be avoided. However, if secondary phases could be ideally controlled in size, morphology and distribution, they would change from harmful to beneficial, and DSS would take a big step forward. It remains a big challenge to the development of DSS.

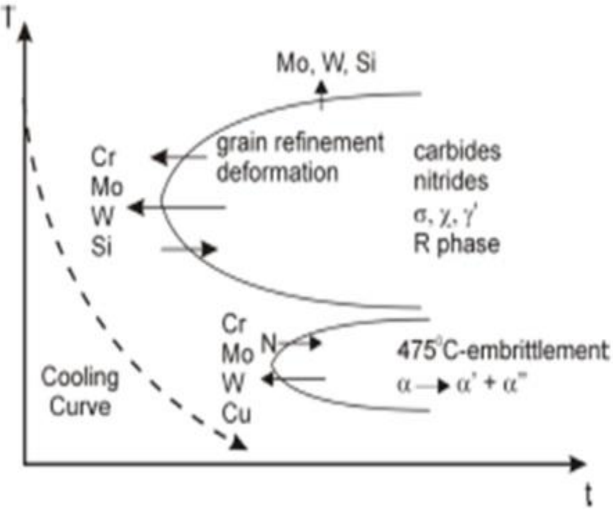

Fig.2.1 Occurrence of various precipitates

The σ phase is a non-magnetic intermetallic phase consisting mainly of iron and chromium that forms in ferritic and austenitic stainless steels during annealing at 550-950 ºC. Aging is a heat treatment technique used to induce precipitation hardening and increase the yield strength of malleable materials. Most structural alloys of aluminium, magnesium, nickel, titanium, and some stainless steels can be aged to precipitate secondary phases for achieving a higher strength. It relies on the variation of solid solubility with temperature to produce fine particles of an impurity phase, which impede the movement of dislocations or other defects in a crystal lattice. Precipitation by aging can produce particles of different size, resulting in radically different mechanical properties. Precipitation hardening occurs at high temperature or room temperature, and it usually increases the hardness and strength while decreases plasticity and toughness of alloys. DSS can be age hardened by the precipitation of one or more secondary phases. Several precipitation reactions can occur during the aging temperature of 700-1000 °C, such as σ, χ, γ_2, $M_{23}C_7$, Cr_2N, etc. [54], of which σ phase most significantly deteriorates the ductility, toughness and corrosion resistance. Therefore, the application of DSS is usually limited to temperatures not exceeding approximately 500 °C. Ghosh *et al.* [55] investigated the high temperature aging behavior of DSS and found that the short-time annealing have only modest effects on the hardness and strength, that long term aging at 900 °C increases strength and decreases elongation, and that long term aging at 1000°C results in the dissolution of secondary phases and an optimum combination of strength and elongation. The extent of influence of σ phase precipitation on the mechanical properties of stainless steels depends on several factors, including the amount of σ phase precipitated and the size, morphology and distribution of σ phase in the matrix. The fine and homogeneous dispersion of σ phase can play a role of precipitation strengthening in stainless steels [56, 57]. Growing proper size and amount of σ phase in ferrite phase through aging is mostly used to develop precipitation hardening in DSS.

The relation between precipitation evolution and mechanical property is still not clear for DSS. Understanding the temperature-and-time dependent phase transformation is very important for DSS. For example, Kim *et al.* [58] studied the precipitation of σ-phase, and developed its TTT diagram in cast DSSs (CD3MN and CD3MWCuN). Weatherly et al. [59] studied σ phase precipitation in 2205 DSS after cooling at different rate from different annealing temperature using MAC X-ray diffractometry and found that annealing temperature higher than 1080 °C and cooling rate faster than 0.25 °C/s could effectively suppress the formation of σ phase. Plastic deformation increases the amount of σ phase precipitation in 2205 DSS [60]. This study is intended to complement the information about the growing kinetics of σ phase, and propose a solution for the good use of the precipitation hardening effect to develop DSS alloys with diverse strength and ductility.

2.6 Machinability

Good machinability such as turning, drilling, cutting, and threading is essential to the manufacturing of steel products. DSS is difficult to machine due to its high strength, low volume fraction of non-metallic inclusions and low carbon content. Non-metallic inclusions can improve the machinability of DSS. Report [61] improves the machinability of DSS 22Cr-5Ni-3Mo by increasing the Sulphur content while reducing the corrosion resistance and toughness. Therefore, there is a compromise among the machinability and corrosion resistance/toughness of DSS. It has been reported that the machinability is reduced by high content of alloying elements [1, 61].

2.7 Welding performance

The welding performance of DSS has been achieved considerable progress over the past decade by adjusting the chemical composition and the welding parameters [62]. Early DSS alloys were susceptible to the formation of carbides due to the carbon content as high as 0.1%. Thus, it was virtually impossible to avoid carbide precipitation in the heat-affected zone when welding such type steels, leading to low toughness and low corrosion resistance. Also, the δ phase content in these steels is usually high and it often results in entirely ferritic welds. However, modern DSS alloys are poor in carbon but rich in nitrogen. Carbide formation is virtually eliminated, and reformation of γ phase is strong due to the high diffusivity of N. However, high N in the δ phase may cause precipitation of chromium nitrides. Last, welding generates a heat affected zone, which can be regarded as a chill casting, so it is easy to get residual stress.

2.8 Residual stress.

Stress that exists in materials in their unloaded state is termed residual stress. The formation of residual stresses occurs primarily during the production process and is associated with differential cooling and non-uniform plastic deformation. Residual stress in DSS has been frequently studied by diffraction-based techniques [63]. The X-ray diffraction technique is widely used for the determination of surface stress in both near-surface region and the interior of the sample. The residual stress in stainless steel can not be assumed to be of the same magnitude or distribution as that in carbon steel, due to the different physical and thermal properties that stainless steel exhibits. For DSS, residual stress can be caused by the highly anisotropic microstructure, different coefficients of thermal expansion and the mismatch of the stress fields of γ and δ phases, cold rolling [64] and the localized welding heat input and uneven cooling in fabricated sections[65]. The general influence of residual stress on DSS includes premature yielding, a loss of stiffness and a reduction in load-carrying capacity. To understand the mechanical property of DSS, it is necessary to understand the behavior of crystallites of individual phases. The value of initial stresses can be significant [36], so it can influence the mechanical property of the individual phase. The in-situ deformation of DSS during tensile and compressive loadings [63] was studied using a time-of-flight (TOF) neutron diffraction technique and self-consistent modeling, and the strains in a large number of crystallites, providing a good estimation of macroscopic as well as intergranular stress. Andera *et al.* [65] examined residual stresses in cold-rolled stainless steel using X-ray diffraction, and Cruise *et al.* [66] measured the residual stresses in hot-rolled and press-braked stainless steel. The different thermal expansion between the γ and δ phases, it leads to plastic deformation upon pure thermal cycling. The magnitude of thermally induced stresses surpasses the elasticity limit either of one or both phases [67]. L. Gardner et al. [68] determined the specific value of residual stresses for different sections using the electrical strain gauges, a mechanical gauge and a curvature dial.

2.9 Fatigue damage

The degradation of the material resulting from cyclic stress/strain such as repeated application of load called fatigue damage. Fatigue performance of DSS is investigated due to its increased use in industrial applications especially in corrosive environments. Fatigue damage can be influenced by many factors such as chemical composition, microstructural morphology and the local plastic activity of each phase [69, 70]. DSS exhibits a superior resistance to stress-corrosion cracking due to the high Cr and Mo contents. Fatigue damage generally initiates at plastic strain concentration sites. The initiated crack then grows under repeated applied load including low-cycle, high-cycle and very high-cycle (higher than 10^7 cycles) fatigue. Very high-cycle fatigue properties of engineering materials are increasingly of interest to ensure longer service life and are vital for excellent industrial productivity. Cyclic plasticity is partitioned mainly to the softer γ phase leading to the occurrence of elastic residual stresses in the δ phase grains in earlier research. The crack initiation stage dominates the total fatigue life and more than 90% of the total fatigue life of a sample is spent during the crack initiation stage [71]. An important feature of the fracture surface of very high-cycle fatigue is the fine granular area (FGA) at the initiation point. The mechanism of the formation of FGA is not fully understood yet, although different models [72-74] have been proposed on explain it. Fatigue crack initiation occurs at the surface of DSS samples due to inhomogeneous plastic deformation of δ and γ phases. Fatigue crack initiation occurs transgranularly or intergranularly in the δ grain with the reason of slip transmission from the γ grain or separation of the δ/γ phase boundary [24–27], respectively. Research [75] aims to evaluate the features of FGA around crack initiating surface defects in DSS, and the FGA feature around the crack initiation points were observed and found to be composed of nano-sized grains. However, the mechanism of the creation of FGA is still unclear.

DSS is more resistant to fatigue than that of austenitic stainless steel counterpart, especially for stress corrosion controlled fatigue. It is well demonstrated by reports [76, 77]. DSS was found to be superior to the single phase alloys in terms of fatigue performance due to the fine grain size [78].

2.10 Summary and remarks

DSS is one of the best choices in many applications due to a good combination of corrosion resistance and mechanical strength if it is properly heat treated. Though there is some difficulties in welding in early time, the welding problem has been overcome in modern DSS so the welds show similar corrosion resistance and mechanical property as those of the base material. The duplex microstructure, which is the key to the unique properties, relies on the correct heat treatment. Therefore, the relationship between phase evolution in microstructure and overall performance is essential for research. Much attention should be paid to deleterious phenomena such as the precipitation of σ phase, which can cause the degrade of DSS on performance such as corrosion resistance, machinability and fatigue, etc. Though σ phase can be controlled in proper size, morphology and distribution to exhibit both good strength and toughness for DSS, the heat treatment is still difficult to be designed and accurately in practice. Both the primary and σ phases transformation can be modeled using mathmatic equation, and it provides an important prediction effect that can not be obtained by experiment method.

Chapter 3 Alloy and experimental design

3.1 Alloy design

The consideration on composition design of the alloy includes: a) low Chromium low Nickel in purpose of saving resource, b) the as-cast result contains both ferrite and austenite phases. Based on previous research [79]:

$$M_s = 539-423C-30.4\,Mn-17.7\,Ni-12.1\,Cr-7.5Mo \qquad (3.1)$$

And the Cr, Ni equivalent formulas of Schaeffler diagram added the influence of Al on ferrite phase formation as follows [9]:

$$Cr_{eq} = Cr + 2.5Al + 1.8\,Mo + 2Nb + 2.5Si \qquad (3.2)$$

$$Ni_{eq} = Ni + 30C + 0.5Mn \qquad (3.3)$$

15Cr-2Al-2Ni-12Mn and 15Cr-2Al-8Ni alloy were chosen as the experimental materials, which exhibit the same Cr_{eq} and Ni_{eq}, but different M_s, as exhibited in Table 3.1. Based on the Schaeffler diagram as shown in Fig. 1.1, both compositions locate at the same point and result in the DSS. If the Schaeffler diagram is used, the ferrite content may be about 20%. However, our following investigation will show that the volume fraction of ferrite or austenite can be varied in a wide range.

Table 3.1 Cr_{eq}, Ni_{eq} and Ms of 15Cr-2Al-2Ni-12Mn and 15Cr-2Al-8Ni castings

Alloy	Cr_{eq}	Nieq	M_s(°C)
15Cr-2Al-2Ni-12Mn	20	8	-51
15Cr-2Al-8Ni	20	8	207

3.2 Casting and microstructure identification

The raw materials were melted in an electric arc furnace and then sucked into a copper mould at room temperature. This device was usually used to synthesise metallic glasses since it achieves a cooling rate in the order of 10^3 °C/s. Here we utilize it to prepare the as-cast DSS which can substantially freeze its high-temperature phase constitution and microstructure. Extra Fe-Mn alloy were added in the raw materials, because Mn evaporates easily in the electric arc furnace. Although all DSSs solidifies ferritically, the subsequent air cooling in the conventional production process brings about a significant amount of austenite. For the composition we studied, the previous work [9] and WRC1992 diagram both indicate that the air cooling process results in about 30% δ-phase. However, using the copper-mould suction, 70% ferrite is resulted. The optical micrograph and XRD pattern of the two as-cast alloys are shown in Fig. 3.1. XRD confirms their dual-phase structure and relative proportionality (in terms of heights of peaks). 15Cr-2Al-2Ni-12Mn is constituted by 70% ferrite and 30% γ-phase, while, 15Cr-2Al-8Ni is of 70% δ and 30% martensite phases. It indicates the significant role of Manganese in suppressing the formation of martensite phase. We then fix the resource-saving DSS composition to be 15Cr-2Al-2Ni-12Mn and pay our attention to the subsequent heat-treatment. And its specific chemical composition after spectroscopic analysis is shown in Table 3.2.

Table 3.2 The specific chemical compositions 15Cr-2Ni DSS (wt.%).

Element	Fe	Cr	Al	Ni	Mn	C
Wt.%	Balance	17.05	2.05	1.88	12.73	0.02

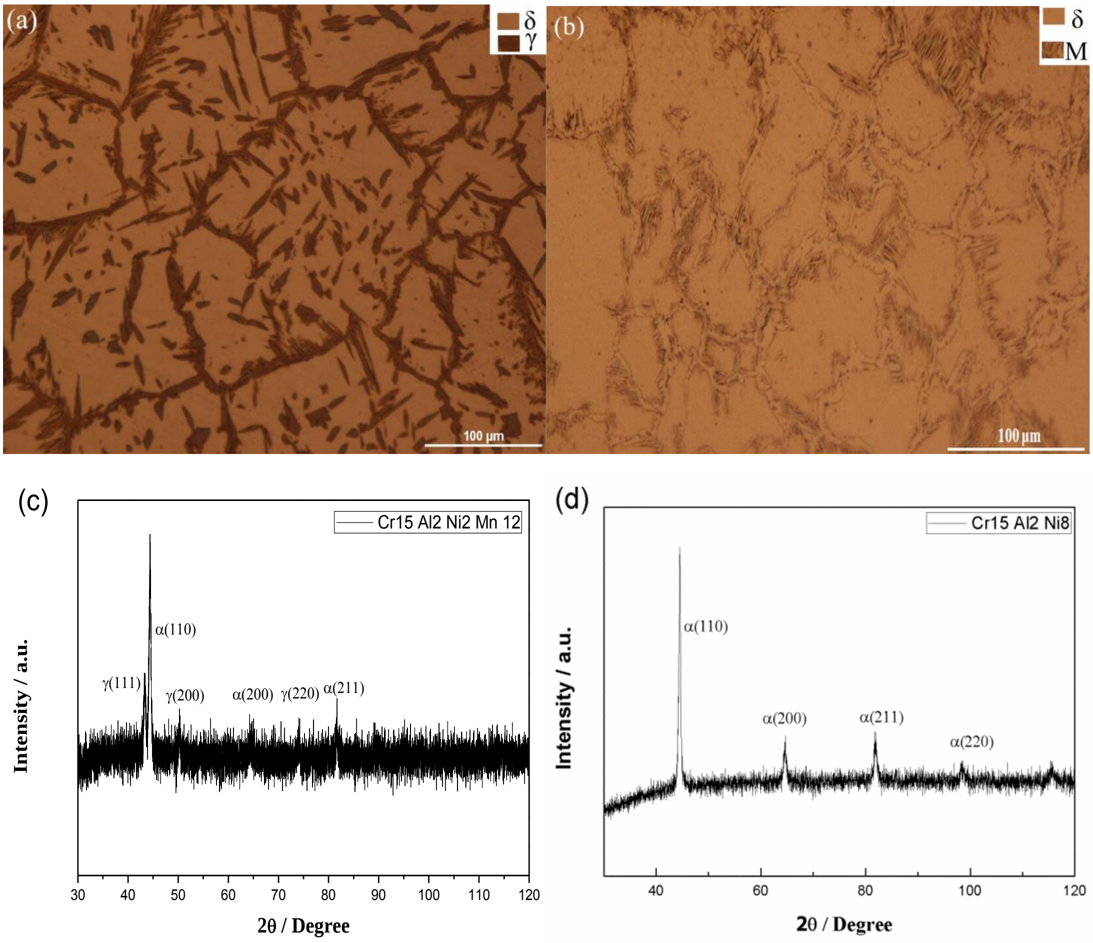

Fig. 3.1 The metallographs (a) 15Cr-2Al-2Ni-12Mn and (b) 15Cr-2Al-8Ni and X-ray diffraction pattern of (c) 15Cr-2Al-2Ni-12Mn and (d) 15Cr-2Al-8Ni of the as-cast alloys.

3.3 Experimental schedule

The research is based on 15Cr-2Ni-2Al-11Mn alloy. The as-cast alloy is very ductile, which can be cold rolled with 70% reduction of the thickness. The as-cast sample has element segregation issue. To limit this issue, the casting sample was controlled in small size, all samples were cut from the same depth of the ingot, and the centre region of each heat-treated sample was examined to avoid any boundary effect. Both the as-cast and cold-rolled (rolled at room temperature) specimens were subjected to various heat treatments without high temperature homogenization which changes the volume fraction and grain size of the primary phase of DSS samples. We want to get the link between the casting DSS and its resulted property. Eg. Phase transformation, we want to predict the ferrite content after different heat treatment according to the TTT diagram once the chemical composition is fixed. The samples were heat treated in the furnace at 750 ~ 1250 °C for 1 ~ 240 min (as shown in Table 3.3) and then cooled to room temperature through water quenching, air cooling or furnace cooling. In the experiment of sigma phase formation, the DSS samples were undertaken aging at 750, 850, 900 and 950 ºC for 150~1400 min followed by water quenching. The presence of sigma phase in DSS samples is determined by metallography. The transformation kinetics and phase constituents were examined and directly measured by quantitative analysis using standard metallographic techniques.

Table 3.3 Heat treatment schedule of 15Cr-2Ni DSS samples

Temp., °C	Time/min														
	1	3	5	10	15	20	30	45	70	90	120	150	180	210	240
750							■	■	■	■	■	■	■	■	■
850					■		■	■	■	■	■	■	■	■	■
950			■	■	■	■	■	■	■	■	■				
1050	■	■	■	■	■	■	■	■	■						

3.4 Characterization methods

To reveal the two primary phases, the specimens were electrolytically etched in 15 wt.% KOH solution, which made the austenite bright and the ferrite dark under an optical microscope. The average phase constitution was calculated from 10 data, which every data is obtained from an area of approximately 730000 μm^2 of the specimen surface using metallography image analysis software. The sigma phase content is also calculated using metallography image analysis software by setting a proper color reading value. Though the image analysis method is commonly adopted in metallurgy research and also for DSS, we acknowledge that the area fraction is not identical to the volume fraction. In order to make sure that the calculated area fraction does not deviate too much from volume fraction, we also calculate the area fraction from lateral surfaces and from different depths. The data points later shown are averaged results with an estimated error of about ±2%.

DSS specimens with half content of ferrite phase (45% ~ 55%) but obtained from different heat treatment processes were subjected to tensile tests. For tensile test, all samples were wire-cut into dog-bone shape with the gauge dimension of 5×30×1 mm, to which a 25-mm extensometer can be attached for an accurate measurement of the elongation. Micrographs on the fracture surface of samples after tensile test were observed in a Jeol 7490 scanning electron microscope (SEM). Selected samples were subjected to investigation using transmission electron microscope (TEM, JEOL 2000FX working at 200 kV). The samples were thinned into 30 μm by sand paper, punched into wafers of 3 mm diameter and ion milled to get the TEM foils. Finally, these specimens were ion-milled to obtain the TEM foils. TEM was performed on JEOL 2000FX at 200 kV to determine the crystallographic features of some possible secondary phases. The crystallographic analyses of precipitates and matrix were accompanied by a selected area diffraction pattern (SADP) measurement, and an energy dispersive X-ray spectrometer (EDS) was used for composition analyses. The Vickers indentations were performed with a load of 250 mN during 10s using FM-7E, FUTURE-TECH JAPAN. For each sample, a minimum of 10 indentations were performed. Nano-indentation is performed with Berkovich tip using load-control process with the maximum load 8000 μN, loading rate 1700 μN/s and dwell time 2 seconds using Hysitron. The alloy in corrosion behavior was investigated using potentiodynamic polarization curves and ASTM G48-03 standard corrosion test [18]. Polarization test was conducted using potentiodynamic polarization electrochemical methods and evaluated in solution of 3.5 wt.% NaCl at 25 °C. The experiments were carried out in a 200 ml conventional three-electrode cell comprising the sample as the working electrode, a Pt foil as the auxiliary electrode and a saturated calomel electrode as the reference one. Prior to testing, specimens were mechanically polished to 800 grit abrasive paper, washed with distilled water, degreased with acetone and dried in air. The interface between sample and resin were coated with a polyacrylate quick-setting resin, so as to prevent the possibility of crevice corrosion during measurement. Polarization test of each specimen was performed at least three times using an EG&G Princeton Applied Research Potentiostat/ Galvanostat Model 273A. Before the scan was initiated, the specimens were allowed to remain in the pitting solution for 10 min so as to stabilize the open-circuit potential (OCP). Potentiodynamic polarization curves were recorded started from -0.2 V to 1.5 V with respect to OCP. The value of potential where the current increases sharply from the passive current level was called the pitting corrosion potential.

Chapter 4. Non-equilibrium phase transformation in 15Cr-2Ni-2Al-11Mn duplex stainless steel

This work investigates the effect of annealing temperature and time, cooling rate, and plastic deformation on the phase transformation of 15Cr-2Al-2Ni-11Mn. The plastic deformation was caused by 70% cold rolling on the DSS sample.

4.1 Microstructural change by cold rolling

Fig.4.1 (a) shows the microstructure of the as-cast (AC) casting which shows approximately 30% austenite phase with dendrite crystal. Fig.4.1 (b) shows the 70% cold rolled (CR) casting, and it shows apparently elongated dendrite crystal.

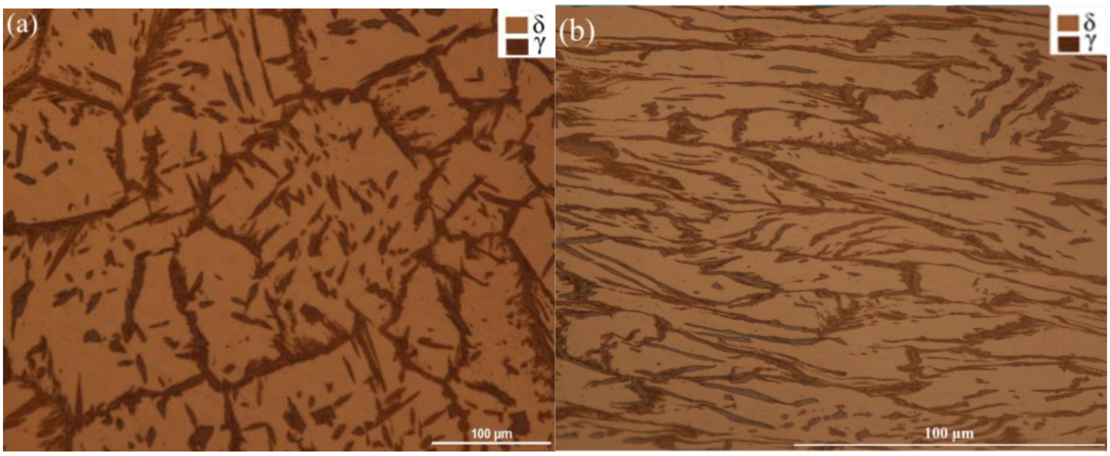

Fig.4.1 Metallographs of (a) AC casting (b) CR casting

4.2 An overview of microstructures after different heat treatments

In order to let reader has a quick overview of the effect of annealing temperature, time, cooling rate and plastic deformation, we select five samples for a brief description. Fig. 4.2a) shows the result using the conventional approach, in which the CR sample isothermally hold at 1050 °C for 30 minutes and finally water quenched, therefore denoted as CR-1050-30-W. The γ-phase, amounting to 41% volume, is those white islands embedded in the continuous δ phase matrix. No secondary precipitates were found in the ferrite-ferrite and ferrite-austenite phase boundaries. The two phases were further confirmed by XRD analysis as shown in Fig. 4.2(b). In Fig.4.2(b), the effect of cooling rate is also exhibited in terms of the change of the relative height of the peaks pertaining to the γ(111) and δ(110) planes. After the analysis of optical micrographs of CR samples heated at 1050 °C for 30 mins, it is revealed that the volume fraction of γ-phase ϕ_γ increases from 41% to 72%, when the cooling rate reduces from water quenching to furnace cooling. As a comparison, the sample CR-850-30-W, as shown in Fig.4.2(c), demonstrates that annealing at lower temperature leads to much smaller but the larger quantity of separated γ-phase. If annealing time increases, the case CR-850-90-W, as shown in Fig.4.2(d), demonstrates that γ-phase grew larger and coalesced. Cooling rate shows similar effect. When the cooling rate is slower, γ-phase in the sample CR-850-30-F becomes larger and more equiaxed than that in sample CR-850-30-W as shown in Fig.4.2(e). The effect of plastic deformation can be exemplified by Fig.4.2(f), in which the AC sample is heat-treated using the process of AC-850-30-W. Compared to Fig.4.2(c), it indicates that plastic deformation leads to much smaller γ-phase. The dual-phase microstructure can be further confirmed using TEM. Fig.4.3 shows the interface of δ and γ grains taken from CR sample solution-treated at 750 °C for 30 min followed by water quenching.

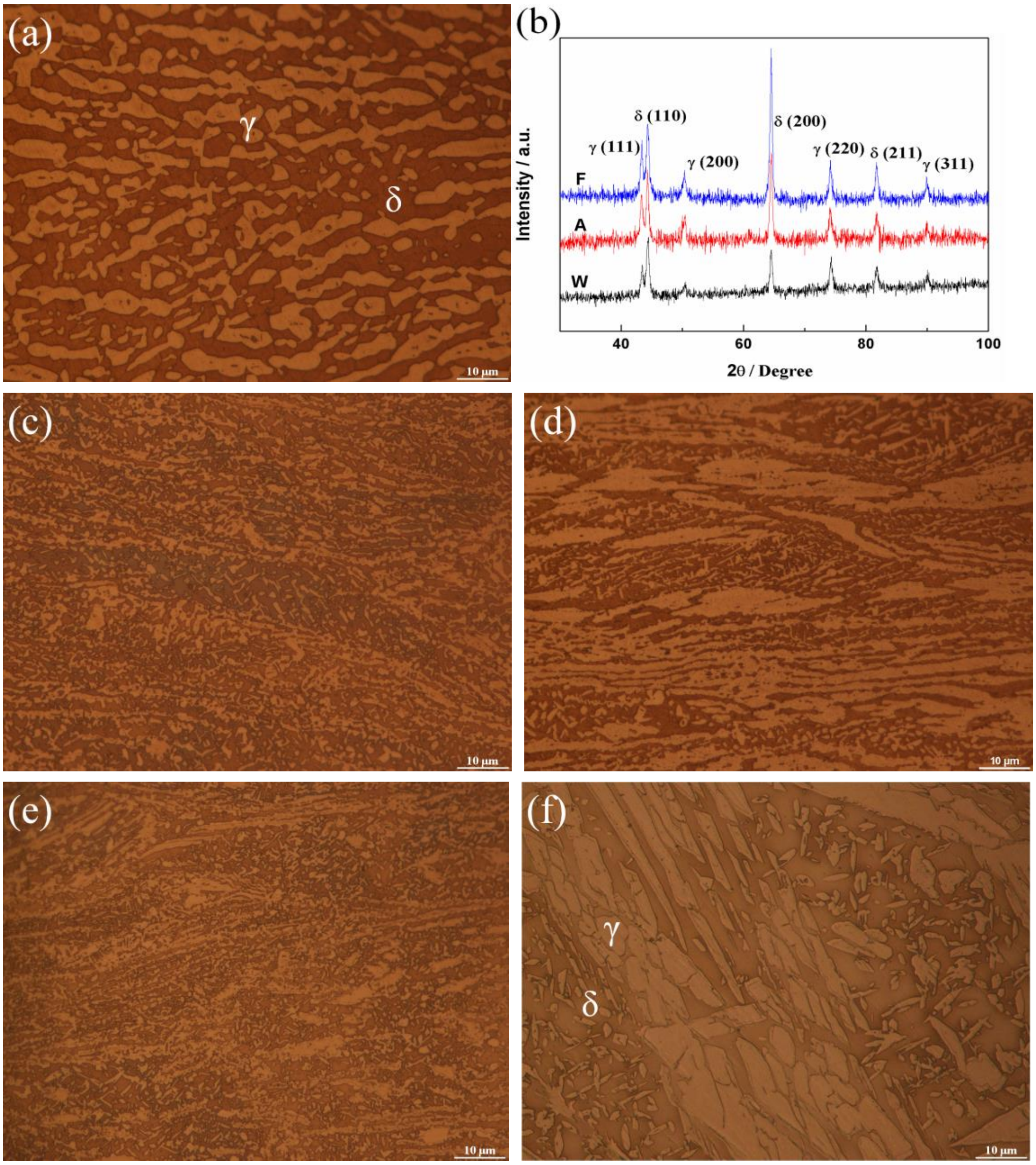

Fig. 4.2 An overview of metallographs (a, c-f) and XRD pattern (b) of DSS samples: (a) CR-1050-30-W, (b) CR-1050-30-W, CR-1050-30-A and CR-1050-30-F, (c) CR-850-30-W, (d) CR-850-90-W, (e) CR-850-30-F and (f) AC-850-30-W

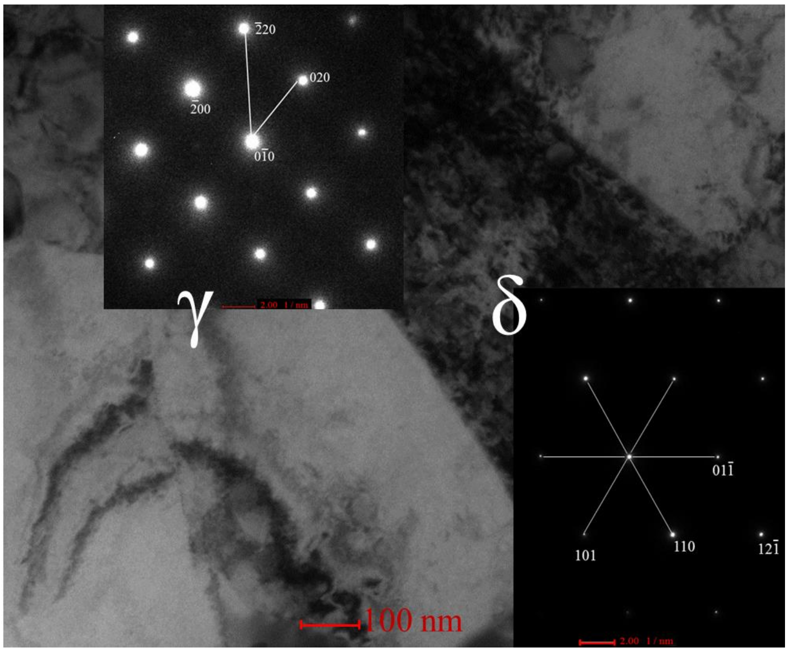

Fig. 4.3 The typical TEM images taken from δ/γ interface of CR sample solution-treated at 750 °C for 30 min followed by water quenching

4.3 Microstructural evolution during isothermal annealing

Fig.4.4(a)~(d) show the metallographs of the CR samples annealing at 950 °C for 1, 3, 30, 70 min followed by water quenching, respectively. Fig.4.4(a) shows the unexpected truth that phase transformation occurs at 950 °C even for 1 min holding, and it shows the totally nucleation scene. δ/γ boundary shows most austenite nucleation, and the ferrite interior also has. For 3 min annealing as shown in Fig.4.4(b), the newly-formed γ grains apparently grow coarser. Then for 30 min annealing as shown in Fig.4.4(c), the newly-formed γ grains became nearly-spheroidized. Last, 70 min annealing as show in Fig.4.4(d) shows coarser but similar amount of γ-phase compared with Fig.4.4(c). It indicates that the δ-to-γ phase transformation reaches the thermos-equilibrium state within 30 min.

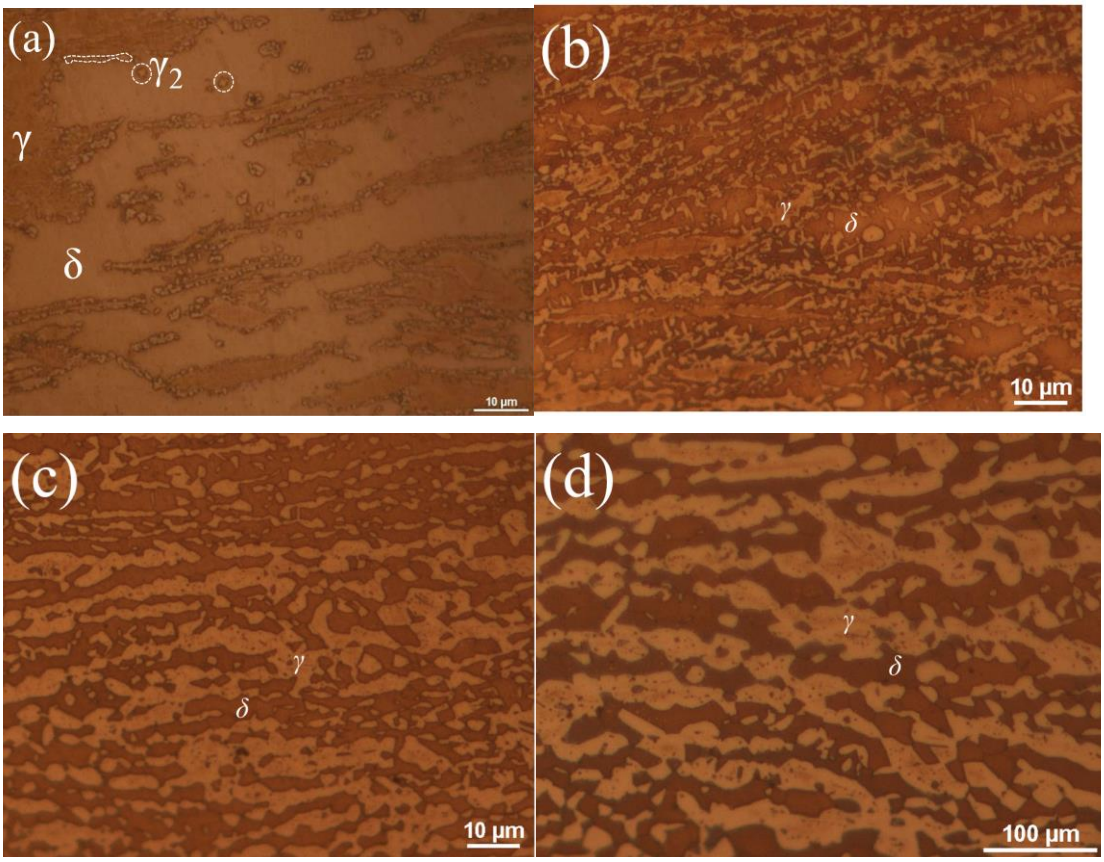

Fig.4.4 Metallographs of (a) CR-950-1-W (b) CR-950-3-W (c) CR-950-30-W (d) CR-950-70-W

4.4 The quantitative effects of annealing temperature, time and cooling rate

The variation of γ-phase in the DSS samples annealing at 750 ~ 1050 °C for 1~240 min followed by water quenching is shown in Fig.4.5. It is interesting to find that the volume fraction of γ-phase increases with annealing time and finally reaches a constant value. It can be concluded that the δ-to-γ phase transformation occurs and reaches a thermo-equilibrium state after long enough annealing. Also, γ-phase increases with annealing temperature. The variations of the volume fraction of the ferrite phase ϕ_δ against annealing temperature T for different annealing time is summarized in Fig. 4.6. It should be noted that the δ-phase content is the water-quenched result instead of the high-temperature result. Fig.4.6 illustrates two cases. For Case I, the annealing time is set to 30 minutes. For case II, the annealing time is sufficient long that the quenched ferrite content does not change further with longer time. We name it quasi-equilibrium content since they are not the exact high-temperature value but the quenched result. The two cases shown in Fig. 4.6 are remarkably different especially in the temperature range of 750 ~ 1050 °C. This manifests the influence of annealing time and indicates that annealing for 30 min at 750 ~ 1050 °C is insufficient for equilibrating phases. For the case I, the content of ferrite phase decreases with annealing temperature T when it is lower than 1050 °C, which is seemingly against the general understanding that more ferrite phase will be transformed to austenite phase at lower temperature. Based on case II, it is clear that the equilibrium ferrite content increase with temperature. It is noted that when T is higher than 1050 °C, the ferrite content surges. The microstructure became almost fully ferritic at 1150 °C for the CR samples and 1250 °C for the AC ones. Since the as-cast material contains about 70% δ, the critical temperature T_{cr} can be concluded, below which the net phase transformation is δ-to-γ and vice-versa. T_{cr} shall be a temperature between 1050 and 1150 °C.

The different tendency of phase transformation when T is lower or higher than T_{cr} can further be elucidated using the short-duration of 1 min and 10 s isothermal treatment (followed by water quenching). Fig.4.7(a) and Fig.4.7(b) show the micrographs of CR-950-1-W and CR-1150-0.17-W, respectively. In Fig. 4.7(a), it is observed that γ_2 phase of scale-like morphology nucleates in grain boundary and δ-phase interior. In Fig.4.7(b), the γ-phase islands are decomposed from the boundary. This decomposition process leaves the feather-line γ-phase, which may be the consequence of heterogeneous diffusion.

The effect of cooling rate for Case I is summarized in the inset of Fig.4.6, in which the water quenched samples were used as reference. That is, the results indicate the difference of δ content $\Delta\phi_\delta$ if the cooling rate reduces from that of the water quenching. The air and furnace cooling only lead to no more than 5% and 21% reduction in δ content respectively when the temperature is below 1050 °C. The magnitude of reduction rises more or less linearly with temperature. This difference $\Delta\phi_\delta$ quickly increases with temperature when the temperature is higher. However, it should be noted that the difference significantly reduces when the sample is cooled from 1250 °C, at which the material becomes fully ferritic. Even furnace cooling cannot notably increase the content of γ-phase. After investigating the microstructures of the sample heated at 1250 °C, it is found that the ferritic grains have grown to be very large, which minimizes grain boundaries and makes the nucleation site of γ-phase very rare.

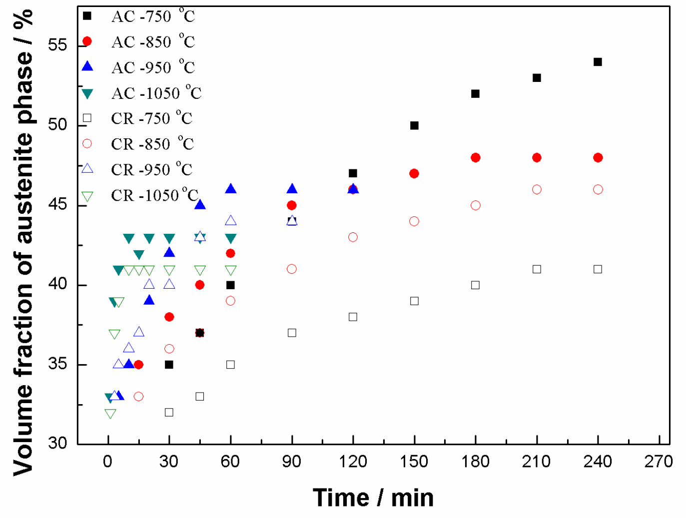

Fig.4.5 Variations of austenite phase in DSS samples annealing at 750~1050 °C for 1~240 min

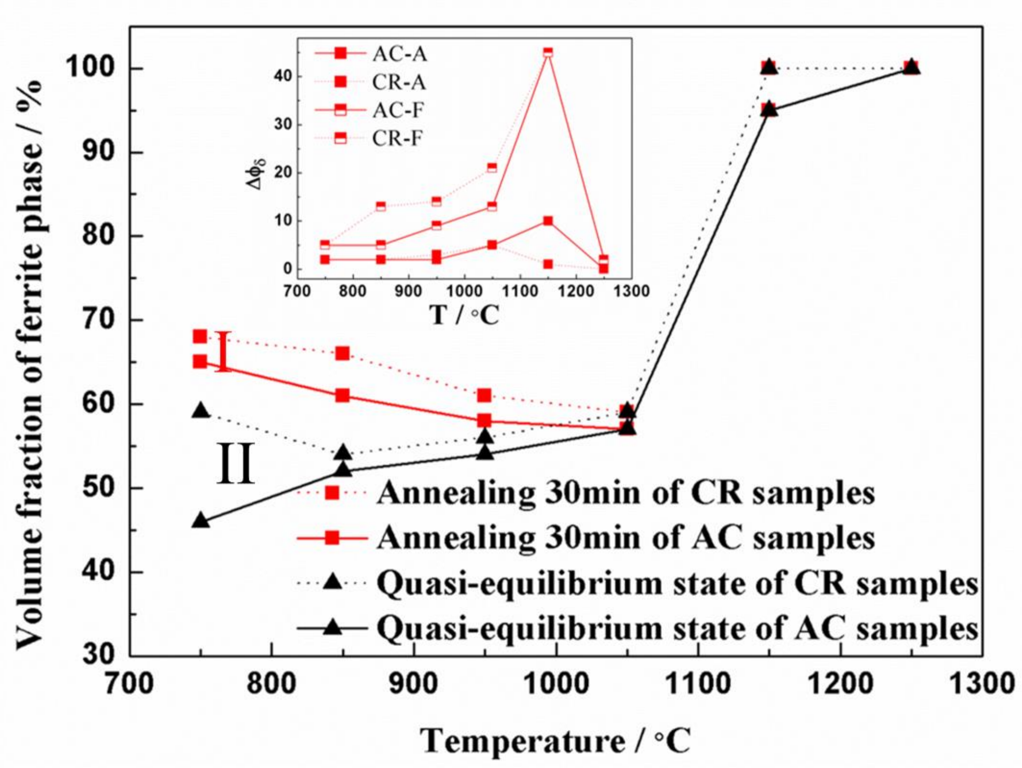

Fig. 4.6 The variation of room-temperature ferrite content with heating temperature: the samples were held for (I) 30 min and (II) a sufficiently long time followed by water quenching, respectively. The inset shows the effect of air cooling and furnace cooling for (I).

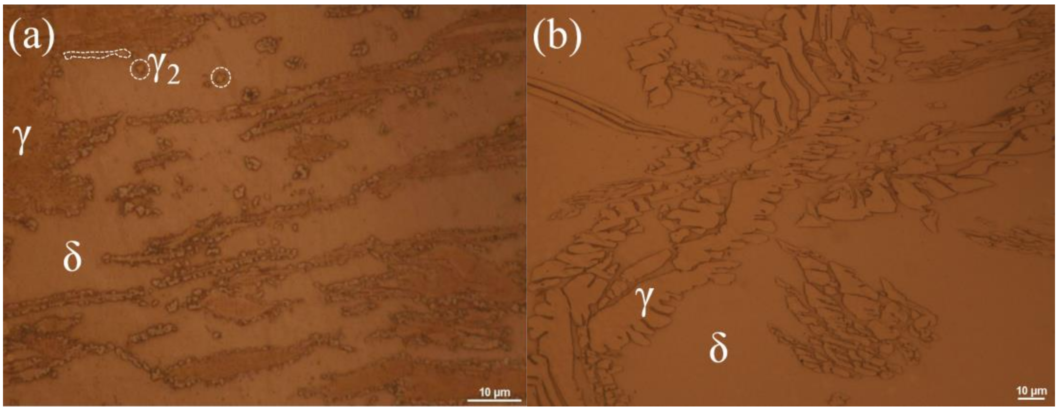

Fig.4.7 The metallographs of samples (a) CR-950-1-W and (b) CR-1150-0.17-W for demonstrating nucleation of γ_2 phase

4.5 TTT diagrams based on water quenched samples

δ-to-γ transformation occurs at 750~1050 °C, so the TTT diagram for both AC and

CR samples heat treated below 1050 °C followed by water quenching were established. The results are fitted using the Avrami equation [80, 81]:

$$f = \phi_\gamma / \phi_\gamma^e = 1 - \exp(-(t/\tau)^n) \tag{4.1}$$

Where f is the fraction transformed, ϕ_γ is the volume fraction of γ-phase at time t, ϕ_γ^e is the volume fraction of γ-phase at the thermal equilibrium state, which is determined based on the experimental results when the ϕ_γ remains unchanged if the annealing time is doubled. Since the samples have 30% γ-phase before heat treatment, we assume the time in Eq. (4.1) does not start from zero but from t_0. Therefore, Eq. (4.1) is modified to:

$$\phi_\gamma / \phi_\gamma^e = 1 - \exp(-((t + t_0)/\tau)^n)\,. \tag{4.2}$$

Eq. (4.2) can be recast as:

$$\ln(-\ln(1 - \phi_\gamma / \phi_\gamma^e)) = n\ln(t + t_0) - n\ln\tau\,, \tag{4.3}$$

The exponent n is considered to be close to 2.5 [58], which is based on a simplified model for diffusion mediated phase transformation, to be described in Chapter 8. Therefore, in fitting the data points, the initial time t_0 is adjusted to ensure that the experimental data points are along the straight line. Fig. 4.8 shows the experimental data and fitting lines in the log-log plot. The magnitudes of fitting parameters n, τ, t_0, ϕ_γ^e are listed in Table 4.1. Fig. 4.9 shows the experimental results and fitting curves on the temperature-time dependent variation of γ content, which exhibits the non-equilibrium kinetics and the equilibrium state of 15Cr-2Al-2Ni-11Mn alloy. For confirming the fitting, heat-treatments were conducted based on the fully ferritic samples obtained after annealing at 1250 °C for 30 min. The fully CR ferritic samples were then aged at 750, 850, 950 and 1050 °C followed by water quenching, respectively. The aging result leads to the pentagrams in Fig. 4.10, which are all along the fitting curves. The inset shows the microstructures of some samples.

The Avrami equations were then used to establish TTT diagrams of γ-phase formation, as shown in Fig. 4.11. It is noted that the growth rate of γ-phase increases with annealing temperature and that the γ-phase formation in AC samples is faster than that in CR samples. If we define the time needed for γ-phase content increasing from 0% to 1% as the breeding time, the breeding time is about 80-90 min at 750 °C and 1-2 min at 1050 °C for both AC and CR samples.

Table 4.1 Fitting parameters of Avrami equation for δ-to-γ phase transformation in DSS

	T (℃)	τ (min)	n	t_0 (min)	ϕ_γ^e (%)
As-cast	750	305.40	2.80	280.00	54
	850	192.90	2.30	200.00	48
	950	71.10	2.49	70.00	47
	1050	11.30	2.80	12.00	43
Cold-rolled	750	374.30	2.70	399.00	41
	850	247.50	2.50	253.00	47
	950	72.90	2.52	78.50	44
	1050	12.00	2.79	13.20	41

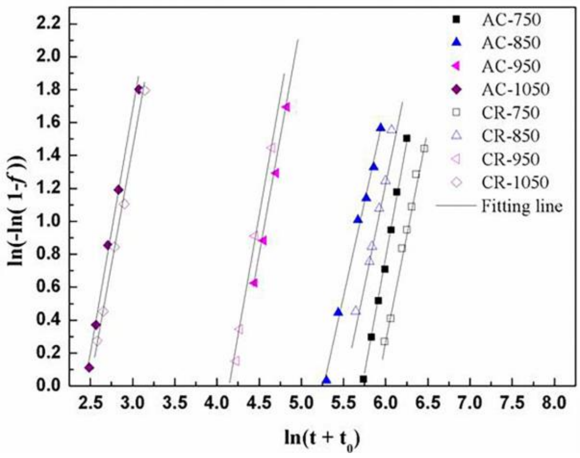

Fig. 4.8 Experimental results and fitting curves on the temperature-time dependent variation of γ phase content plotted in log-log-scale

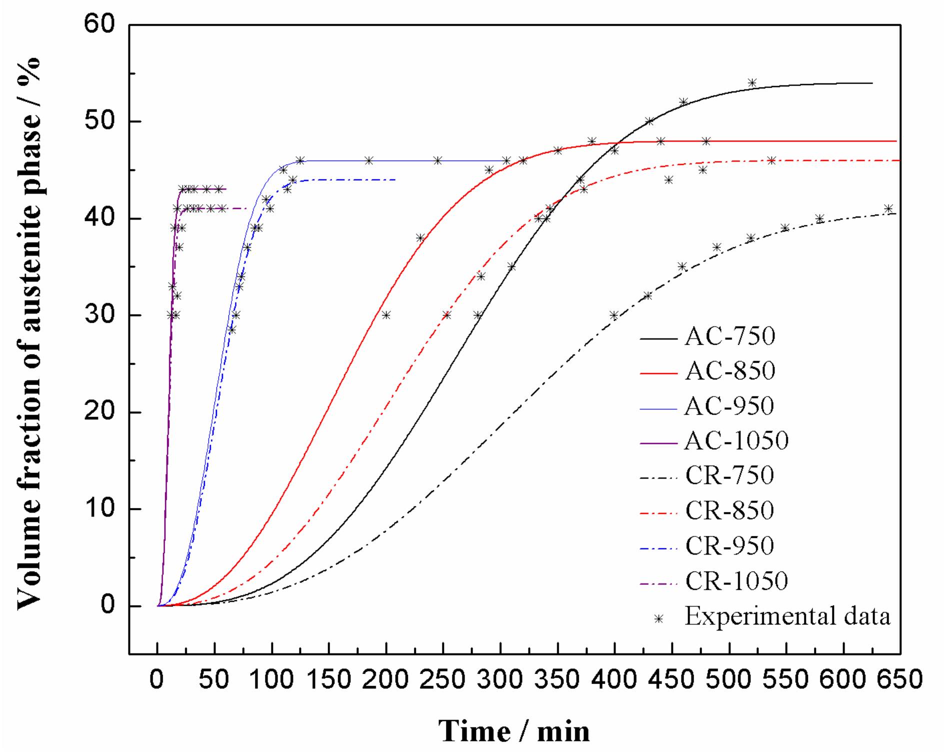

Fig.4.9 Experimental result and fitting curves on the temperature-time dependent variation of γ phase content for AC and CR samples of 15Cr-2Ni DSS

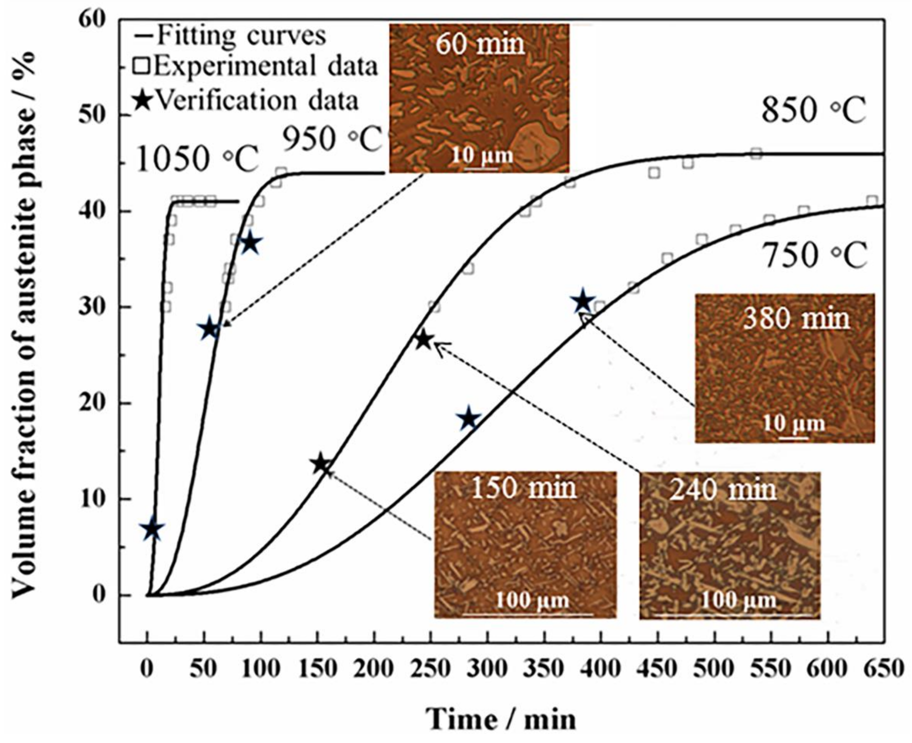

Fig. 4.10 For confirming the fitting, heat treatment based on fully ferritic CR samples was also conducted, leading to the additional pentagram points on the experimental result and fitting curves on the temperature-time dependent variation of γ phase content for CR samples.

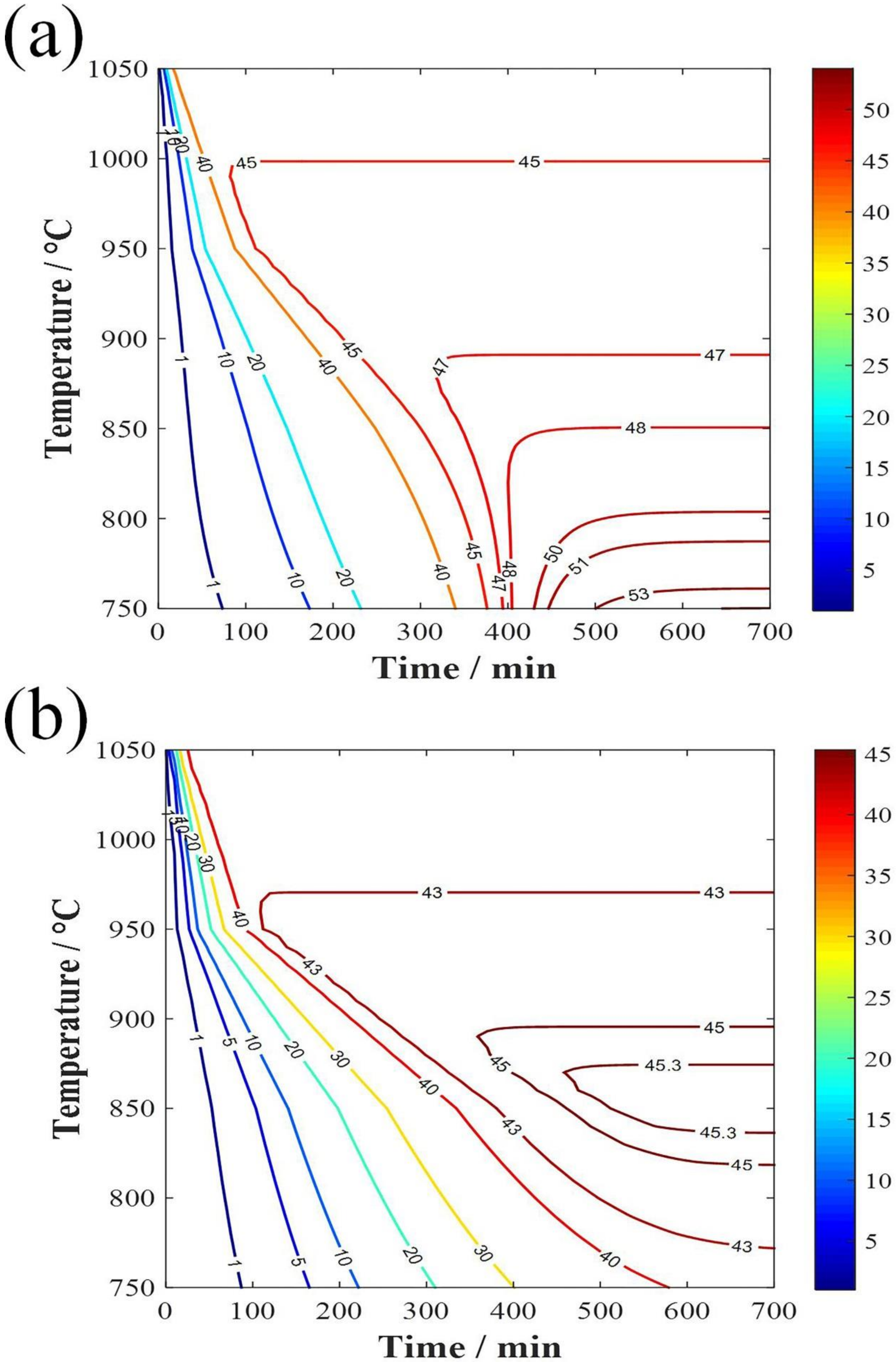

Fig. 4.11 TTT diagram of γ phase volume fraction of (a) as-cast and (b) cold-rolled samples

4.6 Discussion

4.6.1 On the role of plastic deformation in phase transformation

It is well known that rolling leads to “pancake” grains, which is an effective approach to obtain small grains in the process involving phase transformation, since nucleation of new phase preferably starts at grain boundaries and the pancake-shaped grains limited the space of grain growth. It is also conceived that severe plastic deformation induces more internal energy owing to the high density of defects, which shall bring about faster phase transformation. However, this is not true in our case. In Table 4.1, the time τ indicates the characteristic time for phase transformation. Comparing τ of AC and CR samples at different temperatures, it is noted that the ferrite-to-austenite phase transformation of CR sample is slower than that of AC. And the plastic deformation reduces not only the rate of phase transformation but also the equilibrium content of γ-phase.

To corroborate the effect of plastic deformation, the AC and CR samples were investigated using differential scanning calorimeter (DSC, PerkinElmer DSC7) under the heating rate of 25 °C/min, as shown in Fig. 4.12. For the AC and CR samples, the exothermic peaks at about 570 and 720 °C are found respectively, which indicates that the plastic deformation defers the δ-to-γ phase transformation. The metallographs at the temperatures before and after the peak are shown in the inset. Fig. (a) and Fig. (b) pertain to the samples AC-550-30-W and AC-700-30-W, and the newly-nucleated γ_2 phase can be found in (b) but no γ_2 in (a). Similarly, the metallographs of the sample

CR-700-30-W (inset (c)) has no γ_2, while that of CR-750-30-W (inset (d)) has.

The DSC results confirm that plastic deformation suppresses the δ-to-γ transformation at low temperature. Since the δ-phase has smaller atomic packing factor than γ-phase, one may loosely hypothesis that the δ-to-γ transformation is exothermic and that γ-*to*-δ is endothermic in DSS [1, 9, 82]. Noting that plastic deformation introduces additional mechanical energy to the material owing to the distorted lattices surrounding defects. This additional energy suppresses the exothermic reaction, as manifested by the retarded δ-to-γ transformation at low temperature, but helps the endothermic one, as manifested by the fact that the CR samples achieve the fully ferritic structure at the lower temperature than that of AC counterparts (Fig. 4.6 (II)). Higher temperature makes the atomic system more active and reduces microstructure defects. Therefore the effect of plastic deformation should be reduced with the increase of temperature. On the other hand, higher temperature leads to less equilibrium content of γ-phase. The combination of these two effects, as sketched in Fig. 4.13, makes the equilibrium content of γ-phase in CR samples approaches a maximum magnitude at about 850 °C, which explains the difference between Fig. 4.11(a) and Fig. 4.11(b). And the shaded area in Fig. 4.13 quantifies the effect of plastic deformation at different temperatures.

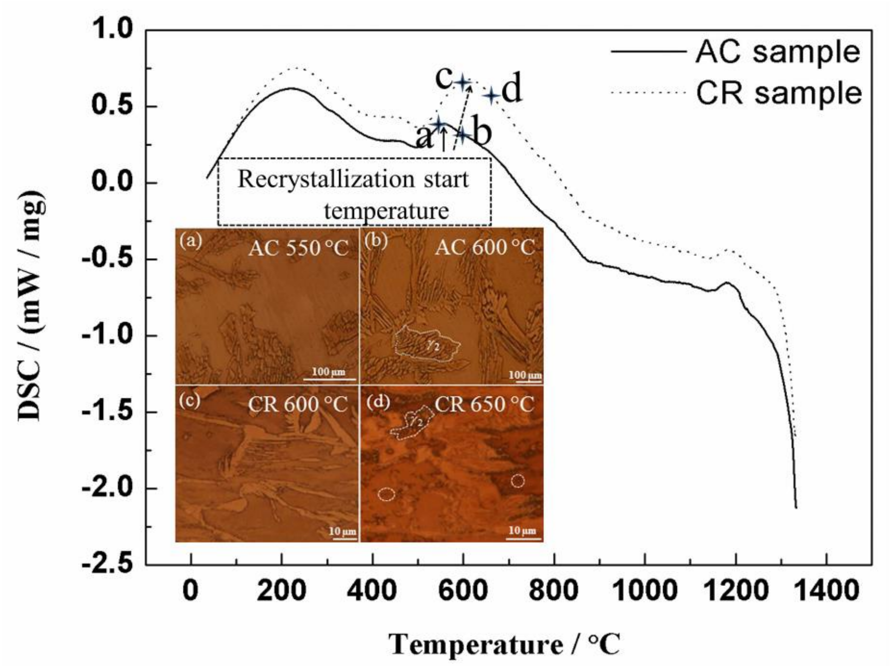

Fig. 4.12 DSC curves of as-cast and cold-rolled samples. The insets show the metallographs before and after the exothermic peak.

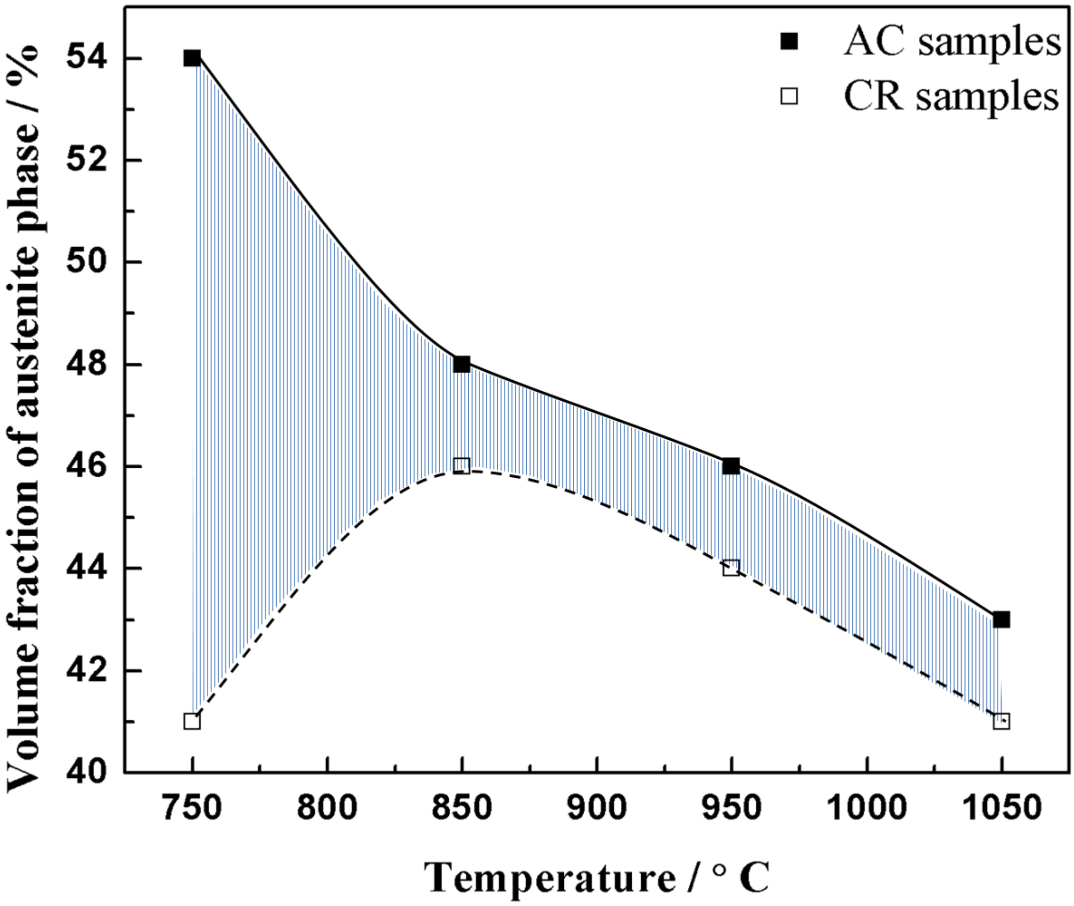

Fig.4.13 The effect of plastic deformation on γ phase formation of DSS samples

4.2.2 The accessible range of phase constitution

In the conventional synthesis approach of DSS, the melt is generally slowly cooled in furnace or air, which usually results in a small content of δ owing to the δ-to-γ transformation when temperature reduces. For the 15Cr-2Ni DSS, air cooling generally brings about 40% δ in the as-cast sample [9]. However, in this work, the quick quenching using copper mould suction is employed, which leads to the 70% δ in the as-cast sample. The justification for the present approach can be understood using the diagrams shown in Fig. 4.14.

To elaborate the design of the thermal process for adjusting the phase contrast in DSS, the equilibrium δ content of both cold-rolled and as-cast samples against temperature 750~1250 °C, which is approximated by water-quenched samples after sufficient long time annealing, is plotted in Fig. 4.14. Sufficiently long time annealing herein means that the quenched δ content does not change further when the annealing time is double. If the preheated sample consists of 40% δ as the dashed line shown in Fig. 4.14(a), isothermal holding leads the δ content to the equilibrium magnitude and cooling reduces the content of δ. The blue shaded area in Fig. 4.14(a) indicates the accessible range of δ content through heat treatment. If the target δ content in the DSS is 50%, it is then apparent that the accessible temperature range of heat treatment must be larger than the intersection point (about 850 °C) between the 50% reference line and the equilibrium curve.

However, if the δ content of the preheated sample is 70%, as shown in Fig. 4.14(b), the additional accessible range of δ content is indicated as the grey shaded area, in which heating leads to reduction of δ content. And the 50% δ content can be obtained easily at the low temperature range of 750~850 °C. In general, diffusion of alloy elements and grain growth are slower at lower temperature. Therefore, if a range of annealing temperature can be chosen for achieving a given volume fraction of δ/γ phase in DSS, annealing at lower temperature may have the advantage of better control of microstructure.

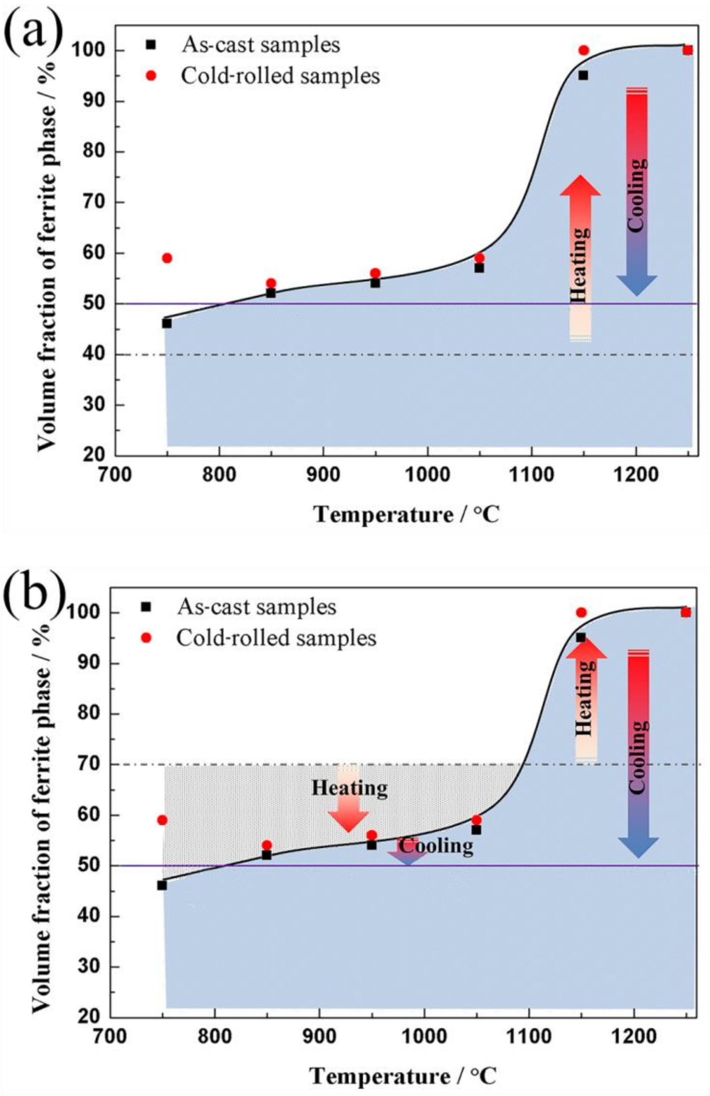

Fig.4.14 Accessible range of heat treatment for DSS with δ content of (a) 40% and (b) 70%

4.7 Conclusion

This work investigates the effect of annealing temperature and time, cooling rate, and plastic deformation on the phase transformation of 15Cr-2Al-2Ni-11Mn. The main findings are:

1. The primary phase transformation is δ-to-γ when the annealing temperature is less than 1050 °C, but becomes γ-to-δ at higher temperature for rapidly-solidified DSS 15Cr-2Al-2Ni-11Mn.
2. Rapid solidification expands heat-treatment temperature to as low as 750 °C to achieve 50/50 duplex structure.
3. It is found that plastic deformation not only changes the rate of phase transformation and the grain size of new phase but also changes the equilibrium phase constitution. Plastic deformation suppress the transformation from δ-to-γ phase, while promotes the inverse one. After 70% cold rolling, the maximum austenitic content after long isothermal annealing occurs at about 850 °C. This effect of plastic deformation has never been reported before.
4. Based on Avrami equation, TTT diagrams of as-cast and cold-rolled DSS samples were established. It is found that the stretched exponent n is about 2.5 by fitting the experimental data, which can be explained based on a simplified model of diffusion-mediated phase transformation.

Chapter 5 Excellent combination of strength and ductility in 15Cr-2Ni duplex stainless steel based on ultrafine-grained austenite phase

The effect of temperature, time and cooling method on the phase evolution facilitates the synthesis of DSS of a desired phase constitution through different heat-treatment process. 70% cold-rolled DSS samples were used in different heat treatment and then conducted on the tensile test. These experiment were aimed to investigate the mechanical performance of DSS.

5.1 Mechanical Properties

In order to exhibit the impacts of different heat-treatment process on the mechanical properties, four different processes with annealing temperature 750 °C and 1000 °C were designed, which all bring about the DSS with about 50% δ phase. These are cold-rolled samples treated at 1000 °C for 15 min (S1) and 30 min (S2), and at 750 °C for 90 min (S3) followed by air cooling, which results in 52%, 50%, and 49% δ phase, respectively. As-cast sample treated at 1000 °C for 30 min followed by air cooling (S4) was also conducted on the tensile test to show the effect of plastic deformation on the mechanic property, and its δ content is 52%.

Fig. 5.1 shows the true stress-strain and work hardening rate curves of the four samples. The true stress-strain curves, after the yield point, are well fitted using the equation:

$$\sigma_T = \sigma_y + k\varepsilon^n, \tag{5.1}$$

where *k* and *n* are fitting parameters. The hardening rate is then $\frac{d\sigma_T}{d\varepsilon} = nk\varepsilon^{n-1}$, which has been shown in Fig. 5.1 for different samples. With the stress-strain relation, the nominal necking strain can be obtained using the Considere's criterion:

$$\left.\frac{d\sigma_T}{d\varepsilon}\right|_{necking} = \sigma_T, \tag{5.2}$$

which results in the end asterisks of the dashed fitting curves as shown in Fig. 5.1. The actual necking strain is about 70~80 % of the nominal one, which could be attributed to the internal voids resulted from casting[1]. The measured yield stresses, based on the fitting Eq. (5.1) or using the 0.2% proof stress, are listed in Table 5.1. All four samples exhibit good mechanical performance in terms of the yield strength of 307~499 MPa, ultimate tensile strength of 708~853 MPa and elongation of 20~33%. It is learned that severe plastic deformation before the heat treatment renders some constrains to the growth of γ-phase in the process of annealing [83], which makes the sample S2 stronger but less ductile than sample S4. The cold-rolling leads to two effects in producing DSS. Firstly, the severe plastic deformation induces many dislocations. These dislocated microstructures are the additional nucleation site (especially at high temperature) for the nucleation of γ grains from δ-phase. Secondly the rolling squeeze the grains, leading to the pancaked microstructure and smaller width of δ grains as shown in Fig. 5.2. The new γ grains then nucleate and growth from either grain boundary or grain interior of the deformed δ matrix. They are of various orientations, which may collide each other

---

[1] Forging can remove the internal voids and may further improve the ductility [8].

during growth and constrain the size of γ grains [44]. On the other hand, the more nucleation sites lead to the more separate γ-phase. In case of a fixed volume fraction of γ-phase, the size of them should be smaller. The latter can be corroborated by comparing Fig. 5.3(b) and (d). Comparing S1 and S2, the δ content of DSS reaches the equilibrium state after annealing at 1000 °C for 15 min as concluded from chapter 4, so both of S1and S2 undergo fully recrystallization. The δ content reaches thermal equilibrium state within 15 min, so grain size grows larger for the 30 min annealing and leads to the higher ductility but lower strength of S2. The metallographs of samples S1~S4 confirm the above description as shown in Fig. 5.3. Fig. 5.3(b) and Fig. 5.3(d) are very common DSS morphologies, which are the results of conventional 30 min annealing. For Fig. 5.3(a) and Fig. 5.3(b), the reduced annealing time led to many small γ-phases embedded in δ matrix in S1, which explains the higher yield strength in comparison with S2. It is estimated (through piece-wise linear interpolation) from Table 4.1 that the characteristic time τ at 1000 °C is about 35 minutes and t0 should be slightly (about 10%) larger than τ. Therefore, we can estimate using Eq. (4.1) that the 15-min annealing at 1000 °C has brought the material very close to, but still slightly different from, the equilibrium phase constituent. The calculated $\phi_\gamma / \phi_\gamma^e$ is about 95%. The interruption of annealing then leads to the microstructure shown in Fig. 5.3(a), which is the manifestation of nucleation of may needle-like γ-phase from δ matrix in the course of annealing. Therefore, in the course of further 15-minute annealing, growth of grains and rounding of phase boundaries would be the main process of microstructure evolution. A quick diffusion calculation at 1000 °C for 900 Seconds shows that the Cr diffusion distance in DSS to be between 1.4 and 3.3 microns [84]. In Fig.5.3(a), the average width of small needle-like γ-phase is about 1.3 μm. However, in Fig 5.3(b), the average width of thin γ-phase only increases to 2.7 μm. The difference in width of about 1.4 μm is consistent with the calculation result based on the diffusion of Cr. It indicates that γ phase can have bi-modal size distribution due to the growth from the new nucleus and existing ones respectively. This feature can be better controlled if the annealing temperature is reduced, as exemplified in Fig. 5.3(c), where a large number of even smaller γ-phases are exhibited. It is noted that the yield strength of S3 is lower than that of S1 and the ductility of S3 is even larger than that of S2. This low-temperature heat treatment brings about the best combination of strength and ductility as well as the largest hardening rate at large plastic strain. S1 and S3 exhibit the best strength and ductility respectively, which is consistent with the micrograph of fracture surface. S3 exhibits excellent combination of strength and elongation compared to other DSS alloys as shown in Fig 5.4. Fig. 5.5 exhibits the fracture surfaces of S1 and S3 using SEM. Fig. 5.5 (a) shows apparently brittle fracture feature of S1, while Fig. 5.5 (b) shows nearly all dimples feature of S3.

Table 5.1 Mechanical property and fitting parameters for true strain of DSS samples

Samples	$\sigma_{0.2\%}$ (MPa)	σ_y (MPa)	k (MPa)	n (MPa)	Nominal necking strain	Actual necking strain
S1	499	374	928.17	0.37	0.22	0.17
S2	349	308	947.91	0.52	0.33	0.23
S3	371	335	1017.47	0.55	0.35	0.28
S4	307	255	841.23	0.45	0.30	0.24

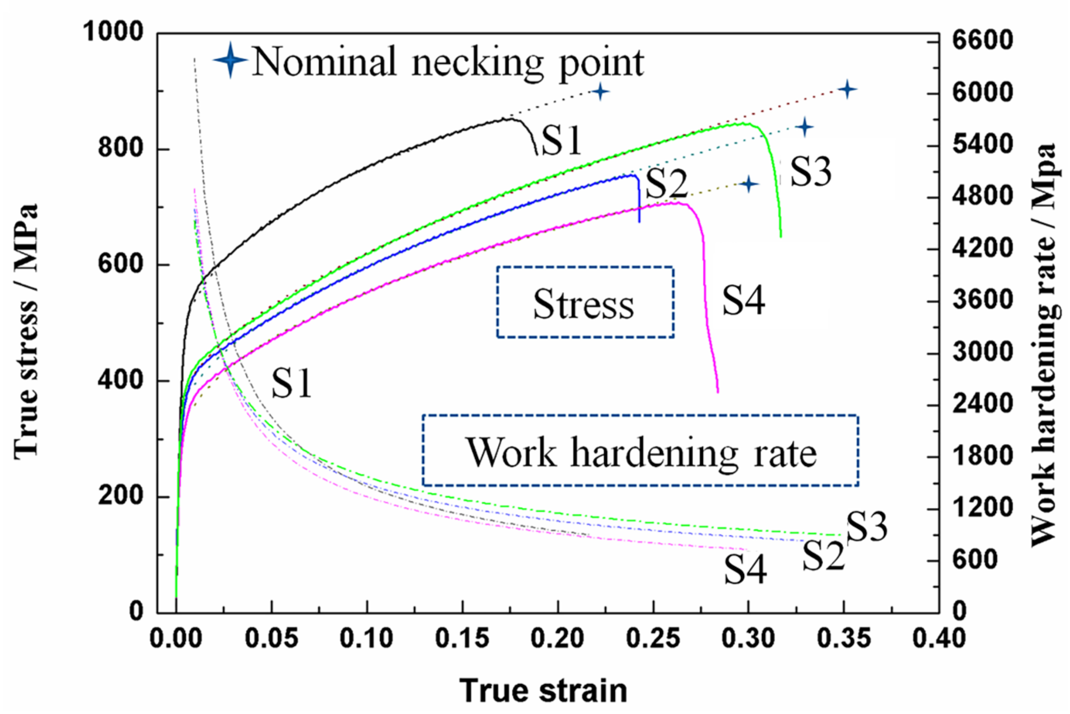

Fig.5.1 True stress-strain and hardening rate curves of cold-rolled DSS samples treated at 1000 °C for 15 min (S1) and 30 min (S2), and at 750 °C for 90 min (S3) and as-cast sample treated at 1000 °C for 30 min (S4). All of them were air-cooled after annealing.

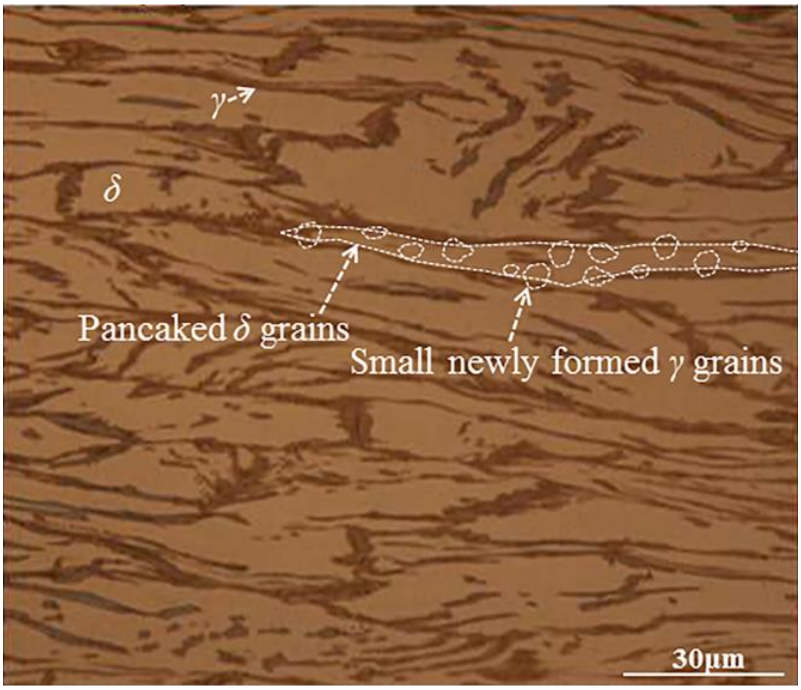

Fig.5.2 A schematic shows the role of plastic deformation before the heat treatment renders some constraints to the growth of γ-phase in the process of annealing.

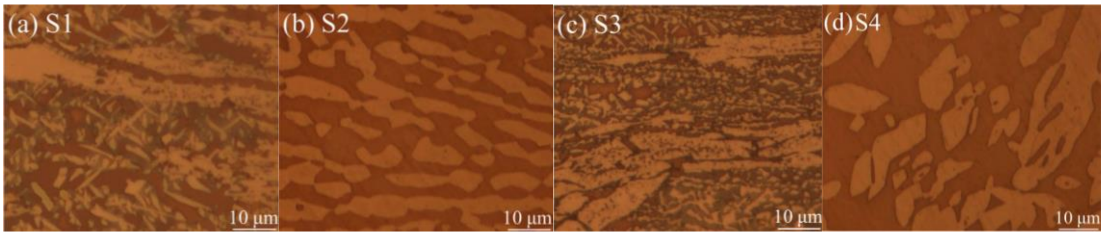

Fig.5.3 Metallographs of samples S1~S4

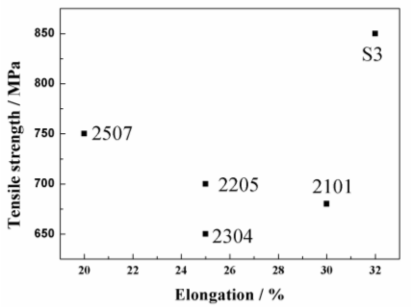

Fig. 5.4 The comparison between S3 and other DSS on tensile strength VS elongation

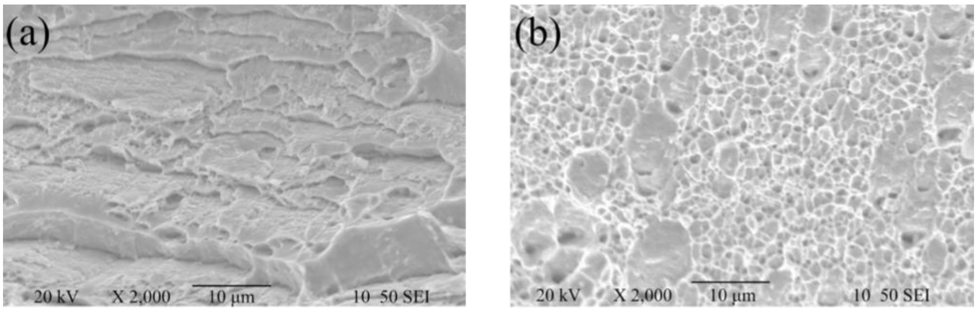

Fig.5.5 The SEM images of fracture surfaces of samples (a) S1 and (b) S3 after tensile test

5.2 Discussion

5.2.1 On the 750 °C heat treatment

Heat treatment is an effective step for improving the mechanical performance of DSS. The annealing temperature in the conventional process of adjusting phase constituent is around 1000 °C, at which the secondary phase such as σ-phase will not precipitate. The σ-phase usually forms between 700~900 °C and embrittles DSS [1]. However, the size and distribution of σ-phase can be controlled by adjusting the chemical composition and heat treatment, and the fine and homogenous dispersion of σ-phase can play a role of precipitation strengthening in stainless steels [85, 86]. In addition, heat-treated at lower temperature can not only reduce growth rate of grains but also keep more deformed and dislocated microstructures, leading to finer γ grains [45]. Therefore, low temperature heat treatment should be useful for improving the mechanical performance of DSS [44, 45, 87].

5.2.2 On the strength contrast of δ and γ-phases

In order to understand the mechanic mechanism of the contrast between S1 and S3, microhardness and nano-indentation tests on δ and γ-phases were conducted. The average microhardness values of δ and γ-phases of S1 and S3 is shown in Table 5.2.

Table 5.2 Microhardness value of δ and γ phases in S1 and S3 (HV)

	δ	γ
S1	307 ± 13	271 ± 5
S3	207 ± 18	373 ± 20

Table 5.3 Nano-indentation result of δ and γ phases in S1 and S3 (GPa)

	δ	γ
S1	3.22 ± 0.14	2.71 ± 0.13
S3	2.44 ± 0.15	3.54 ± 0.20

The indentation of micro-hardness test on the δ and γ-phases of samples S1 and S3 is shown in Fig.5.6. Nano-indentation result in Fig.5.6 is shown in Table 5.3. Berkovich tip, with tip radius of tens of nanometers, the elastic contact only within a few nanometers of indentation. Beyond that, the material underneath the tip has been deformed plastically. The maximum indentation depth is hundreds of nanometers, which is well beyond the limit of elastic contact. The plastic strain underneath the tip is not uniform. The plastic strain close to the tip is quite large. Material could have been softened instead of hardened. With a constant indentation force, plastic flow can still happen if the material is weakened. Therefore, the indentation curves have a platform when the applied load reaches the maximum value. It was not found any certain regularity for the hardness between the large and small phases. S1 exhibits the δ strength of 3.12-3.36 GPa and γ strength of 2.53-2.86 GPa. S3 exhibits the δ strength of 2.17-2.75 GPa and γ strength of 3.44-3.74 GPa. It needs a comprehensive and quantitative research for the effect of phase size on the hardness in next step. Since S1 was subjected to a higher annealing temperature, the nano-hardness of δ-phase in S1 may be expected to be lower than that of S3. It is against with the experiment result. It can be explained from the reformation mode of γ-phase. Low annealing temperature favors for grain nucleation, while high temperature favors for grain coarser. The δ-phase of S3 was precipitated by ductile austenite, so it exhibits lower hardness than that of S1. In the macroscopic deformation of two-phase alloys, each phase undergoes elastic and plastic strains under the mutual constraint of the other constituent. The onset of plastic deformation of DSS should occur in the softer phase and is accompanied by severe load redistribution between δ and γ-phases [88, 89]. The strength of the γ of S1 is stronger than that of the δ of S3, So S1 exhibits higher YS than S3 though both of samples exhibit bimodal γ grains and similar microstructure. Some investigations have shown that γ-phase in DSS could be harder [36, 37] than the δ-phase, but the conventional notion about DSS is that the δ-phase is harder [35, 87, 90]. However, S3 renders the converse result that the γ-phase in DSS can also be the reinforcing phase. The strength of γ-phase in S3, if estimated using Tabor's empirical conversion [91] between hardness and strength with ratio 3.5, is about 1 GPa. Taber emprical conversion is to convert between hardness valus and strength. This strength is not the yield strength although Tabor initially tried to correlerate them. The typical conversion parameter is between 3-3.5 accoridng to Tabor's suggestion, though based on his experiments for mild steels, brass etc. Since the γ-phase can be pronouncedly hardened by plastic deformation, the hardness-strength conversion only leads to the flow stress at a large plastic strain. Based on the assumption that the incipient plasticity of S3 is merely due to yielding of δ-phase for that δ-phase is the softer phase in S3, the yield strength of γ-phase in S3 would be about 540 MPa considering the ratio of hardness of two phases (3.54 / 2.44). Comparing to the conventional ASS, such as 304 and 316, which have the yield strength about 200 ~ 300 MPa [92], the γ-phase in S3 is exceptionally strong. The inset of Fig. 5.7 shows the partition coefficient of major alloying elements in δ and γ-phases and the hardness ratio ($HR_{\gamma/\delta}$). The partition coefficient is defined by $K_i = X_i^{\gamma} / X_i^{\delta}$, where $X_i^{\gamma \text{ or } \delta}$ is the weight percent of element *i* in γ or δ-phase, estimated using the energy-dispersive X-ray spectroscopy (EDS). Each data were obtained by comparing δ-phase and its adjacent γ-phase, and 10 different regions were tested to get the average value. No effect was found on the phase size in the partition coefficient. The as-cast sample is also listed as a reference, and its partition coefficients for all alloying elements are nearly equal to 1 due to rapid solidification. The comparison between as-cast sample, S1 and S3 indicates that low-temperature treatment leads to notable increase of nickel and manganese and decrease of aluminum in the γ-phase of S3. S3 is more reasonable as it has a lower Al and higher Mn content in γ-phase, but S1 is strange as it has a higher Al and lower Mn content in γ-phase. It can be explained in the following section 6.2. Both of S1 and S3 did not reach thermal equilibrium state for their phase transformation which is still earlier than composition homogenization period. Therefore, the alloying elements of S1 and S3 are not the steady state. It is known that the deformation mechanism of ASS depends strongly on the stacking fault energy (SFE). With higher SFE, cross-slip is more favored than planar slip [93, 94], leading to the higher yield strength. The empirical equations of SFE [95-99] for ASS all indicate that Ni and Mn are more prominent in increasing SFE than that of Cr. Therefore the γ phase of S3 shall have a higher SFE than that of S1. The SFE of Al-alloyed ASS cannot be found. However, it shall be stressed that solid-solution hardening is not sufficient to explain why the γ-phase in S3 is even harder than the δ-phase of S1. The typical TEM test was conducted to show the grains distribution as shown in Fig. 5.8. Fig. 5.8(a) shows the significantly elongated grains in S1, where the average length of short axis is already about 800 nm. In contrast, Fig. 5.8(b) shows rounded equiaxed grains in S3 with average size of about 750 nm. It was not found any secondary phase in S1, while one σ-phase grain with diameter about 338 nm was found in S3 as shown in the inset of Fig. 5.8(b). However the σ-phase does not induce brittleness for S3 at least in comparison with S1 and S2. The grain size indicated in Fig.

5.8(b) does not distinguish whether they are γ or δ grains. Considering the current DSS casting with 70% δ content, δ-to-γ transformation occurs during annealing concluded in chapter 4. The δ grains, which formed during melt quenching, should be larger than the newly formed γ grains. Therefore, 750 nm can be regarded as the upper bound of the average size of γ grains in S3. In order to confirm the average size of γ grains, TEM images with clear indication of γ/δ grains are shown in Fig. 5.9(a~c), in which both large (microns) and ultrafine γ grains are identified. In addition, the histogram of γ grain size distribution is shown in Fig. 5.9(d), which illustrates the bimodal size distribution of γ grains. The average size of all measured γ grains is still about 750 nm, which is consistent with the measurement made in Fig. 5.8(b). The small grains impart high strength owing to the Hall-Petch effect, and the bi-modal size distribution of γ-phase could be the cause of the largest strain hardening rate and ductility of S3 among the four examined samples [100-102]. The yield strength of γ-phase can be estimated by substituting the average grain size 750 nm into established Hall-Petch relations for DSS [44, 103] and ASS [49, 104-106]. The results are in the range of 559 ~ 738 MPa [18，40-44], among which the minimum magnitude 559 MPa based on [44] agrees admirably with nano-indentation result (540 MPa). Therefore, the ultra-fine grain size of the γ-phase in S3 is concluded to be the main cause of its high strength, and the optimum mechanic property of S3 could be attributed to the bi-modal distribution of γ grain size.

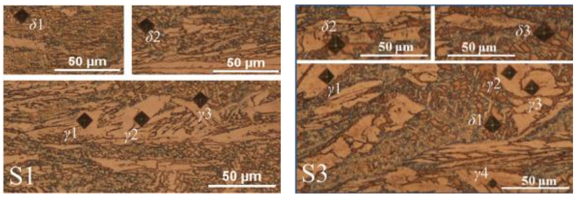

Fig.5.6 Indentation of micro-hardness test on the δ and γ-phases of samples S1 and S3.

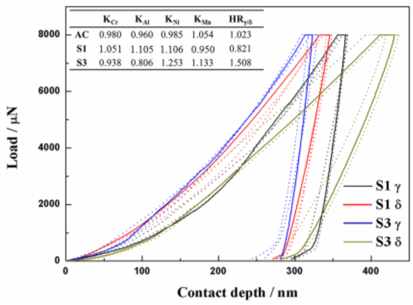

Fig.5.7 Load-indentation results of δ and γ phases in S1 and S3. The inset shows the partition factors of alloy elements and hardness ratios of as-cast sample and S1 and S3.

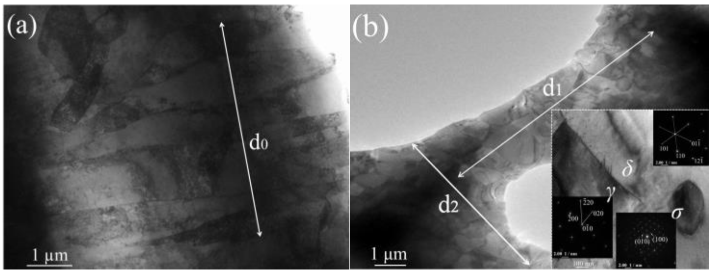

Fig.5.8 Bright-field TEM images showing multiple grains of samples (a) S1 and (b) S3, where segments d_0, d_1, and d_2 are 4.79, 7.89, and 5.45 μm respectively.

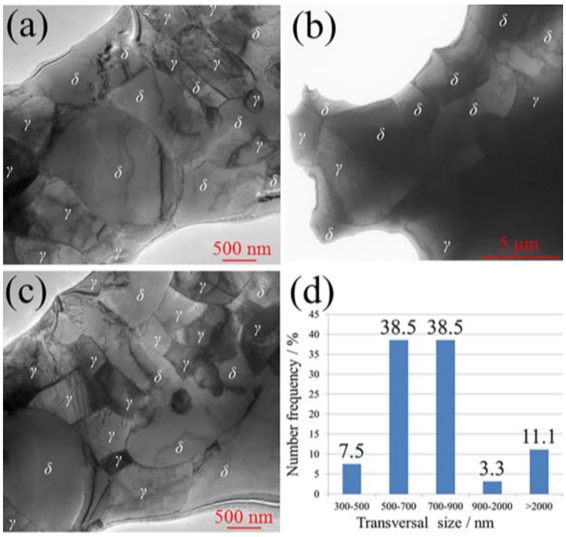

Fig. 5.9 Bright-field TEM images (a), (b), and (c) showing multiple grains of sample S3 with identified γ and δ grains, and (d) distributions of transverse spacing for γ grains.

5.3 Conclusion

This work investigates the DSS 15Cr-2Al-2Ni-11Mn to exhibit that a series of DSS samples with the same phase constituent but different microstructure and mechanical property by employing the non-equilibrium phase transformation of the primary phases. Based on the non-equilibrium kinetics diagram and the effect of cooling method, DSS with about 50% δ-phase was prepared using different non-equilibrium thermal process. It was found that the mechanical performance of DSS is optimised by plastic deformation and low temperature annealing. This solution brings about bimodal size of γ grain, which acts as reinforcing and toughening phase and leads to an excellent combination of strength and ductility of DSS.

Above results also paves the way to further develop 15Cr-2Ni DSS with even larger yield strength and ductility, if the precipitation hardening (through aging [107]) and the transformation induced plasticity (through reducing Mn content [46]) are involved in δ and γ-phases respectively.

Chapter 6 The partition coefficient of alloying elements and its influence on the corrosion resistance of 15Cr-2Ni duplex stainless steel

The segregation behavior of alloying elements in non-equilibrium phase transformation should be useful to indicate and improve the corrosion resistance of duplex stainless steel. The influence of heat treatment parameters including annealing temperature, time and cooling rate on the partition coefficient of alloying elements between δ and γ phases in the as-cast DSS samples was investigated in this chapter

6.1 The effect of annealing temperature

The partition coefficient K_i for element i is defined as $K_i = C_i^\delta / C_i^\gamma$ where C_i^δ and C_i^γ represent the average concentration of element i in the neighboring δ and γ phases respectively. The partition coefficients (K_i) of major alloying elements in the casting ingot are all in the range of 0.95~1.05 as shown in Table 6.1, since the ingot is obtained by fast solidification. Fig. 6.1(a) shows the variations of partition coefficient of DSS samples heated at 750~1150 °C for (I) 30 min and (II) sufficiently long time followed by water quenching, respectively. For case (I), which is a conventional annealing method, K_i deviates away from the uniform line K=1 in 750~950 °C and then approaches K=1 at the temperature higher than 950 °C. For case II, sufficiently long time means that the quenched δ content does not change further with longer annealing time, and DSS samples achieve the isothermal equilibrium state [108]. In this case, K_i approaches the uniform line K=1 monotonically as the annealing temperature increases.

Fig.6.1(b) shows the variations of the volume fraction of δ phase ϕ_δ against annealing temperature T for (I) 30 min and (II) sufficiently long time followed by water quenching, respectively. Through the comparison between Fig.6.1(a) and Fig.6.1(b), it is noted that the variation of the partition coefficient K_i exhibits the same trend as that of the δ content. Atamert and Cortie [109, 110] reported that the element-partitioning between the primary phases becomes more uniform when the solution temperature increases. It should be the case for the casting alloy solidified by air cooling, which the phase transformation in the casting is close to the thermo-equilibrium state. Then the δ content increases with annealing temperature in conventional annealing time of 30 min [9, 111]. Therefore, it can be concluded more exactly that the partition coefficient K_i becomes more uniform when the equilibrium content of δ phase increases.

Table 6.1 Concentrations (wt.%) of major alloying elements in δ and γ phases of casting

Phase	Cr	K	Al	K	Ni	K	Mn	K
δ	15.81	1.02	2.03	1.05	2	1.02	12.73	0.95
γ	15.57		1.94		1.97		13.31	

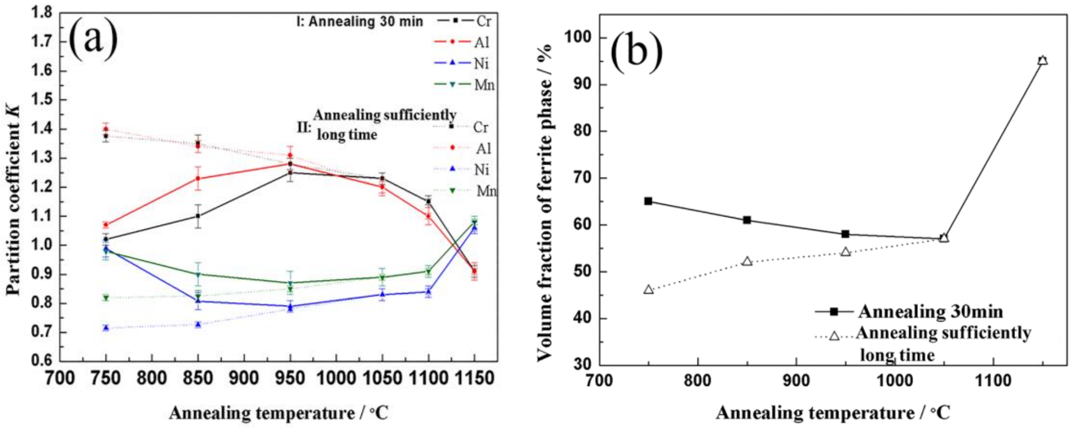

Fig. 6.1(a) Variations of partition coefficient of DSS samples heated at 750~1150 °C for (I) 30 min and (II) sufficiently long time followed by water quenching, respectively. (b)Variations of δ phase volume fractions of DSS samples heated at 750~1150 °C for (I) 30 min and (II) sufficiently long time followed by water quenching, respectively.

6.2 The effect of annealing time

Fig.6.2 shows the experiment result and linear fitting curves on the variation of partition coefficient *K* when samples were heated at (a) 750 °C, (b) 950 °C, and (c) 1000 °C. For the 750 and 950 °C cases, the cooling method is water quenching. For the case of 1000 °C, the cooling method is air cooling. For all these cases, it is noted that the partition coefficients of Cr and Al increase while those of Ni and Mn decrease with the annealing time, finally levels off after 240 min for (a) 750 °C, 70 min for (b) 950 °C and 15 min for (c) 1000 °C. It should be noted that *δ*-to-*γ* phase transformation occurs at temperature below 1050 °C and the durations needed for reaching isothermal phase-equilibrium state at the three temperatures are 240 min for 750 °C, 70 min for 950 °C and 15 min for 1000 °C [108]. This comparison indicates that the period of composition homogenization is reached after the phase transformation is completed, which suggests that the migration of phase boundary may be faster than the diffusion of alloying elements.

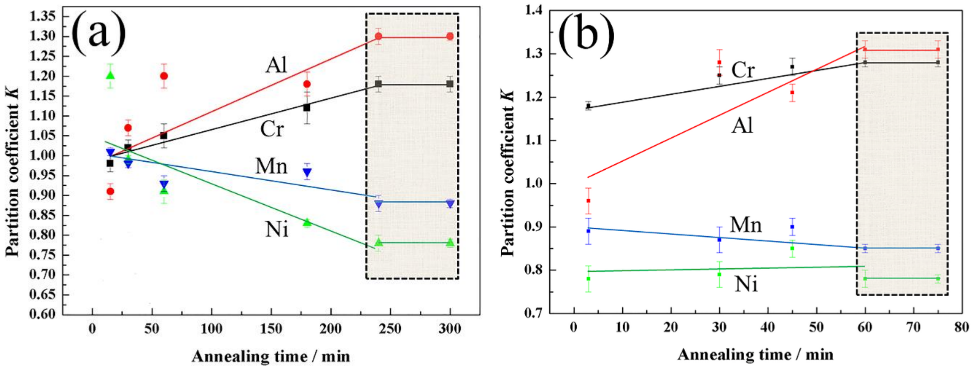

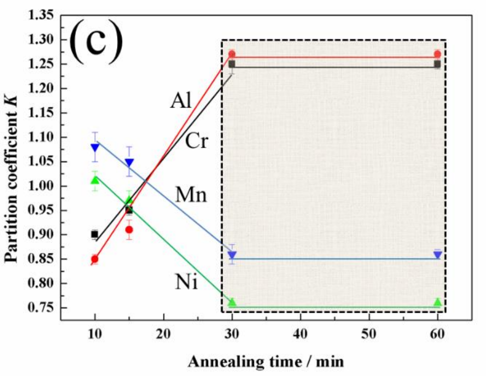

Fig. 6.2 Experiment result and linear fitting curves on the variation of partition coefficient of DSS samples heated at (a) 750 °C for 15~300 min and (b) 950 °C for 3~75 min followed by water quenching respectively, and (c) 1000°C for 10~70 min followed by air cooling. The shaded area refers to the composition homogenization period.

6.3 The effect of cooling rate

Fig.6.3 shows the variation of alloying elements of DSS samples heated at 750~1150 °C for 30 min followed by water quenching, air cooling and furnace cooling, respectively. The partition coefficients of water quenched samples are closer to 1 than that of air cooling and furnace cooling. The comparison between water quenching and furnace cooling was analyzed herein due to the significant difference between them. All DSS alloys solidify ferritically and then transform partially to γ in cooling [1]. Therefore, the δ volume fraction decreases in furnace cooling compared to that of water quenching. As concluded in section 6.1.1, K_i becomes more uniform when the equilibrium content of δ-phase increases. Therefore, the K_i values of Cr and Al after furnace cooling are higher than those of water quenching, while the K_i values of Ni and Mn after furnace cooling are lower than those of water quenching. The magnitude of deviation of the partition coefficient between furnace cooling and water quenching at 1050 ~1150 °C is much larger than that of below 1050 °C as shown in Fig.6.3. It is consistent with the trend of experiment result that δ is much more transformed to γ when the DSS sample is cooled from the temperature higher than 1050 °C than that of below 1050 °C as shown in Fig.6.4.

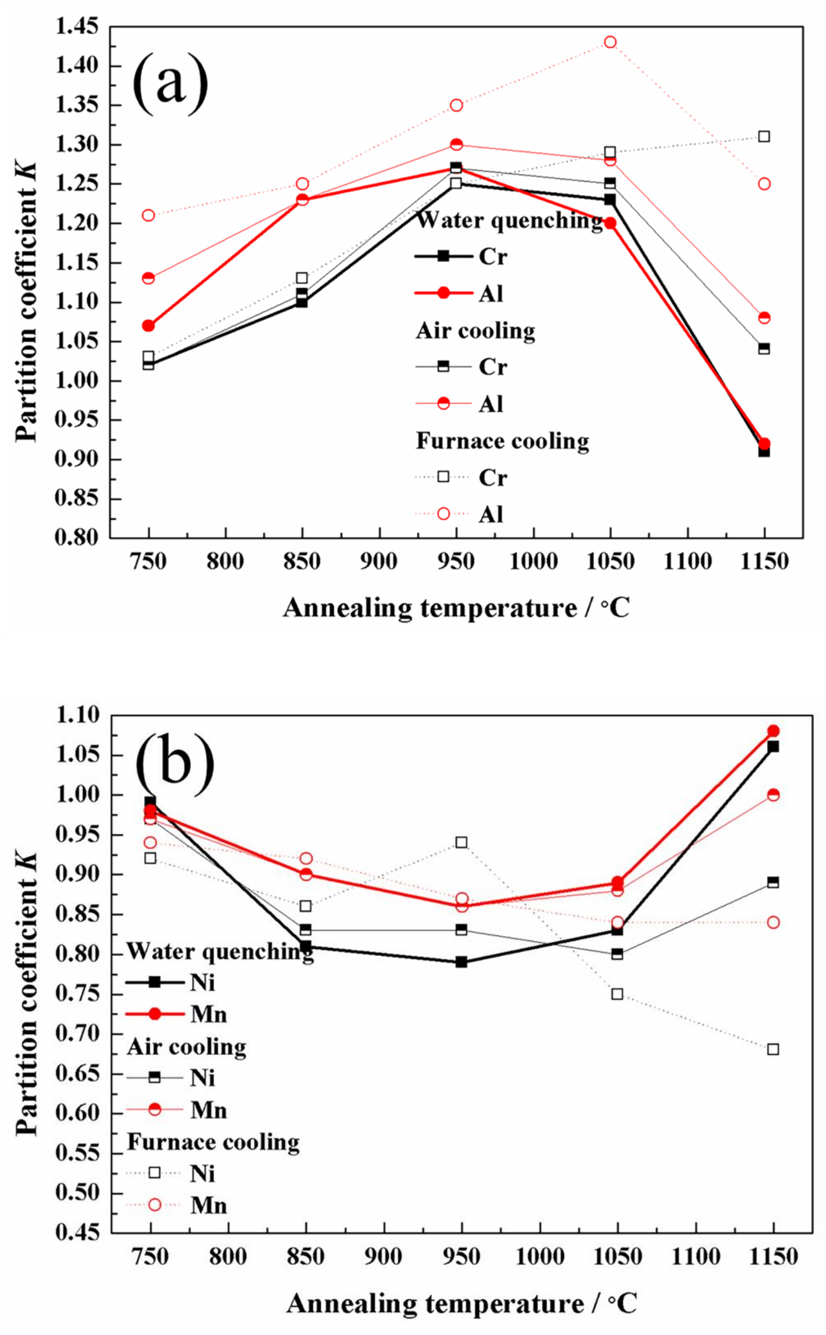

Fig. 6.3 Variations of partition coefficient of alloying elements (a) Cr and Al (b) Ni and Mn when DSS samples heated at 750~1150 °C for 30 min followed by water quenching, air cooling and furnace cooling, respectively.

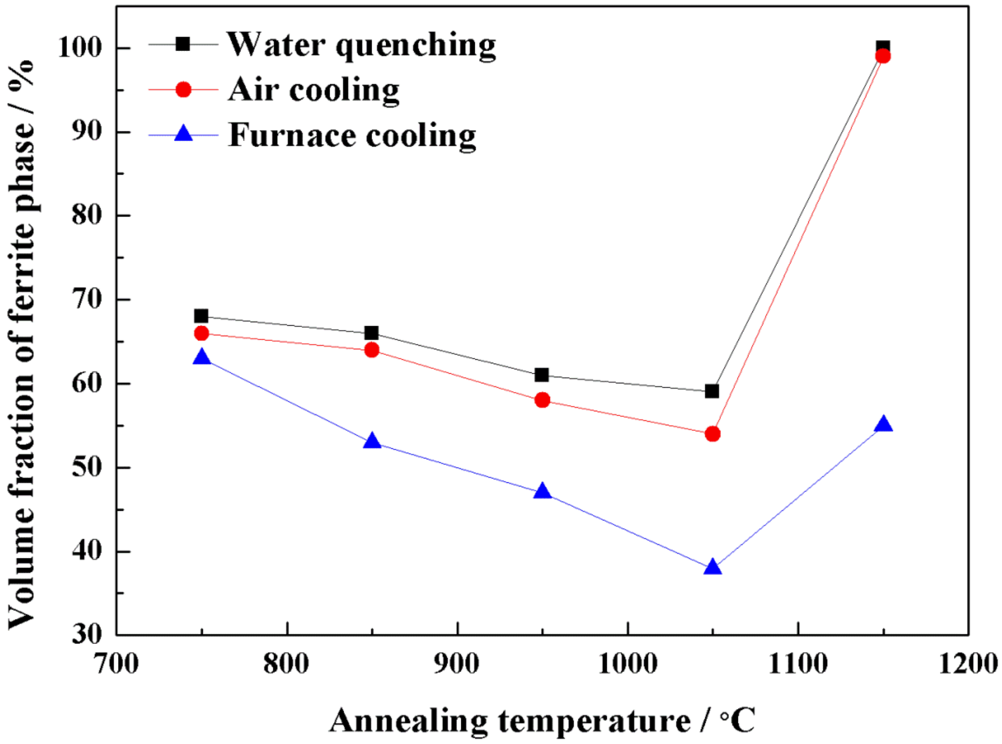

Fig. 6.4 Variations of δ phase of DSS samples heated at 750~1150 °C for 30 min followed by water quenching, air cooling and furnace cooling, respectively.

6.4 Improve the corrosion resistance

Polarization test was carried out to investigate the corrosion resistance of DSS samples. Pitting resistance equivalent number (PREN) is widely used to predict the pitting corrosion resistance and correlates with the chemical composition of stainless steels. Higher PREN is generally in accord with better pitting corrosion resistance in most stainless steels. For the resource-saving DSS, PREN is redefined for considering both the beneficial promotion of Al [112] and the detrimental influence of Mn [9, 113] on the pitting corrosion resistance as follows:

$$\text{PREN} = \text{wt.\% Cr} + 2.5\ \text{wt.\% Al} - 0.75\ \text{wt.\% Mn} + 3.3\ \text{wt.\% Mo} \qquad (6.1)$$

Five DSS samples were chosen to examine the proposed PREN of γ and δ-phases. The DSS samples are coded as (1#) 1000-30-a, (2#) 1000-15-a, (3#) 750-30-w, (4#) 750-

15-w and (5#) 1150-15-a, which indicate the DSS samples heated at 1000 °C for 30 min followed by air cooling, 1000 °C for 15 min followed by air cooling, 750 °C for 30 min followed by water quenching, 750 °C for 15 min followed by water quenching, 1150 °C for 15 min followed by air cooling, respectively. Fig.6.5 shows the representative polarization curves of 1~5# DSS samples in 3.5 wt.% NaCl aqueous solution at 25 °C, and the pitting potential values are 5# > 3# > 1# > 2# ~ 4# as listed in the Table 6.2. According to the specific chemical composition of δ and γ phases, the ratios of PREN value ($R_{\delta/\gamma}$) of the five samples are 14.40/8.10, 10.48/12.35, 12.53/11.77, 10.53/11.31, 13.72/10.77, respectively. The corrosion resistance of 1#, 3# and 5# should be dependent on the corrosion resistance of γ, while that for 2# and 4# is on δ. So the theoretical sequence of the corrosion resistance of DSS samples is 3# > 5# > 4# ~ 2# > 1#, which is not consistent with that of the experiment result listed in Table 6.2. The corrosion resistance of DSS is partially affected by the microstructure, particularly the contact area between the δ and γ-phases [113]. DSS samples 1# and 2# have the same volume fraction of δ-phase [108], but the grain size of 1# is larger than that of 2# due to longer annealing time. The contact area between the δ and γ phases of 1# is less than that of 2#, and it can be the cause that the pitting potential value of 1# is higher than that of 2#. DSS sample 5# has nearly 90% content of δ-phase, and the small contact area between the δ and γ-phases can promote the pitting potential value of 5#.

However, the microstructure factor is not the case in research on the contrast of corrosion resistance between δ and γ-phases within the same sample, and these contrasts of corrosion resistance of two phases calculated by PREN equation using chemical composition are consistent with the result of the pitting corrosion test. The metallographs of the specimens after polarization test are shown in Fig. 6.6. It can be seen that the phase which was etched first for 1#, 3# and 5# is γ while that for 2# and 4# is δ.

The effect of annealing time on the contrast of corrosion resistance between δ and γ-phases is exhibited based on the comparison of samples 1# vs 2# and 3# vs 4#. Fig. 7.2 indicates that longer annealing time increases the concentration of Cr and Al and reduces the concentration of Mn in the δ-phase at annealing temperature 750 and 1000 °C. Therefore, the $R_{\delta/\gamma}$ value of 1# is higher than that of 2#, and that of 3# is higher than that of 4#. It can be concluded that the longer annealing time, at the temperature inducing δ-to-γ transformation, leads to the increase of Cr and Al and decrease of Mn in δ-phase, which improves the corrosion resistance of δ-phase.

High annealing temperature also exhibits impressive impact on the contrast of corrosion resistance between δ and γ-phases of DSS samples as exhibited on the comparison of samples 2# and 5#. The corrosion test of 5# shows that the pitting occurred in γ-phase. It reverses the result compared to that of 2#. The γ-to-δ phase transformation occurs at 1150 °C, which can be concluded from Fig.6.1(b) [108]. It leads to even lower content of Cr at 1150 °C compared to that of 1000 °C in the γ-phase of DSS sample. Therefore, the γ-phase becomes the weaker phase in pitting corrosion resistance than that of δ-phase in DSS sample 5#.

Table 6.2 The pitting corrosion potential values of DSS samples 1# ~ 5#

DSS samples	1#	2#	3#	4#	5#
Pitting corrosion potential (mv)	-38	-120	25	-120	200

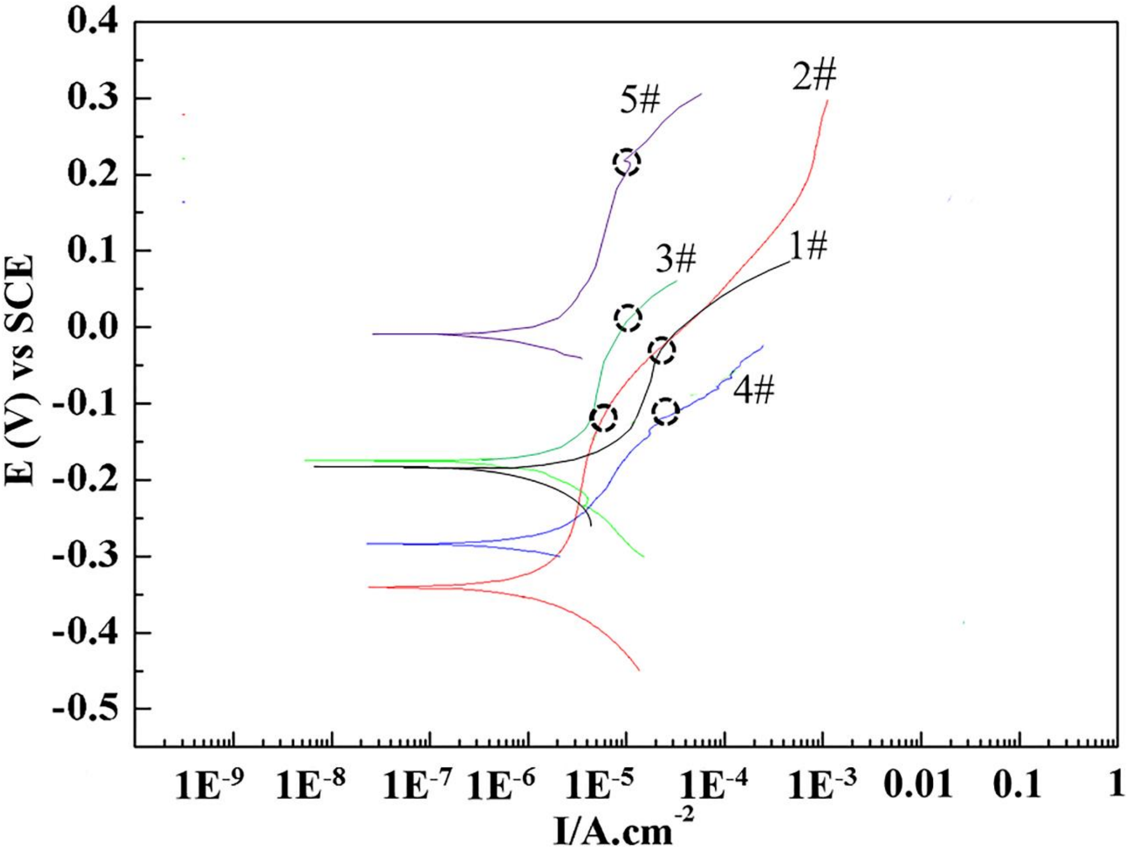

Fig.6.5 The representative polarization curves of DSS samples 1~5# in 3.5 wt.% NaCl aqueous solution at 25 °C

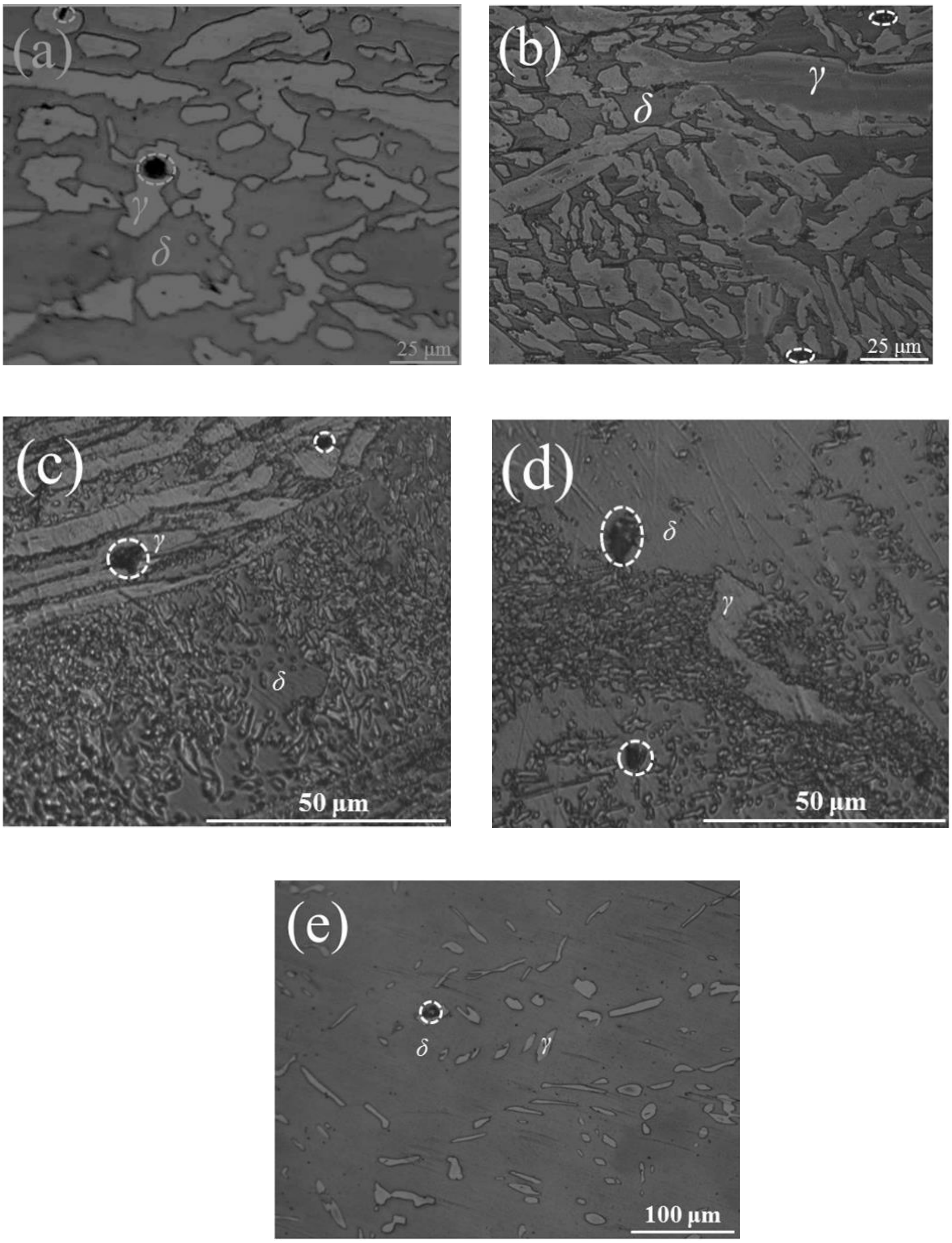

Fig.6.6 Metallographs of DSS samples heated at 1000 °C for (a) 1#-30 min and (b) 2#-15 min followed by air cooling, 750 °C for (c) 3#-30 min and (d) 4#-15 min followed by water quenching, and (e) 5#-1150 °C for 15 min followed by air cooling after polarization test.

6.5 Application on making the porous materials

The above investigation indicates that even with the same chemical composition of

DSS samples, different heat treatments can bring about distinct contrast of the corrosion resistance between γ and δ-phases. One possible application is then to produce porous stainless steel by etching off a primary phase. Porous stainless steel may be used in high-tech filter membrane and filtration of fluids with advantages of good electric conductivity, good corrosion resistance and readjustable on the porous. To demonstrate the possibility, uniform corrosion test was carried out with the DSS sample heated at 1100 °C for 30 min followed by furnace cooling. This DSS sample has approximately 50/50 γ and δ-phases, nearly equiaxed phase morphology as shown in Fig.6.7 (a), and $R_{\delta/\gamma}$ =1.43. Fig.6.7 (b) shows the metallograph of DSS sample after uniform corrosion test for 48 h, and the γ phase was apparently first etched off. With the corrosion testing time increased to 120 h as shown in Fig.6.7 (c), the etched phase areas rapidly increase, and most of those occurs in γ-phase. Therefore, the result that all γ or δ-phase can be etched and only the other one phase kept is possible as long as that the $R_{\delta/\gamma}$ value deviates significantly from 1. As summarised from above, the annealing time and temperature can be effectively used to achieve the result and obtain the porous materials.

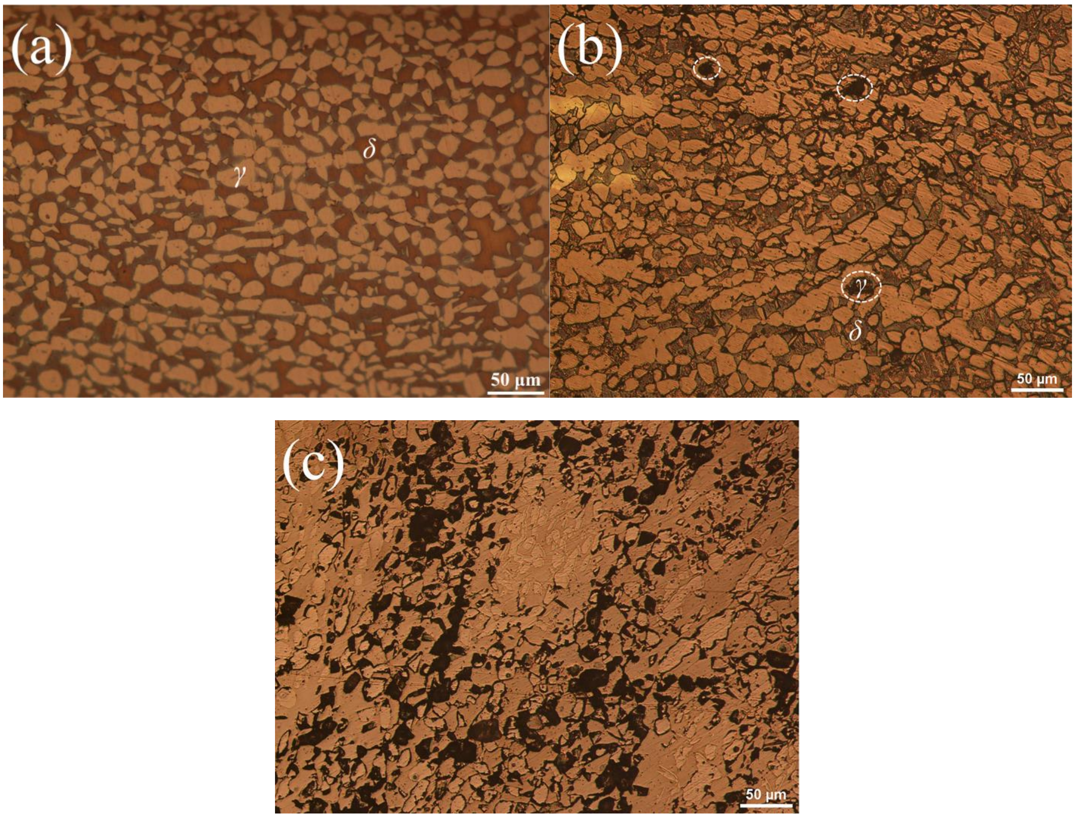

Fig.6.7 Metallograph of DSS samples heated at 1100 °C for 30 min followed by furnace cooling (a) and its metallographs after uniform corrosion test for (b) 48 h (c) 120 h at 25 °C.

6.6 Conclusion

The influence of heat treatment parameters including annealing temperature, time and cooling rate on the partition coefficient of alloying elements between δ and γ-phases was investigated and found to be useful to vary the corrosion resistance comparison between δ and γ-phases of DSS. The main findings are:

1. The annealing temperature and cooling rate affect the partition coefficient of alloying elements, which can be correlated to the variation of δ phase volume fraction. When the δ phase volume fraction increases, the partition coefficient becomes more uniform and close to 1.
2. With the annealing time increases, the partition coefficients of Cr and Al increase

while those of Ni and Mn decrease, finally levels off after the DSS sample reaching isothermal phase-equilibrium state.

3. No any dependent effect of the partition coefficient of alloying elements between *δ* and *γ* phases on the overall corrosion resistance of DSS was found. The microstructure, particularly the contact area between the *δ* and *γ* phases exhibits impact on the overall corrosion resistance of DSS.
4. The contrast of corrosion resistance between *δ* and *γ* phases varies owing to the change of the partition coefficients of alloying elements. Longer annealing time is beneficial for improving the corrosion resistance of *δ* phase if the annealing temperature leads to *δ*-to-*γ* phase transformation in DSS. Higher annealing temperature, at which *γ*-to-*δ* phase transformation occurs in DSS samples, can rapidly increase the corrosion resistance of *δ*-phase.
5. This work also suggests the way to develop single-phase porous stainless steel through etching by controlling the heat treatment condition to achieve strong contrast of corrosion resistance between *δ* and *γ* phases.

Chapter 7 The kinetics diagram of sigma phase and its precipitation hardening effect on 15Cr-2Ni duplex stainless steel

The growing kinetics of σ-phase and its precipitation hardening effect on DSS alloy were investigated in this chapter.

7.1 The microstructure of σ phase

Fig.7.1 shows the DSS samples aging at 750 ºC for 300, 1050 min, 850 ºC for 180, 320 min and 900 ºC for 45 min and 90 min, respectively. σ-phase was found in γ-phase. No σ-phase was found in the sample aging at 950 ºC. Fig. 7.2 shows the scanning electron micrograph of the DSS sample aging at 750 ºC for 1050 min, and the chemical composition of σ, δ and γ is listed in Table 7.1. The chemical composition of σ-phase is more close to that of γ-phase than that of δ-phase. The microstructural features have been studied by TEM as shown in Fig. 7.3. The size and amount of σ-phase increase continuously with aging time. Also, the size and amount of σ-phase aging at 850 ºC are bigger than those of 750 ºC. With different aging temperature, the morphology of the σ-phase changes as shown in Fig. 7.1. At 750 °C, a coral-like structure of σ-phase forms, while that of 900 °C is bulk-like σ-phase. At 750 °C, the amount of single σ nuclei at the beginning of the precipitation is rather high, and lower diffusion velocity causes higher local supersaturation and leads to a higher density of precipitations. A different precipitation behavior can be observed at 900 °C. The σ-phase is bigger and the linking between single σ-phase crystals is marginal, due to the low nucleation formation force but a high diffusion rate.

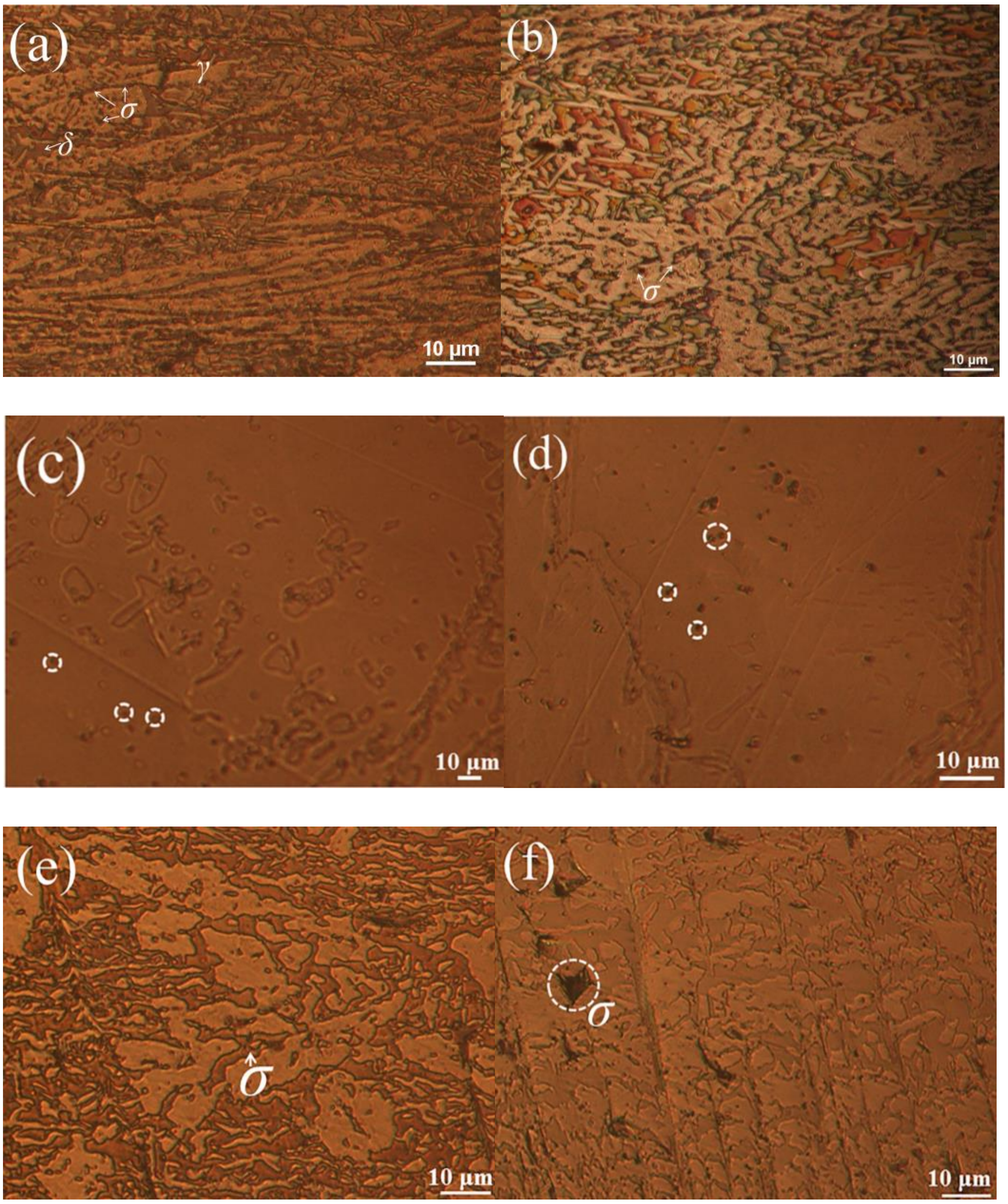

Fig. 7.1 DSS samples aging at 750 ºC for (a)300 min (b) 1050 min, 850 ºC for (c) 180 min (d) 320 min and 900 ºC for (e) 45 min (f) 90 min followed by water quenching, respectively.

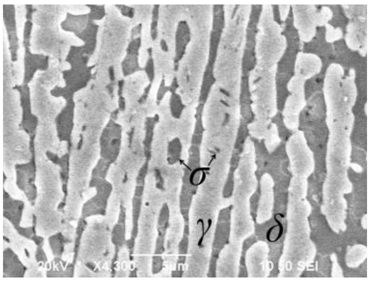

Fig. 7.2 Scanning electron micrographs on the DSS sample aging at 750 ºC for 1050 min.

Table 7.1 The chemical composition of σ, δ and γ phases of DSS sample aging at 750 ℃ for 1050 min (wt.%)

	Cr	Al	Mn	Ni	Fe
δ	17.4	1	12.24	1.78	Bal.
γ	14.03	1.87	13.28	2.18	Bal.
σ	14.07	1.20	14.11	0	Bal.

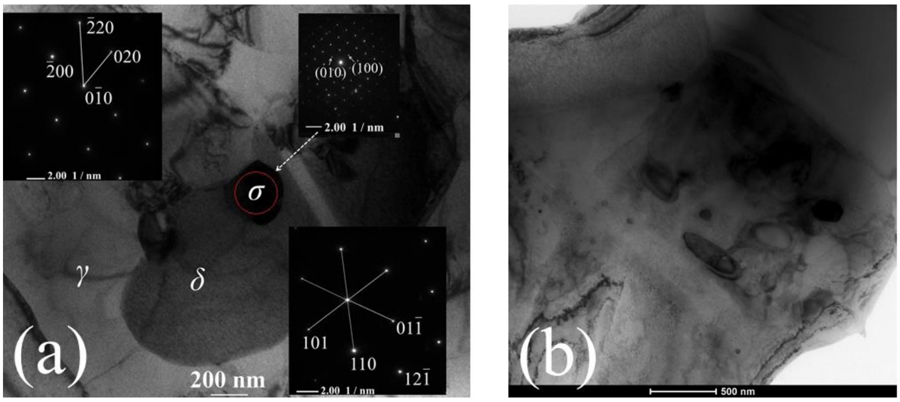

Fig.7.3 The typical TEM images taken from δ/γ interface of DSS sample aging at (a) 750 ºC for 90 min and (b) 850 ºC for 235 min.

7.2 The σ phase precipitation kinetics in DSS

The kinetic of σ-phase formation in stainless steel has been reported [58] on elucidating the transformation characteristics. Various physical parameters can affect the transformation kinetic, and these parameters include minor variations in the chemical composition, phase grain size and its volume fraction, as well as the thermal and/or mechanical pre-treatment used, in addition to the direct effect of aging time and temperature. Therefore, it is hard to predict accurately the σ-phase transformation kinetics using one universal model. The Johnson–Mehl–Avrami relationship is one of the most commonly used theories to describe transformation kinetics in many systems involving nucleation and growth.

$$f = \phi \ / \phi^{e} = 1 - \exp(-kt^{n}) \tag{7.1}$$

Where f is the fraction transformed, ϕ^{e} is the volume fraction of σ-phase at the equilibrium state, ϕ is the volume fraction of σ-phase at time t, k and n are fitting parameters. The magnitudes of fitting parameters n, τ, t_0, ϕ^{e} are listed in Table 7.2. It is noted that n ≈ 2.5 is consistent with the kinetics of σ-phase precipitation in [58], which indicates σ-phase formation is diffusion controlled. Fig. 7.4 shows the experimental results and fitting curves on the temperature-time dependent variation of σ content, which exhibits the non-equilibrium kinetics and the equilibrium state of the σ-phase precipitation in 15Cr-2Al-2Ni-11Mn alloy. It shows the formation of σ-phase was fastest at 850 ºC while slowest at 750 ºC.

The Avrami equations were then used to establish TTT diagrams for f = 1%, 50% and 99% σ phase formation, as shown in Fig. 7.5. Usually, the time needed for f = 1% is defined as the breeding time, while f = 99% as completed. The nose of the initial curve is located at temperature 850 ºC for about 350 min. Fig. 7.3 (a) shows the typical TEM graph taken from DSS samples aging at 750 ºC for 90 min which exhibits a σ phase grain with size of approximately 200 nm. It identifies the application of the fitting diagram in short aging time when the σ phase can not be seen in optical microscope. Fig. 7.3 (b) shows the typical TEM graph taken from DSS samples aging at 850 ºC for 235 min which exhibits σ phase grains with size between 50~550 nm.

Table 7.2 Fitting parameters of Avrami equation for DSS samples aging at 750, 850 and 900 ºC

DSS	*k*	*n*	ϕ_e (%)
750	4.98E-7	2.24	9.5
850	7.46E-7	2.33	11.5
900	3.08E-7	2.44	10.5

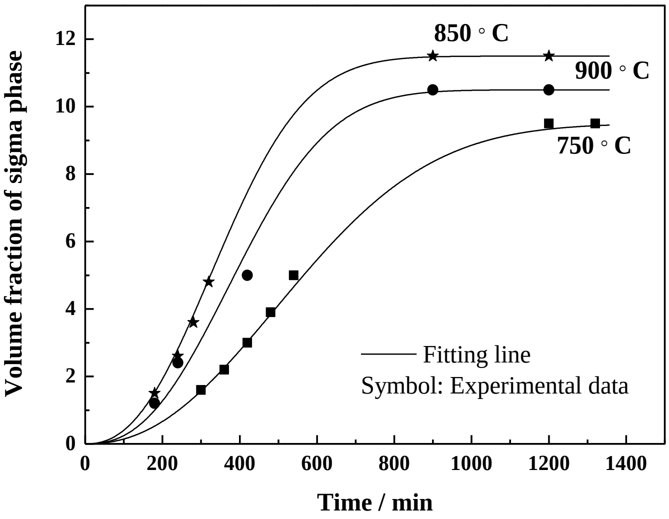

Fig. 7.4 Aging data and fitting curves of DSS sample on the temperature-time dependent variation of σ-phase content

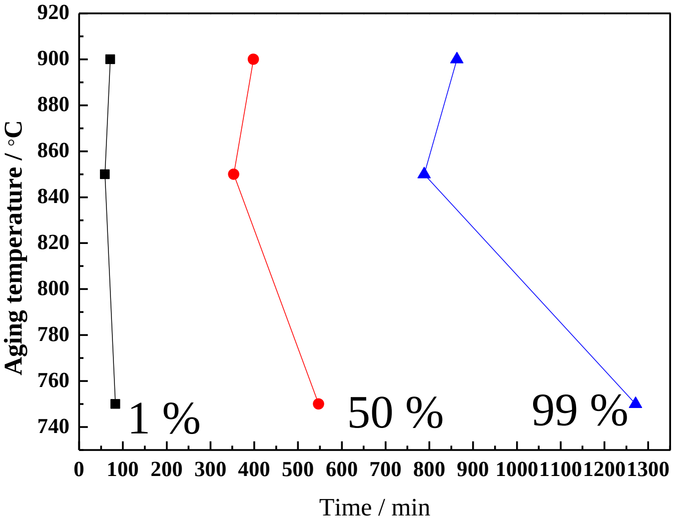

Fig. 7.5 Calculated TTT diagram on σ-phase volume fraction transformed f

7.3 The effect of Mo on the precipitation of σ-phase

In order to investigate the alloying element of Mo on the precipitation behavior of σ-phase, 15Cr-2Al-2Ni-7Mn-0.5Cu-0.5Mo and 15Cr-2Al-2Ni-7Mn-0.5Cu-Mo were added to compare with the performance of 15Cr-2Al-2Ni-11Mn. These three DSS were referred as Mo-0, Mo-0.5 and Mo-1 in this section, respectively. Fig. 7.6 shows the metallographs of DSS samples aging at 850 ºC for 780 min, and it can be found that the size and mass amount of σ-phase increases with Mo content. σ-phase was formed in δ-phase for Mo-0.5 and Mo-1. The magnitudes of fitting parameters n, τ, t_0, ϕ^e are listed in Table 7.3. Fig. 7.7 shows the experimental results and fitting curves of Mo-0, Mo-0.5 and Mo-1 on the time dependent variation of σ-phase content at 850 ºC. It is noted that both the precipitation rate and the mass amount of σ-phase increase with Mo content in DSS samples.

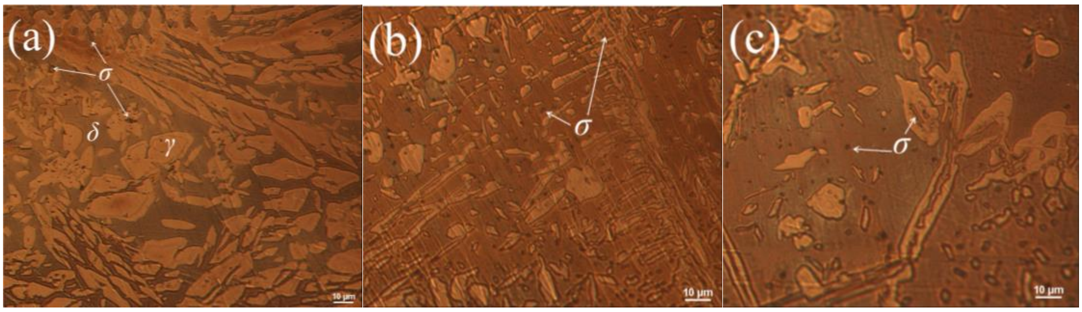

Fig. 7.6 Metallographs of DSS aging at 850 ºC for 780 min (a) Mo-0 (b) Mo-0.5 (c) Mo-1

Table 7.3 Fitting parameters of Avrami equation for Mo-0,0.5,1 aging at 850 ºC

DSS	k	n	ϕ_e (%)
Mo-0	7.47E-7	2.33	11.5
Mo-0.5	7.82E-8	2.65	17.0
Mo-1	1.93E-6	2.05	21.0

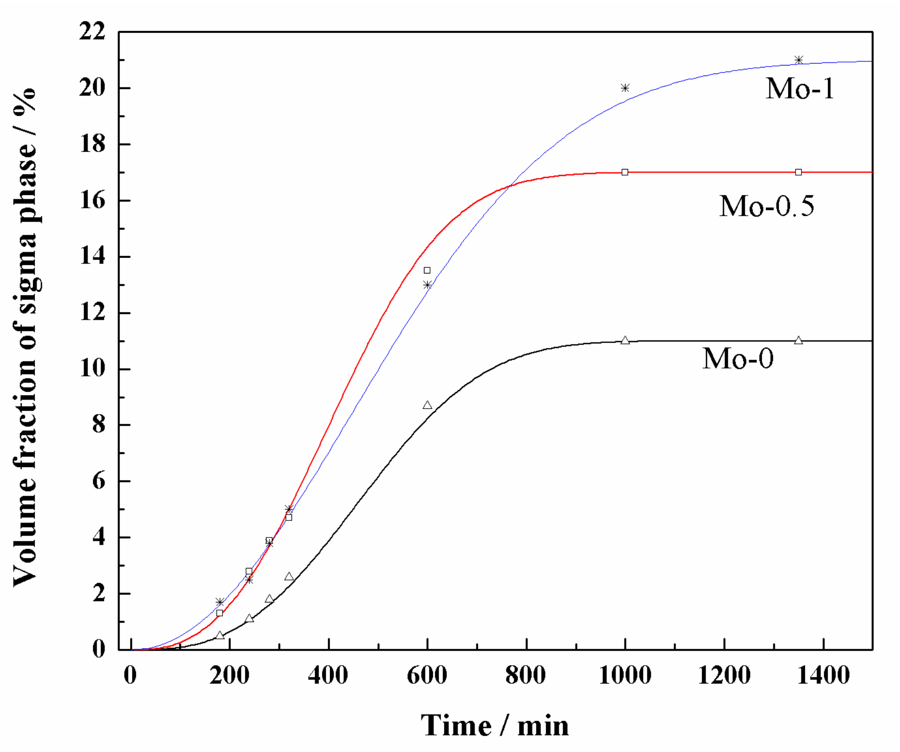

Fig. 7.7 Aging data and fitting curves of Mo-0, Mo-0.5 and Mo-1 on the time dependent variation of σ phase content at 850 ºC.

7.4 Mechanical property of duplex stainless steel

Tensile test was conducted on the DSS samples aging at 850 ºC for different time to investigate the effect of σ-phase precipitation on the mechanical performance. Fig.7.8 shows the tensile curves of DSS samples aging at 850 ºC for 105, 140, 160, 180,195, 210, 235 min, respectively. It shows that sample-105 min exhibits normal mechanical performance with yield strength about 350 MPa and elongation 28%. With the aging time increases, the strength increases while elongation decreases. The strength reaches a peak of about 900 MPa at 180 min aging with the worst elongation no more than 5%. After 180 min, the strength decreases while elongation increases with increased aging time. The volume fraction of γ-phase increases with the aging time, and reaches an equilibrium state of about 50% at 180 min as investigated in Chapter 4. Therefore, the volume fraction of γ-phase of 180, 195, 210 and 235 samples is nearly the same, but the grain size increases with aging time. In the range of 105, 140, 160 and 180 min aging, the strength should decrease while elongation increase due to the increase of γ-phase; Meanwhile, the σ-phase content increase from 0.5% to 0.8%, 1.2% and 1.5%, and it makes experiment result reverse with last judge. Then, in the range of 180, 195, 210 and 235 min aging time, the strength should decrease while elongation increases due to the increased grain size; Meanwhile, the σ-phase content increase from 1.5% to 1.8%, 2.1% and 2.6%, and its impact on the mechanical performance is reduced according to the experiment result. The increase of strength from sample-105 to sample-180 is attributed to the formation of σ-phase. σ-phase precipitation prevents the dislocation movement so the strength of sample increases. With the aging time longer than 180 min, the increase rate of the amount of σ-phase decreases, but that of the size of σ-phase increases. The coarsened σ-phase precipitation does not inhibit sufficiently to the mobile dislocations, leading to the decreased strength and increased elongation of DSS sample-195 and after. This is the over aging mechanism [114]. Fig. 7.9 shows the typical morphology on the fracture surface of DSS samples aging at 850 ºC for 105, 180 and 235 min after tensile test at room temperature. The morphology of samples-105 and 235 min show most ductile fracture feature, composed of fine and big ductile dimples which contributed to the ductility. However, sample-180 min shows most brittle fracture feature, and σ-phase precipitation was identified at the fracture surface with the chemical composition as listed at Table 7.4. Apparently, σ-phase plays the role of crack source in Sample-180 min.

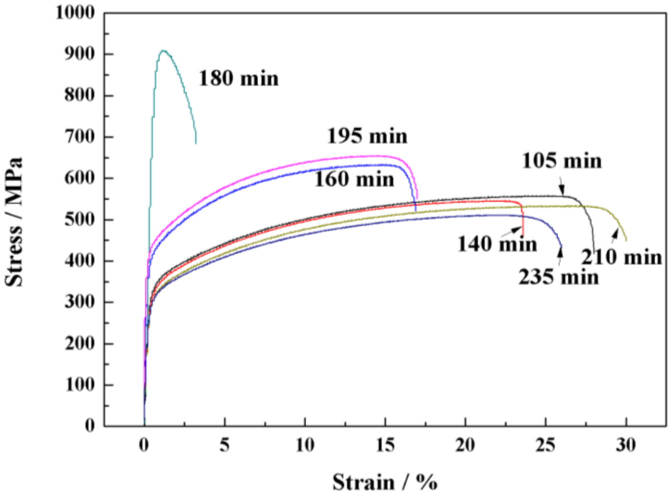

Fig. 7.8 Tensile curves for DSS samples annealing at 850 ºC

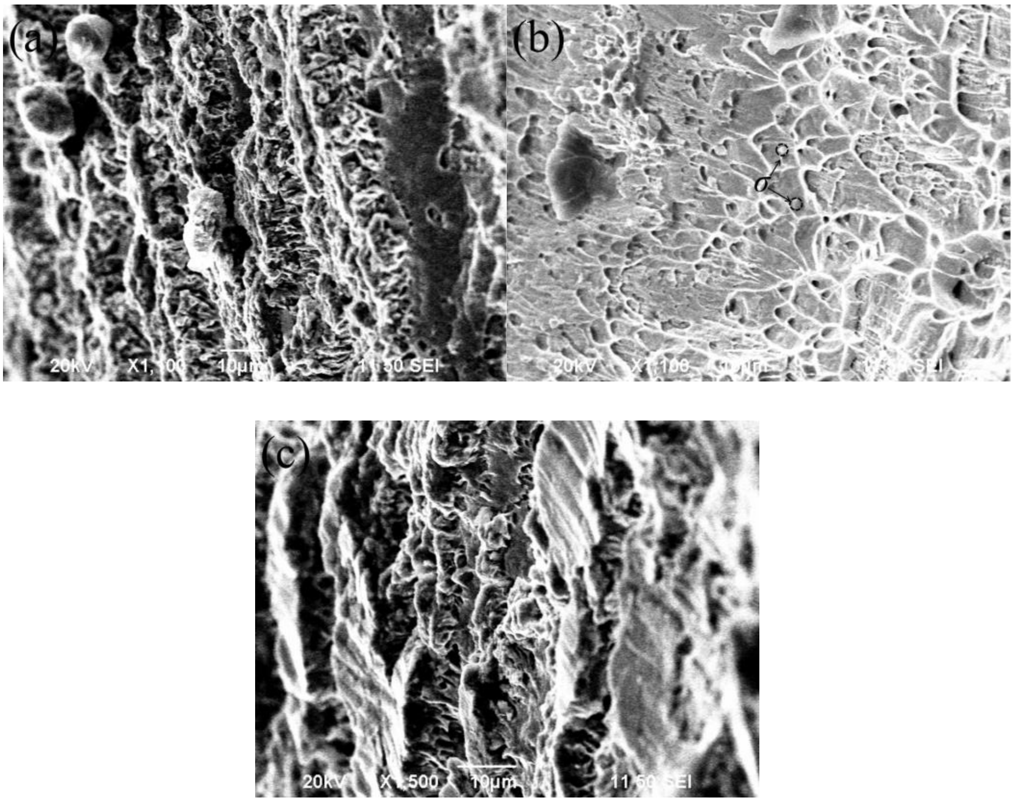

Fig. 7.9 The typical morphology on the fracture surface of DSS samples aging at 850 ºC for (a) 105, (b)180 and (c) 235 min.

Table 7.4 The chemical composition of σ phase of DSS sample aging at 850 ℃ for 180 min (wt.%)

Cr	Al	Mn	Ni	Fe
14.11	7.37	9.12	0	Bal.

7.5 Conclusion

The growing kinetics of σ-phase and its precipitation hardening effect on DSS alloy were investigated and the main findings are as follows:

1. Upon aging at 750~900 ºC, the σ-phase precipitates in the DSS, and the size and amount of σ-phase increase continuously with aging time.

2. TTT diagram of σ-phase precipitation is established, and the kinetics of σ-phase formation reaches peak at about 850 ºC aging.

3. Mo increases the formation rate and the mass amount of σ-phase, and favorites σ-phase precipitated in δ-phase.

4. The σ-phase most increase the strength and decrease the elongation when its volume fraction is 1.5%.

Chapter 8 Theoretical models for phase transformation in duplex stainless steel

8.1 Conventional model

The phase transformation between *δ*/*γ* phases is widely considered to be controlled by elemental diffusions. And in a rapid heating and cooling process, such as welding, it can be regarded that the substitutional elements cannot redistribute within the two phases because of insufficient time caused by rapid cooling. Therefore, the diffusion of interstitials elements, such as nitrogen in super DSS, was considered to be the main cause of phase transformation. Hertzman *et al*. [27] then established a theoretical model of phase growth based on nitrogen diffusion. Hemmer *et al*. [115] proposed another theoretical model by ignoring nitrogen diffusion in the *δ* phase. Zhang *et al.* then established the one-dimensional phase field model to study the phase transformation in DSS [28].

8.2 Phase field model for phase transformation of DSS

Phase transformation is generally coupled with different physical processes, such as diffusion, interface migration, morphology evolution, thermal conduction and mechanical deformation, etc. These processes are intertwined, giving rise to great difficulty in determining their respective influence through merely experimental studies. Phase-field approach was thus proposed [116] and become the powerful tool for quantitative analysis of phase evolution in materials.

The γ-to-δ phase transformation in DSS mediated by nitrogen diffusion [28] can also be described by phase-field model. Let φ be the phase order parameter, which is 1 for δ phase and 0 for γ phase and c be the concentration of nitrogen. Based on the Ginzburg-Landau formulation and the diffusion-interface approach, the total Gibbs free energy of the material is established as follows:

$$G = \int_{\Omega} [g(\phi, c, T) + \varepsilon |\nabla \phi|^2 / 2] dV \tag{8.1}$$

where G is the total Gibbs free energy in the closed system Ω and g represents the Gibbs free energy density, dependent not only on the order parameter ϕ but also on the concentrations c and temperature T. The interfacial energy is given as $\varepsilon |\nabla \phi|^2 / 2$, where ∇ indicates gradient and ε is the scale factor of the interfacial energy density. Given the interfacial energy density σ (per unit area) and interface thickness λ, it can be found that $\varepsilon=\sigma\lambda$.

Following Kim et al. [117], the Gibbs free energy density g is defined to be the summation of the weighted average of diffusion potentials in δ and γ and a double-well potential as follows:

$$g(\phi, c, T) = p(\phi) g_{\delta}(c, T) + [1 - p(\phi)] g_{\gamma}(c, T) + q(\phi) W \tag{8.2}$$

g_δ and g_γ are the homogeneous diffusion potential density in δ and γ phases, respectively. They are assumed in quadratic form as shown in Fig. 8.1(a), after Echebarria et al. [17], given as:

$$g_{\delta(or\gamma)} = 0.5 A^0_{\delta(or\gamma)} (c - c^0_{\delta(or\gamma)})^2 + B^0_{\delta(or\gamma)} \tag{8.3}$$

where $A^0_{\delta(or\gamma)}$ is the curvature of energy density function ($A^0_\delta = A^0_\gamma = A^0$ is assumed for simplicity), $B^0_{\delta(or\gamma)}$ denotes the height of energy density, and $c^0_{\delta(or\gamma)}$ represents the equilibrium concentration of nitrogen corresponding to the minimization of free energy density. The double-well potential $q(\phi)W$ is used to describe the activation energy barrier between the neighboring phases during transformation in DSS. W is the height of energy barrier and can be related to the interfacial energy and thickness in the form of W=18σ/λ. $q(\phi)$ is the double-well function with minimum at ϕ=1 and ϕ=0, and symmetric about ϕ=0.5, given in the form of $q(\phi)=\phi^2(1-\phi)^2$.

Based on the principle of free energy minimization, the governing equations for the interface migration and elemental diffusion can be given as:

$$\partial\phi/\partial t = -M_\phi\left(\delta G/\delta\phi\right) = M_\phi\left[\varepsilon\nabla^2\phi - \partial g\left(\phi,c,T\right)/\partial\phi\right], \tag{8.4}$$

$$\partial c/\partial t = \nabla D\nabla c + \nabla\frac{D}{\partial^2 g/\partial c^2}\frac{\partial^2 g}{\partial c\partial\phi}\nabla\phi. \tag{8.5}$$

These partial differential equations can be solved by finite element method after developing a user element subroutine in the commercial finite element package ABAQUS [118]. In order to compare with previous studies, we study the welding case reported in [28]. The parameters are listed in Table 8.1, which are taken from [28] for calibrating our model. In Fig. 8.1(a), the TTT diagram is obtained. The relation between time and temperature for given δ phase volume fraction (55%, 65%, 75%, 85%, 99%) are plotted based on simulation results and the equilibrium fraction of δ phase at different temperature is obtained. By comparing the equilibrium volume fraction at given temperature with the theoretical results from [28], A_0 and ΔB_0 are determined and listed in Table 8.1. The parameterized model is then applied to simulate the γ-to-δ transformation in heat affected zone during welding, which has been experimental studied in [28]. Considering the linear temperature rise from 1338K to 1658K within 4s and using the initial condition given, the evolution of δ phase during heating, based on the 1-D model, is plotted in Fig. 8.1(b). It is noted that the numerical results from present model agrees with those from Zhang's model as well as the experimental results [28]. Although the predicted competition time of γ-to-δ transformation based on the present model is different from that of Zhang's model, it matches well with the experimental data. In the TTT diagram (Fig.8.1(a)), the discrepancy on the completion time of phase transition between our model and the model of Zhang *et al.*, namely the 99% curve, is also shown. This discrepancy is thought to be caused by the different description of the interface. In our model, the nitrogen concentration of the interface is finite, which must satisfy the conservation law and become more realistic. However, in Zhang *et al.*'s work, the concentration in interface is unbounded.

While the γ-to-δ phase transformation in DSS is considered to be primarily mediated by the substance diffusion, the diffusion coefficients at different temperatures are difficult to determine and often varies in a wide range. The Arrhenius relation between diffusion coefficient and temperature is assumed, given in Table 8.1.

Table 8.1 Parameters in present phase field model

Parameters	Value
Nitrogen diffusion coefficient in δ [27]	$D_\delta = 0.464\times 10^{-6}\exp(-10223.7/T)$
Nitrogen diffusion coefficient in γ [119]	$D_\gamma = 36\times 10^{-6}\exp(-18883.8/T)$
Equilibrium nitrogen concentration (wt%) [28]	$c_\delta^0 = 10^{0.002703T-5.04964}$ $c_\gamma^0 = 0.255+10^{0.002257T-3.99984}$
Initial volume fraction	54% δ-phase 46% γ-phase
Initial nitrogen concentration [28]	0.03% in δ-phase 0.356% in γ-phase
Initial thickness [28]	δ-phase =11.1 um γ-phase = 9.5 um
Curvature of energy density function	$A_0 = 1$ J/m^3
Height difference of energy density curves	$\Delta B_0 = 0.04$ J/m^3
Interface energy density	$\sigma=1$ J/m^2
Interface thickness	$\lambda=100\times 10^{-9}$m

Based on both the 1-*D* simulation model of heat affect zone during DSS welding and the initial conditions listed in Table 8.1, the variations of volume fraction of δ phase against time are illustrated in Figs. 8.2(a) and (b) for the cases of varying D_δ and D_γ respectively. It is noted that the phase transformation is significantly influenced by the nitrogen diffusion coefficient D_δ, while much weaker by D_γ over the five orders of magnitude. It indicates that the nitrogen diffusion in δ phase affects the γ-to-

δ phase transformation much more pronouncedly than that in γ phase. During the γ-to-δ phase transformation, the newly generated δ phase replaces the original γ phase, which requires the release of nitrogen from the original γ phase and the diffusion and homogenization to stabilize the new δ phase. The rate of this process thus depends much more on D_δ than D_γ. The equilibrium concentrations of nitrogen in both phases are also difficult to determine accurately. We then study further the influences of c_δ^0 and c_γ^0, which are presented in Figs. 8.3(a) and (b). It's observed that the equilibrium content of δ-phase is significantly affected by the equilibrium concentration c_δ^0, while it is approximately unaffected by the variation of c_γ^0. Based on the elementary theory of phase diagram, the equilibrium phase fraction is determined using the condition of mass conservation:

$$c_0 = \phi c_\delta + (1-\phi)c_\gamma \tag{8.6}$$

where c_0 is the overall average concentration of nitrogen. Based on the initial condition listed in Table 8.1, c_0 is 0.18 wt%. If the equilibrium state is considered, c_δ and c_γ are almost identical to the equilibrium concentration c_δ^0 and c_γ^0, which are 0.27 wt% and 0.80 wt%, respectively at the final temperature of 1638 *K*. It is noted that at this high temperature, c_δ^0 is larger than c_0, therefore, the change of c_γ^0 cannot influence the final volume fraction of δ phase, as shown in Fig.8.3(b). However, reducing c_δ^0 to be less than c_0, namely the case of $0.5c_\delta^0$ as shown in Fig. 8.3(a), impact the final δ phase volume fraction. However, the simulation result shown in Fig. 8.3(a) clearly indicated that this equilibrium state is not reached owing to the very short heating time. It is also worthy to remark that although the durations of phase transformation are approximately identical with different c_γ^0, the variations of δ phase volume fraction are significantly different, as shown in Fig. 8.3(b). With a small c_γ^0, the phase transformation would be significantly suppressed at the beginning. This suppression is, however, gradually weaken due to the reduction of γ phase volume fraction during transformation. Thus, the deceleration first and acceleration later for the increase of δ phase is observed in the Fig. 8.3(b). In contrast, the increase of equilibrium concentration c_γ^0 leads to the quick early transition but slow-down at the later stage when the δ phase volume fraction is close to the equilibrium magnitude.

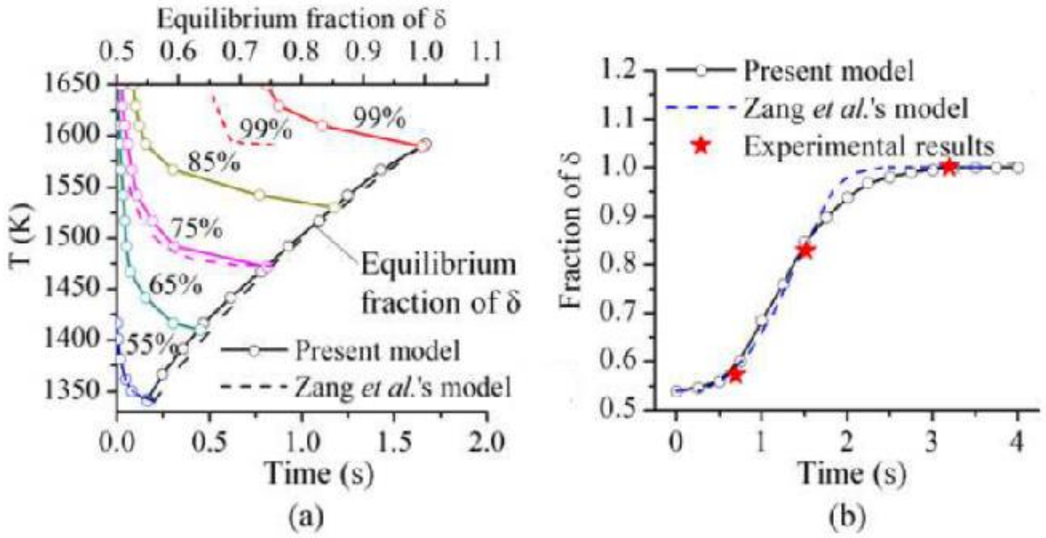

Fig.8.1 (a) TTT diagram for the γ-to-δ transformation of DSS and (b) δ phase evolution during weld heating

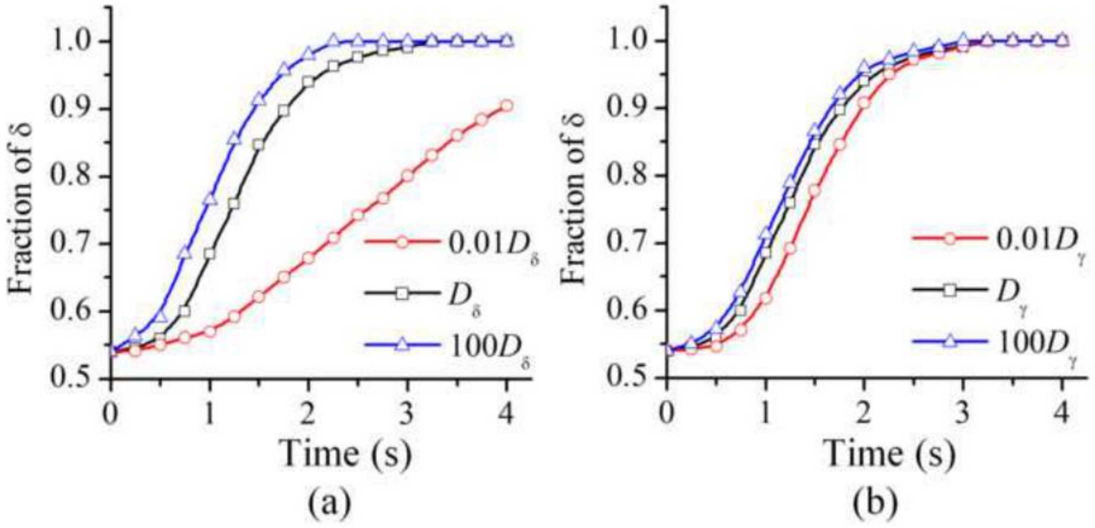

Fig.8.2 The influences of nitrogen diffusion coefficients (a) D_δ and (b) D_γ on the variation of δ phase volume fraction in DSS.

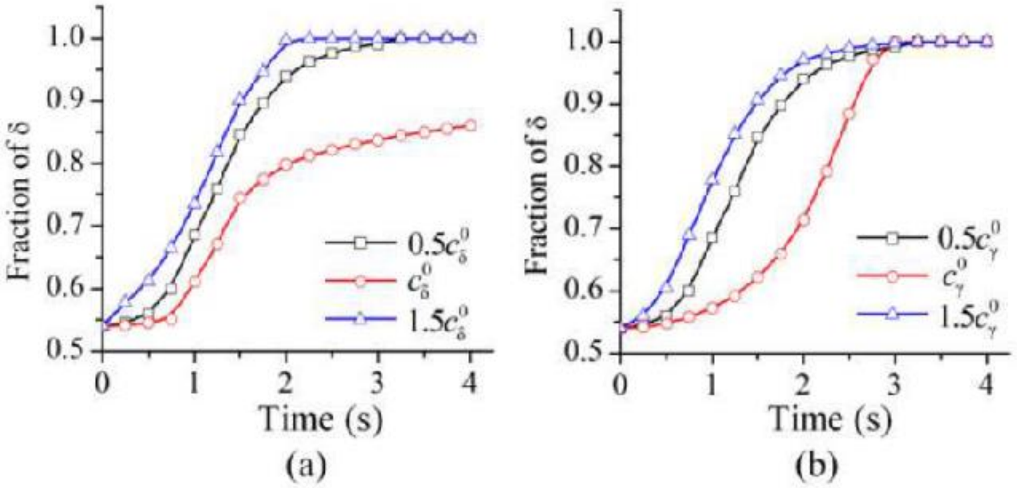

Fig.8.3 The influences of equilibrium nitrogen concentration (a) c_δ^0 and (b) c_γ^0 on the variation of δ phase volume fraction in DSS.

8.3 Simplified phase-field model for understanding Avrami exponent

8.3.1 Solution of 1-D diffusion based on the Fick's laws

The resource-saving DSS investigated in this work contains no nitrogen, even very little carbon. In order to understand the phase evolution in this material, the following assumptions are made: (i) the transformation between δ and γ phases is governed by the diffusion of substances and (ii) the diffusion is due to the exchange of position between vacancy and solute atom. The interphase boundary then serves as a vacancy reservoir to assist the flow of substances. Therefore, the dissolution reaction of δ-to-γ phase is assumed to be controlled on the diffusion of substances. Because dissolution of δ phase is a moving interface, the position of the δ/γ phase boundary is related to a set of partial differential equations that accounts for the flux balance across the interface and to one continuity equation for each phase that satisfies Fick's second law for diffusion. For simplify, the substance (eg. Cr/Al) concentration is distributed evenly in each phase before heat treatment, with δ phase being richer in Cr/Al than that of γ phase as shown in Fig. 8.4(a). $c_{\delta,0}$ and $c_{\gamma,0}$ represent the initial concentrations of Cr in δ and γ phases, respectively. Local equilibrium of Cr is assumed at the δ/γ interface. Fig. 8.4(b) shows the Cr/Al concentration profile during δ-to-γ transformation, where M is the δ/γ interface location, $c_{\delta,M}$ and $c_{\gamma,M}$ are the Cr/Al concentration at the δ/γ interface in δ and γ phases, respectively. Similarly, Schematic representation of the assumed Ni/Mn concentration profile before heat treatment and during δ-to-γ transformation is shown in Fig. 8.4(c) and (d).

The Cr/Al concentration as a function of time (t) and distance (x) is given by Fick's second law of diffusion [120]:

$$\frac{\partial c}{\partial t} = D_{\gamma}\frac{\partial^2 c}{\partial x^2}, \quad \text{in } \gamma \ (0 < \mathrm{x} < M)$$

$$\frac{\partial c}{\partial t} = D_{\delta}\frac{\partial^2 c}{\partial x^2}, \quad \text{in } \delta \ (M < \mathrm{x} < \mathrm{x}_{\gamma}) \tag{8.7}$$

Herein, t is time, and D_{δ} & D_{γ} are the diffusion coefficients of Cr/Al in the δ and γ phases, respectively. For Fig. 8.4(a), the initial conditions for the concentration profile at a time equal to zero are:

$c = c_{\gamma,0} \qquad 0 < \mathrm{x} < M,$

$c = c_{\delta,0} \qquad M < \mathrm{x} < X_{\delta}\, ,$

$$M = X_{\gamma}. \tag{8.8}$$

For Fig. 8.4(b), the boundary conditions for the concentration profile at a time greater than zero are:

$\frac{\partial c}{\partial x} = 0 \qquad x=0 \text{ and } x= X_{\delta}$

$c = c_{\gamma,M} \qquad x=M^-$

$$c = c_{\delta,M} \qquad x=M^+ \tag{8.9}$$

where M^- and M^+ are the locations in γ and δ phases, respectively. Eq. [8.9] implies that Cr/Al concentration has no mass flux across the two boundary surfaces at x=0 and x= X_{δ} and exhibits local equilibrium at δ/γ interface. The interface advance at a rate during the phase transformation, and the location (M) should be determined for solving Eq. (8.7). The interface is assumed to move a distance of dM in a short time period of dt, an equivalent amount of Cr/Al needs to be diffused away. Therefore, the interface location (M) as a function of time is:

$$(c_{\delta,M} - c_{\gamma,M})dM = (D_{\gamma}\frac{\partial c}{\partial x}\bigg|_{M^+} - D_{\delta}\frac{\partial c}{\partial x}\bigg|_{M^-})dt \tag{8.10}$$

Where $\frac{dM}{dt}$ is the interface moving velocity, $(c_{\delta,M} - c_{\gamma,M})dM$ represents the Cr/Al content in the shaded area, and $D_{\gamma}\frac{\partial c}{\partial x}\Big|_{M^+}$ and $-D_{\delta}\frac{\partial c}{\partial x}\Big|_{M^-}$ are the Cr/Al fluxes into the γ and δ phases, respectively. The total mass of Cr/Al in the system is conserved which can be concluded from Eq.(8.10). With the thin δ layer dissolved, the Cr mass in this area was diffused into the bulk regions of δ and γ phases. Therefore, the Cr/Al concentration at the two symmetric boundaries (x=0, x=x_{δ}) increases to an extent which should be depended on the equilibrium Cr concentration at the δ/γ phases interface.

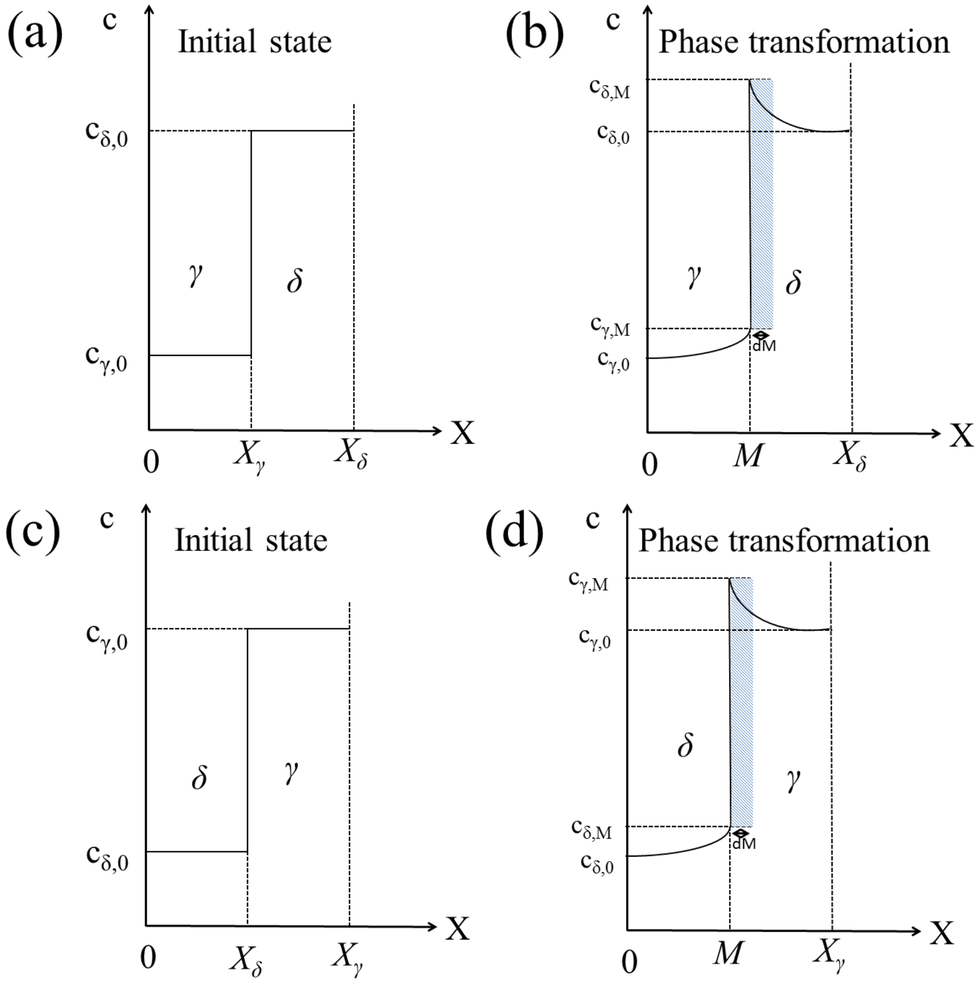

Fig.8.4 Schematic representation of the assumed Cr/Al concentration profile during (a) before heat treatment and (b) δ-to-γ transformation, and the assumed Ni/Mn concentration profile during (c) before heat treatment and (d) δ-to-γ transformation.

Fig.8.4 (b) is taken for the example to obtain the concentration distribution of alloying elements in the individual phase. The δ/γ phase structure can be taken as a diffusioncouple where the two sides do not be affected by the composition diffusion.

Assume an intermediate variable

$$\beta = \frac{x}{2\sqrt{Dt}}, \tag{8.11}$$

Then $\frac{\partial c}{\partial t} = \frac{dc}{d\beta}\frac{\partial \beta}{\partial t} = -\frac{\beta}{2t}\frac{dc}{d\beta}$ (8.12)

While $\frac{\partial^2 c}{\partial x^2} = \frac{\partial^2 c}{\partial \beta^2}(\frac{\partial \beta}{\partial x})^2 = \frac{d^2 c}{d\beta^2}\frac{1}{4Dt}$ (8.13)

Take (8.12) and (8.13) into Fick's second law (8.7),

$$-\frac{\beta}{2t}\frac{dc}{d\beta} = D\frac{1}{4Dt}\frac{d^2 c}{d\beta^2} \tag{8.14}$$

Get $\frac{dc}{d\beta} = A_1 \exp(-\beta^2)$ (8.15)

Integration: $c = A_1 \int_0^{\beta} \exp(-\beta^2) d\beta + A_2$ (8.16)

Then for the individual γ phase, it can be taken as a diffusion body where the left side does not be affected by composition diffusion. The initial conditions for the concentration profile at a time equal to zero are:

$t = 0, x \geq 0, \quad c = c_{\gamma,0}$ (8.17)

the boundary conditions for the concentration profile at a time greater than zero are:

$t > 0, x = 0, \quad c = c_{\gamma,M}$

$x = \infty, c = c_{\gamma,0}$ (8.18)

According to Eq. (8.16), the Cr/Al concentration distribution in γ phase is obtained as follows:

$$C(x,t) = c_{\gamma,M} - (c_{\gamma,M} - c_{\gamma,0})\mathrm{erf}(\frac{x}{2\sqrt{Dt}}) \tag{8.19}$$

8.3.2 The general case and the explanation of the Avrami exponent

For the three-dimensional case, the conservation law of a substance *i* can be written as follows:

$$\frac{d}{dt}\left(\int_{V_\delta} c_i dV + \int_{V_\gamma} c_i dV\right) = 0\,, \tag{8.20}$$

where *c* denotes the local concentration, V_δ and V_γ are the volumes of *δ* and *γ* phases respectively. Noting that there is no source or sink of any substance and that the flow of material at the boundary of a phase is due to both local vacancy-atom exchange and the migration of boundaries, we can then recast Eq. (8.20) using Stokes theorem as

$$\int_{S_\delta} \mathbf{n}_\delta \cdot \left(\mathbf{J}_i^\delta + c_i^\delta \mathbf{u}\right) dS + \int_{S_\gamma} \mathbf{n}_\gamma \cdot \left(\mathbf{J}_i^\gamma + c_i^\gamma \mathbf{u}\right) dS = 0\,, \tag{8.21}$$

where *S* indicates boundary of a phase, J_i is the concentration flow of material at the boundary, *u* is the velocity of boundary migration and *n* is the outwards normal vector of the boundary. Suppose that the interphase boundary is the only region where material flow occurs and noting that $\mathbf{n}_\delta = -\mathbf{n}_\gamma$, Eq. (8.21) is then simplified as

$$\int_A \left(J_i^\delta + J_i^\gamma\right) + \left(c_i^{\delta e} - c_i^{\gamma e}\right) u\, dA = 0\,, \tag{8.22}$$

where *A* is the area of the interface, $J_i^\delta = \mathbf{n}_\delta \cdot \mathbf{J}_i$, $J_i^\gamma = \mathbf{n}_\gamma \cdot \mathbf{J}_i$ and $u = \mathbf{n}_\delta \cdot \mathbf{u}$. Since the interface is a vacancy reservoir, we suppose that the concentration of either *γ* or *δ* phase forming elements near the interface can quickly approach the equilibrium magnitude. Therefore, the concentrations at the both sides of interface *A* in Eq. (8.22) has been replaced by the equivalent values $c_i^{\delta e}$ and $c_i^{\gamma e}$. Apparently, the migration velocity *u* of the phase boundary cannot depend on the species in diffusion *i*. Therefore, the total flow into the phase boundary from both sides $J_i = \left(J_i^\delta + J_i^\gamma\right)$ must satisfy the constraint of Eq. (8.22) for any substance i. We then remove the subscript i in the following discussion since solution from any substance shall be identical. If the total flow into the interphase boundary J is time-independent, the velocity u becomes constant. The kinetics of phase growth then mainly depends on the geometry of the phase. For example, for an uniform nucleation and spherical growth, Avrami's theory renders: $\phi_\gamma = 1 - \exp\left(-kt^4\right)$, where ϕ is the volume fraction of γ phase which grows from the δ phase in the isothermal hold. The general Avrami equation is given as: $\phi_\gamma = 1 - \exp\left(-kt^n\right)$, where the fact that $n < 4$ is generally attributed to non-spherical growth. However, for our material, the flow J can hardly be treated to be time-impendent since it depends on the deviation from the equilibrium concentration, which must diminish when time increase. Therefore, we alternatively assume that the concentration near the boundary is a Gauss error function:

$$c^{\delta(\gamma)}(x,t) = c^{\delta e(\gamma e)} + \left(c_0^{\delta(\gamma)} - c^{\delta e(\gamma e)}\right)\left(1\text{-}\operatorname{erf}\left(\frac{x}{2\sqrt{D_{\delta(\gamma)}t}}\right)\right), \tag{8.23}$$

Which is arisen from the transient solution of the Fick's second law for a one-dimensional diffusion. The subscript "0" indicates the value at $t = 0$, the variable x is the distance from the interface and D is the diffusion constant. Using the Fick's first law, the time-dependence of J_i can be given in the form as:

$$J = -\left(D_\delta \frac{\partial c^\delta}{\partial x} + D_\gamma \frac{\partial c^\gamma}{\partial x}\right) = \left(\frac{c_0^\delta - c^{\delta e}}{\sqrt{\pi D_\delta}} + \frac{c_0^\gamma - c^{\gamma e}}{\sqrt{\pi D_\gamma}}\right)\frac{1}{\sqrt{t}}, \tag{8.24}$$

which indicates that the migration of the interphase boundary satisfies the scaling

$$u \sim \frac{1}{\sqrt{t}}, \tag{8.25}$$

Now considering a spherical growth from a γ nucleus, the volume of this γ phase V_1 at time t should follow the scaling:

$$V_1 \sim t^{3/2} \tag{8.26}$$

since $\frac{d\left(V_1^{1/3}\right)}{dt} \sim u \sim \frac{1}{\sqrt{t}}$ due to Eq. [8.25].

Considering a constant nucleating rate from the remaining δ phase and noting that only the fraction $\left(\phi^e - \phi\right)$ is the net nucleation for γ phase, the Avrami's argument on uniform nucleation leads to:

$$d\phi_\gamma \sim \left(\phi_\gamma^e - \phi_\gamma\right)\left(t-\tau\right)^{3/2} d\tau \tag{8.27}$$

which leads to

$$f = \phi_\gamma \big/ \phi_\gamma^e = 1 - \exp\left(-\left(t/\tau\right)^{5/2}\right), \tag{8.28}$$

where $n = 2.5$ is obtained and used in apprehending experimental results.

8.4 Conclusion

This chapter propose the assumption that the dissolution reaction of δ-to-γ in DSS without of nitrogen content is controlled on the diffusion of substances. The concentration distribution of alloying elements during phase evolution is calculated, and the phase evolution of δ-to-γ transformation in DSS 15Cr-2Al-2Ni-11Mn is modeled using Avrami equation.

A FE-based phase field approach is applied to the investigation of phase transformation of DSS. TTT diagram and δ phase evolution in the heat-affected zone during welding are analyzed and compared with the conventional model as well as the experimental data. The 1-D simulation of γ-to-δ transformation during weld heating is carried out to investigate the influence of diffusion properties. It is found that the nitrogen diffusion in δ phase rather than that in γ phase dominates the transformation. The elevations of diffusion coefficient D_δ and the equilibrium concentration c_δ^0, which are directly beneficial for this process, promotes the phase transformation.

Chapter 9 Conclusion and future work

9.1 Conclusion

This work investigates the effect of annealing temperature and time, cooling rate, and plastic deformation on the phase transformation of 15Cr-2Al-2Ni-11Mn. Then a series of DSS samples with the same phase constituent but different microstructure obtained by different heat treatments were conducted to exhibit mechanical property. Following research on mechanical performance was taken to the precipitation hardening effect of σ phase on DSS alloy. Finally, a finite element based phase field approach is applied to the investigation of phase transformation of DSS.

The main findings are:

1. Using the copper-mold suction casting, the raw DSS can have 70% δ phase, and it significantly expands the annealing temperature range on adjusting the phase constitution, morphology and grain sizes.
2. The primary phase transformation is δ-to-γ phase when the annealing temperature is less than 1050 °C, but becomes γ-to-δ phase at higher temperature for rapidly-solidified DSS 15Cr-2Al-2Ni-11Mn.
3. It is found that plastic deformation not only changes the rate of phase transformation, the grain size of new phase but also the equilibrium phase constitution. Plastic deformation suppress the δ-to-γ phase transformation, while promotes the inverse one. After 70% cold rolling, the maximum γ phase content

after long isothermal annealing occurs at about 850 °C. This effect of plastic deformation has never been reported before.

4. Based on Avrami equation, TTT diagrams of as-cast and cold-rolled DSS samples were established. It is found that the stretched exponent n is about 2.5 by fitting the experimental data, which can be explained based on a simplified model of diffusion-mediated phase transformation.
5. Based on the non-equilibrium kinetics diagram and the effect of cooling method, DSS with about 50% δ phase was prepared using different non-equilibrium thermal process. It was found that the mechanical performance of DSS is optimised by plastic deformation and low temperature annealing. This solution brings about bimodal size of γ grain, which acts as reinforcing and toughening phase and leads to an excellent combination of strength and ductility of DSS.
6. The annealing temperature and cooling rate affect the partition coefficient of alloying elements, which can be correlated to the variation of δ phase volume fraction. When the δ phase fraction increases, the partition coefficient becomes more uniform and close to 1.
7. With the annealing time increases, the partition coefficients of Cr and Al increase while those of Ni and Mn decrease, finally levels off after the DSS sample reaching isothermal phase-equilibrium state.
8. No any dependent effect of the partition coefficient of alloying elements between δ and γ phases on the overall corrosion resistance of DSS was found. The microstructure, particularly the contact area between the δ and γ phases exhibits

impact on the overall corrosion resistance of DSS.

9. The contrast of corrosion resistance between *δ* and *γ* phases varies owing to the change of the partition coefficients of alloying elements. Longer annealing time is beneficial for improving the corrosion resistance of *δ* phase if the annealing temperature leads to *δ*-to-*γ* phase transformation in DSS. Higher annealing temperature, at which *γ*-to-*δ* phase transformation occurs in DSS samples, can rapidly increase the corrosion resistance of *δ* phase.
10. Upon aging at 750~900 ºC, the *σ* phase precipitates in the DSS, and the size and amount of *σ* phase increase continuously with aging time.
11. TTT diagram of *σ* phase precipitation is established, and the kinetics of *σ* phase formation reaches peak at about 850 ºC aging.
12. Mo increases the formation rate and the mass amount of *σ* phase, and favorites *σ* phase precipitated in *δ* phase.

13. The *σ* phase most increase the strength and decrease the elongation when its volume fraction is approximately 1.5%.

14. The assumption that the dissolution reaction of *δ*-to-*γ* phase in DSS without of nitrogen content is controlled on the diffusion of substances is proposed. The concentration distribution of alloying elements during phase evolution is calculated, and the phase evolution of *δ*-to-*γ* phase transformation in DSS 15Cr-2Al-2Ni-11Mn is modeled using Avrami equation.

15. TTT diagram and *δ* phase evolution in the heat-affected zone during welding are

analyzed and compared with the conventional model as well as the experimental data. The 1-D simulation of γ-to-δ phase transformation during welding is carried out to investigate the influence of diffusion properties. It is found that the nitrogen diffusion in δ phase rather than that in γ phase dominates the transformation. The elevations of diffusion coefficient D_δ and the equilibrium concentration c_δ^0, which are directly beneficial for this process, promotes the phase transformation.

9.2 Future work

We have paid effort on experimental and theoretical studies related to the load-bearing capacity and corrosion resistance of DSS. The microstructure-strength relationships of DSS was shown, and more advanced and accurate techniques may be used to enhance the strength and deformability of DSS in future work.

The deformation ability of δ and γ phases is different. Therefore, the hot and cold processing performance of DSS is poor. It is essential for researchers to find a way to promote the deformability of DSS while keeping the strength as high as possible. The solutions may include grain refinement, precipitation hardening, and transformation induced plasticity (TRIP) effect.

Surface mechanical attrition treatment (SMAT) improve surface structures and properties of metals by impact of shots and or milling balls, and the grain size is refined to the nanometer scale. The recent studies shows that SMAT can increase effectively the tensile and bending strength, the thermal stability and the fatigue life of AISI 316L [48, 49]. Aging is a heat treatment technique used to induce precipitation hardening and increase the yield strength of malleable materials. Most structural alloys of aluminum, magnesium, nickel, titanium, and some stainless steels can be aged to precipitate secondary phases for achieving a higher strength. It relies on the variation of solid solubility with temperature to produce fine particles of an impurity phase, which impede the movement of dislocations or other defects in a crystal lattice. The fine and homogeneous dispersion of σ phase can play a role of precipitation strengthening in stainless steels [56, 57]. TRIP effect is that phase transformation evenly spread throughout the material so that deformation does not concentrate in the local, leading to the improvement on the strength and ductility of DSS. It has been used to get high-performance DSS [46].

The comprehensive investigation on improving the mechanical performance of DSS using the combination of precipitation hardening and TRIP effect is rarely found. It may further make some progress to the performance of DSS based on previous achievement using single technology.

Reference

[1] J.-O. Nilsson, Super duplex stainless steels, Materials science and technology 8(8) (1992) 685-700.

[2] I.N. Bastos, S.S. Tavares, F. Dalard, R.P. Nogueira, Effect of microstructure on corrosion behavior of superduplex stainless steel at critical environment conditions, Scripta Materialia 57(10) (2007) 913-916.

[3] R. Badji, M. Bouabdallah, B. Bacroix, C. Kahloun, K. Bettahar, N. Kherrouba, Effect of solution treatment temperature on the precipitation kinetic of σ-phase in 2205 duplex stainless steel welds, Materials Science and Engineering: A 496(1) (2008) 447-454.

[4] T. Chen, K. Weng, J. Yang, The effect of high-temperature exposure on the microstructural stability and toughness property in a 2205 duplex stainless steel, Materials Science and Engineering: A 338(1) (2002) 259-270.

[5] S. Chen, H. Davies, W. Rainforth, Austenite phase formation in rapidly solidified Fe–Cr–Mn–C steels, Acta materialia 47(18) (1999) 4555-4569.

[6] M. Li, H. Chang, P. Kao, D. Gan, The effect of Mn and Al contents on the solvus of κ phase in austenitic Fe-Mn-Al-C alloys, Materials chemistry and physics 59(1) (1999) 96-99.

[7] J. Betancur-Rios, K. Nomura, C. Wang, G. Pérez Alcázar, J. Tabares, ICEMS study of isothermal oxidation of Fe–Mn–Al–C–Cr–Si–Mo, Fe–Mn–Al–C–Cr–Si and Fe–9Cr–1Mo alloys, ICAME 2007 (2009) 1129-1134.

[8] J. Lee, C. Wu, T. Liu, The influence of Cr alloying on microstructures of Fe–Al–Mn–Cr alloys, Scripta Materialia 50(11) (2004) 1389-1393.

[9] J. Wan, Q. Ran, J. Li, Y. Xu, X. Xiao, H. Yu, L. Jiang, A new resource-saving, low chromium and low nickel duplex stainless steel 15Cr–xAl–2Ni–yMn, Materials & Design 53 (2014) 43-50.

[10] A.L. Schaeffler, Selection of austenitic electrodes for welding dissimilar metals, Welding journal 26(10) (1947) 601-620.

[11] H. Sieurin, R. Sandström, Sigma phase precipitation in duplex stainless steel 2205, Materials Science and Engineering: A 444(1) (2007) 271-276.

[12] 余存烨, 节镍不锈钢的开发与展望, 化工设备与管道 45(2) (2008) 4-8.

[13] C. Wang, Y. Xiang, C. Wang, Buckling of standing vertical plates under body forces, International Journal of Structural Stability and Dynamics 2(02) (2002) 151-161.

[14] 李正邦, 超洁净钢的新进展, 材料与冶金学报 1(3) (2002) 161-165.

[15] 熊云龙, 娄延春, 刘新峰, 不锈钢材料研究的新进展, 热加工工艺 (5) (2005) 51-53.

[16] E.C. Bain, W.E. Griffiths, An introduction to the iron-chromium-nickel alloys, Trans. AIME 75(166) (1927) 166-211.

[17] 牛琳霞, 我国不锈钢生产和技术发展方向, 钢铁研究 35(6) (2007) 46-49.

[18] J. Charles, P. Chemelle, 胡锦程, 张伟, 双相不锈钢的发展现状及未来市场趋势, 世界钢铁 6 (2011) 1-22.

[19] S. Sohn, B.-J. Lee, S. Lee, N. Kim, J.-H. Kwak, Effect of annealing temperature on microstructural modification and tensile properties in 0.35 C–3.5 Mn–5.8 Al lightweight steel, Acta Materialia 61(13) (2013) 5050-5066.

[20] S. Li, Y. Wang, X. Wang, Effects of ferrite content on the mechanical properties of thermal aged duplex stainless steels, Materials Science and Engineering: A 625 (2015) 186-193.

[21] L. Chen, H. Tan, Z. Wang, J. Li, Y. Jiang, Influence of cooling rate on microstructure evolution and pitting corrosion resistance in the simulated heat-affected zone of 2304 duplex stainless steels,

Corrosion Science 58 (2012) 168-174.

[22] C. Luo, G. Weatherly, The invariant line and precipitation in a Ni-45 wt% Cr alloy, Acta metallurgica 35(8) (1987) 1963-1972.

[23] T. Fujii, T. Mori, M. Kato, Crystallography and morphology of needle-like α-Fe precipitate particles in a Cu matrix, Acta metallurgica et materialia 40(12) (1992) 3413-3420.

[24] C. Luo, U. Dahmen, K. Westmacott, Morphology and crystallography of Cr precipitates in a Cu-0.33 wt% Cr alloy, Acta metallurgica et materialia 42(6) (1994) 1923-1932.

[25] H. Sieurin, R. Sandström, Austenite reformation in the heat-affected zone of duplex stainless steel 2205, Materials Science and Engineering: A 418(1) (2006) 250-256.

[26] H. Hemmer, Ø. Grong, A process model for the heat-affected zone microstructure evolution in duplex stainless steel weldments: Part I. the model, Metallurgical and Materials Transactions A 30(11) (1999) 2915-2929.

[27] S. Hertzman, B. Brolund, P.J. Ferreira, An experimental and theoretical study of heat-affected zone austenite reformation in three duplex stainless steels, Metallurgical and materials transactions A 28(2) (1997) 277-285.

[28] W. Zhang, T. DebRoy, T. Palmer, J. Elmer, Modeling of ferrite formation in a duplex stainless steel weld considering non-uniform starting microstructure, Acta Materialia 53(16) (2005) 4441-4453.

[29] K.D. Ramkumar, D. Mishra, B.G. Raj, M. Vignesh, G. Thiruvengatam, S. Sudharshan, N. Arivazhagan, N. Sivashanmugam, A.M. Rabel, Effect of optimal weld parameters in the microstructure and mechanical properties of autogeneous gas tungsten arc weldments of super-duplex stainless steel UNS S32750, Materials & Design 66 (2015) 356-365.

[30] S. Geng, J. Sun, L. Guo, H. Wang, Evolution of microstructure and corrosion behavior in 2205 duplex stainless steel GTA-welding joint, Journal of Manufacturing Processes 19 (2015) 32-37.

[31] L. Guo, X. Zhao, M. Li, W. Zhang, Y. Bai, L. Qiao, Annealing effects on the microstructure and magnetic domain structures of duplex stainless steel studied by in situ technique, Applied Surface Science 259 (2012) 213-218.

[32] Q. Ran, Y. Xu, J. Li, J. Wan, X. Xiao, H. Yu, L. Jiang, Effect of heat treatment on transformation-induced plasticity of economical Cr19 duplex stainless steel, Materials & Design 56 (2014) 959-965.

[33] J.K.L. Lai, K.W. Wong, D.J. Li, Effect of solution treatment on the transformation behaviour of cold-rolled duplex stainless steels, Materials Science and Engineering: A 203(1) (1995) 356-364.

[34] S. Harjo, Y. Tomota, P. Lukáš, D. Neov, M. Vrána, P. Mikula, M. Ono, In situ neutron diffraction study of α–γ Fe–Cr–Ni alloys under tensile deformation, Acta Materialia 49(13) (2001) 2471-2479.

[35] E.-Y. Guo, H.-X. Xie, S.S. Singh, A. Kirubanandham, T. Jing, N. Chawla, Mechanical characterization of microconstituents in a cast duplex stainless steel by micropillar compression, Materials Science and Engineering: A 598 (2014) 98-105.

[36] J.J. Moverare, M. Odén, Influence of elastic and plastic anisotropy on the flow behavior in a duplex stainless steel, Metallurgical and Materials Transactions A 33(1) (2002) 57-71.

[37] T.-H. Lee, H.-Y. Ha, J.-Y. Kang, B. Hwang, W. Woo, E. Shin, In situ and ex situ neutron diffraction study on deformation behavior of high-nitrogen, Ni-free duplex stainless steel, Scripta Materialia 67(2) (2012) 141-144.

[38] J. Foct, N. Akdut, Cleavage-like fracture of austenite in duplex stainless steel, Scripta metallurgica et materialia 29(2) (1993) 153-158.

[39] Q. Feng, C. Jiang, Z. Xu, L. Xie, V. Ji, Effect of shot peening on the residual stress and microstructure of duplex stainless steel, Surface and Coatings Technology 226 (2013) 140-144.

[40] Y. Han, D. Zou, Z. Chen, G. Fan, W. Zhang, Investigation on hot deformation behavior of 00Cr23Ni4N duplex stainless steel under medium–high strain rates, Materials Characterization 62(2) (2011) 198-203.

[41] B. Chéhab, Y. Bréchet, M. Véron, P. Jacques, G. Parry, J.-D. Mithieux, J.-C. Glez, T. Pardoen, Micromechanics of high-temperature damage in dual-phase stainless steel, Acta Materialia 58(2) (2010) 626-637.

[42] P. Hedström, T. Han, U. Lienert, J. Almer, M. Odén, Load partitioning between single bulk grains in a two-phase phase duplex stainless steel during tensile loading, Acta Mater 5 (2010) 734-744.

[43] S. Fréchard, F. Martin, C. Clément, J. Cousty, AFM and EBSD combined studies of plastic deformation in a duplex stainless steel, Materials Science and Engineering: A 418(1) (2006) 312-319.

[44] L. Chen, F. Yuan, P. Jiang, J. Xie, X. Wu, Simultaneous improvement of tensile strength and ductility in micro-duplex structure consisting of austenite and ferrite, Materials Science and Engineering: A 618 (2014) 563-571.

[45] T. Maki, T. Furuhara, K. Tsuzaki, Advances in Physical Metallurgy and Processing of Steels. Microstructure Development by Thermomechanical Processing in Duplex Stainless Steel, ISIJ international 41(6) (2001) 571-579.

[46] C. Herrera, D. Ponge, D. Raabe, Design of a novel Mn-based 1GPa duplex stainless TRIP steel with 60% ductility by a reduction of austenite stability, Acta Materialia 59(11) (2011) 4653-4664.

[47] R. Silva, L. Baroni, M. Silva, C. Afonso, S. Kuri, C. Rovere, Effect of thermal aging at 475° C on the properties of lean duplex stainless steel 2101, Materials Characterization 114 (2016) 211-217.

[48] T. Roland, D. Retraint, K. Lu, J. Lu, Fatigue life improvement through surface nanostructuring of stainless steel by means of surface mechanical attrition treatment, Scripta Materialia 54(11) (2006) 1949-1954.

[49] X. Chen, J. Lu, L. Lu, K. Lu, Tensile properties of a nanocrystalline 316L austenitic stainless steel, Scripta Materialia 52(10) (2005) 1039-1044.

[50] J. Charles, S. Bernhardsson, Duplex Stainless Steels'91. Vol. 1, Beaune, France, 28-30 Oct. 1991 (1991) 1991.

[51] T.M.D. H.D. Solomon, Proceedings of conference on Duplex Stainless Steels, ASM, Metal park, OH, 1983.

[52] V.S. Moura, L.D. Lima, J.M. Pardal, A.Y. Kina, R.R.A. Corte, S.S.M. Tavares, Influence of microstructure on the corrosion resistance of the duplex stainless steel UNS S31803, Materials Characterization 59(8) (2008) 1127-1132.

[53] T. Karahan, H. Ertek Emre, M. Tümer, R. Kaçar, Strengthening of AISI 2205 duplex stainless steel by strain ageing, Materials & Design 55 (2014) 250-256.

[54] C.-S. Huang, C.-C. Shih, Effects of nitrogen and high temperature aging on σ phase precipitation of duplex stainless steel, Materials Science and Engineering: A 402(1) (2005) 66-75.

[55] S. Ghosh, S. Mondal, High temperature ageing behaviour of a duplex stainless steel, Materials Characterization 59(12) (2008) 1776-1783.

[56] C. Shek, K. Wong, J. Lai, Review of temperature indicators and the use of duplex stainless steels for life assessment, Materials Science and Engineering: R: Reports 19(5-6) (1997) 153-200.

[57] J. Lai, K. Wong, D. Li, Effect of solution treatment on the transformation behaviour of cold-rolled duplex stainless steels, Materials Science and Engineering: A 203(1-2) (1995) 356-364.

[58] Y.-J. Kim, L.S. Chumbley, B. Gleeson, Determination of isothermal transformation diagrams for sigma-phase formation in cast duplex stainless steels CD3MN and CD3MWCuN, Metallurgical and Materials Transactions A 35(11) (2004) 3377-3386.

[59] G. Weatherly, P. Humble, D. Borland, Precipitation in a Cu-0, 55 wt.% Cr alloy, Acta Metallurgica 27(12) (1979) 1815-1828.

[60] H.-S. Cho, K. Lee, Effect of cold working and isothermal aging on the precipitation of sigma phase in 2205 duplex stainless steel, Materials Characterization 75 (2013) 29-34.

[61] J. Charles, Proceedings Conf. Duplex Stainless Steels, Beaune, France, Les editions de physique 1 (1991) 3-48.

[62] S. Pak, L. Karlsson, Optimizing the properties of duplex stainless weld metals by addition of nitrogen, Scand. J. Metall. 19(1) (1990) 9-13.

[63] R. Dakhlaoui, A. Baczmański, C. Braham, S. Wroński, K. Wierzbanowski, E. Oliver, Effect of residual stresses on individual phase mechanical properties of austeno-ferritic duplex stainless steel, Acta materialia 54(19) (2006) 5027-5039.

[64] W. Quach, J. Teng, K. Chung, Residual stresses in press-braked stainless steel sections, I: Coiling and uncoiling of sheets, Journal of Constructional Steel Research 65(8) (2009) 1803-1815.

[65] P. Withers, H. Bhadeshia, Residual stress. Part 2–Nature and origins, Materials science and technology 17(4) (2001) 366-375.

[66] R.B. Cruise, L. Gardner, Residual stress analysis of structural stainless steel sections, Journal of Constructional Steel Research 64(3) (2008) 352-366.

[67] V. Silberschmidt, E. Werner, Analysis of thermal residual stresses in duplex-type materials, Computational materials science 16(1) (1999) 39-52.

[68] R. Cruise, L. Gardner, Residual stress analysis of structural stainless steel sections, Journal of Constructional Steel Research 64(3) (2008) 352-366.

[69] J. Stolarz, J. Foct, Specific features of two phase alloys response to cyclic deformation, Materials Science and Engineering: A 319–321 (2001) 501-505.

[70] J. POLÁK, P. ZEZULKA, Short crack growth and fatigue life in austenitic ‐ ferritic duplex stainless steel, Fatigue & Fracture of Engineering Materials & Structures 28(10) (2005) 923-935.

[71] V. Kazymyrovych, Very high cycle fatigue of tool steels, Karlstad University, 2010.

[72] Y. Murakami, T. Nomoto, T. Ueda, Factors influencing the mechanism of superlong fatigue failure in steels, Fatigue and Fracture of Engineering Materials and Structures 22(7) (1999) 581-590.

[73] Y. Murakami, T. Nomoto, T. Ueda, On the mechanism of fatigue failure in the superlong life regime (N> 107 cycles). Part II: influence of hydrogen trapped by inclusions, Fatigue & Fracture of Engineering Materials & Structures 23(11) (2000) 903-910.

[74] L.-L. Zhang, Y.-H. Fei, X.-Y. Liu, M.-X. Li, On the formation mechanisms of fine granular area (FGA) on the fracture surface for high strength steels in the VHCF regime, International Journal of Fatigue 82 (2016) 402-410.

[75] M.W. Tofique, J. Bergström, K. Svensson, Very high cycle fatigue of cold rolled stainless steels, crack initiation and formation of the fine granular area, International Journal of Fatigue (2017).

[76] R. Mathis, Initiation and early growth mechanisms of corrosion fatigue cracks in stainless steels, Journal of materials science 22(3) (1987) 907-914.

[77] T. Magnin, J. Lardon, L. Coudreuse, A new approach to low cycle fatigue behavior of a duplex stainless steel based on the deformation mechanisms of the individual phases, Low cycle fatigue, ASTM International1988.

[78] H. Hayden, S. Floreen, The fatigue behavior of fine grained two-phase alloys, Metallurgical Transactions 4(2) (1973) 561-568.

[79] W. Vermeulen, P. Morris, A.d. Weijer, S. Van der Zwaag, Prediction of martensite start temperature

using artificial neural networks, Ironmaking and Steelmaking 23(5) (1996) 433-437.

[80] J.W. Christian, The Theory of Transformations in Metals and Alloys Ediz 2. an Advanced Textbook in Physical Metallurgy Parte 1. Equilibrium and General Kinetic Theory, Pergamon Press1975.

[81] R. Magnabosco, Kinetics of sigma phase formation in a duplex stainless steel, Materials Research 12(3) (2009) 321-327.

[82] R. Badji, M. Bouabdallah, B. Bacroix, C. Kahloun, B. Belkessa, H. Maza, Phase transformation and mechanical behavior in annealed 2205 duplex stainless steel welds, Materials Characterization 59(4) (2008) 447-453.

[83] R.Z. Valiev, N. Krasilnikov, N. Tsenev, Plastic deformation of alloys with submicron-grained structure, Materials Science and Engineering: A 137 (1991) 35-40.

[84] P. Williams, R. Faulkner, Chemical volume diffusion coefficients for stainless steel corrosion studies, Journal of materials science 22(10) (1987) 3537-3542.

[85] C. Shek, K. Wong, J. Lai, D. Li, Hot tensile properties of 25Cr-8Ni duplex stainless steel containing cellular (σ+ γ 2) structure after various thermal treatments, Materials Science and Engineering: A 231(1) (1997) 42-47.

[86] J. Lai, K. Wong, D. Li, Effect of solution treatment on the transformation behaviour of cold-rolled duplex stainless steels, Materials Science and Engineering: A 203(1) (1995) 356-364.

[87] N. Jia, R.L. Peng, D. Brown, B. Clausen, Y. Wang, Tensile deformation behavior of duplex stainless steel studied by in-situ time-of-flight neutron diffraction, Metallurgical and Materials Transactions A 39(13) (2008) 3134-3140.

[88] M.T. Hutchings, P.J. Withers, T.M. Holden, T. Lorentzen, Introduction to the characterization of residual stress by neutron diffraction, CRC press2005.

[89] M. Daymond, M. Bourke, R. Von Dreele, B.r. Clausen, T. Lorentzen, Use of Rietveld refinement for elastic macrostrain determination and for evaluation of plastic strain history from diffraction spectra, Journal of Applied Physics 82(4) (1997) 1554-1562.

[90] S. Harjo, Y. Tomota, P. Lukáš, D. Neov, M. Vrana, P. Mikula, M. Ono, In situ neutron diffraction study of α–γ Fe–Cr–Ni alloys under tensile deformation, Acta materialia 49(13) (2001) 2471-2479.

[91] R.W. Carpick, D.F. Ogletree, M. Salmeron, A general equation for fitting contact area and friction vs load measurements, Journal of colloid and interface science 211(2) (1999) 395-400.

[92] A. Chen, H. Ruan, J. Wang, H. Chan, Q. Wang, Q. Li, J. Lu, The influence of strain rate on the microstructure transition of 304 stainless steel, Acta materialia 59(9) (2011) 3697-3709.

[93] C. San Marchi, B. Somerday, X. Tang, G. Schiroky, Effects of alloy composition and strain hardening on tensile fracture of hydrogen-precharged type 316 stainless steels, International Journal of Hydrogen Energy 33(2) (2008) 889-904.

[94] M. Martin, S. Weber, W. Theisen, T. Michler, J. Naumann, Development of a stable high-aluminum austenitic stainless steel for hydrogen applications, International Journal of Hydrogen Energy 38(14) (2013) 5989-6001.

[95] R. Schramm, R. Reed, Stacking fault energies of seven commercial austenitic stainless steels, Metallurgical Transactions A 6(7) (1975) 1345-1351.

[96] C.G. Rhodes, A.W. Thompson, The composition dependence of stacking fault energy in austenitic stainless steels, Metallurgical Transactions A 8(12) (1977) 1901-1906.

[97] P. Brofman, G. Ansell, On the effect of carbon on the stacking fault energy of austenitic stainless steels, Metallurgical and Materials Transactions A 9(6) (1978) 879-880.

[98] T. Yonezawa, K. Suzuki, S. Ooki, A. Hashimoto, The effect of chemical composition and heat

treatment conditions on stacking fault energy for Fe-Cr-Ni austenitic stainless steel, Metallurgical and Materials Transactions A 44(13) (2013) 5884-5896.

[99] S. Curtze, V.T. Kuokkala, A. Oikari, J. Talonen, H. Hänninen, Thermodynamic modeling of the stacking fault energy of austenitic steels, Acta Materialia 59(3) (2011) 1068-1076.

[100] Y. Wang, M. Chen, F. Zhou, E. Ma, High tensile ductility in a nanostructured metal, Nature 419(6910) (2002) 912-915.

[101] U. Andrade, M. Meyers, K. Vecchio, A.H. Chokshi, Dynamic recrystallization in high-strain, high-strain-rate plastic deformation of copper, Acta metallurgica et materialia 42(9) (1994) 3183-3195.

[102] C. Youngdahl, J. Weertman, R. Hugo, H. Kung, Deformation behavior in nanocrystalline copper, Scripta Materialia 44(8) (2001) 1475-1478.

[103] Z. Fan, P. Tsakiropoulos, P. Smith, A. Miodownik, Extension of the Hall-Petch relation to two-ductile-phase alloys, Philosophical Magazine A 67(2) (1993) 515-531.

[104] S. Rajasekhara, P. Ferreira, L. Karjalainen, A. Kyröläinen, Hall–Petch behavior in ultra-fine-grained AISI 301LN stainless steel, Metallurgical and Materials Transactions A 38(6) (2007) 1202-1210.

[105] A. Di Schino, J. Kenny, Grain size dependence of the fatigue behaviour of a ultrafine-grained AISI 304 stainless steel, Materials Letters 57(21) (2003) 3182-3185.

[106] M. Shirdel, H. Mirzadeh, M.H. Parsa, Enhanced Mechanical Properties of Microalloyed Austenitic Stainless Steel Produced by Martensite Treatment, Advanced Engineering Materials 17(8) (2015) 1226-1233.

[107] R. Silva, L.F.S. Baroni, M.B.R. Silva, C.R.M. Afonso, S.E. Kuri, C.A.D. Rovere, Effect of thermal aging at 475 °C on the properties of lean duplex stainless steel 2101, Materials Characterization 114 (2016) 211-217.

[108] J. Wan, H. Ruan, J. Wang, S. Shi, Exploiting the non-equilibrium phase transformation in a 15Cr-2Ni-2Al-11Mn resource-saving duplex stainless steel, Materials & Design 114 (2017) 433-440.

[109] S. Atamert, J. King, Elemental partitioning and microstructural development in duplex stainless steel weld metal, Acta metallurgica et materialia 39(3) (1991) 273-285.

[110] M. Cortie, J. Potgieter, The effect of temperature and nitrogen content on the partitioning of alloy elements in duplex stainless steels, Metallurgical Transactions A 22(10) (1991) 2173-2179.

[111] J. Li, Z. Zhang, H. Chen, X. Xiao, J. Zhao, L. Jiang, New Economical 19Cr Duplex Stainless Steels, Metallurgical and Materials Transactions A 43(2) (2012) 428-436.

[112] F. Hull, Delta Ferrite and Martnesite formation in stainless steels, Welding journal 52(5) (1973) 193.

[113] Y. Jang, S. Kim, J. Lee, Effect of different Mn contents on tensile and corrosion behavior of CD4MCU cast duplex stainless steels, Materials Science and Engineering: A 396(1) (2005) 302-310.

[114] T. Karahan, H.E. Emre, M. Tümer, R. Kaçar, Strengthening of AISI 2205 duplex stainless steel by strain ageing, Materials & Design 55 (2014) 250-256.

[115] H. Hemmer, S. Klokkehaug, Ø. Grong, A process model for the heat-affected zone microstructure evolution in duplex stainless steel weldments: Part II. Application to electron beam welding, Metallurgical and Materials Transactions A 31(3) (2000) 1035-1048.

[116] L.-Q. Chen, A. Khachaturyan, Computer simulation of structural transformations during precipitation of an ordered intermetallic phase, Acta metallurgica et materialia 39(11) (1991) 2533-2551.

[117] S.G. Kim, W.T. Kim, T. Suzuki, Interfacial compositions of solid and liquid in a phase-field model with finite interface thickness for isothermal solidification in binary alloys, Physical Review E 58(3) (1998) 3316.

[118] H. Hibbitt, B. Karlsson, P. Sorensen, Abaqus analysis user's manual version 6.10, Dassault Systèmes Simulia Corp.: Providence, RI, USA (2011).

[119] B. Rhee, S. Roh, D. Kim, Transient Liquid Phase Bonding of Nitrogen Containing Duplex Stainless Steel UNS S31803 Using Ni-Cr-Fe-Si-B Insert Metal, Materials Transactions 44(5) (2003) 1014-1023.

[120] P. Shewmon, Diffusion in Solids, 2nd, Ed., TMS, Warrendale, PA (1989) 107.